CHARACTERIZATION OF MECHANICAL DISCONTINUITIES USING MACHINE LEARNING AND KNOWLEDGE DRIVEN CAUSAL MODEL

A Dissertation

by

RUI LIU

Submitted to the Graduate and Professional School of
Texas A&M University
in partial fulfillment of the requirements for the degree of

DOCTOR OF PHILOSOPHY

Chair of Committee,	Siddharth Misra
Committee Members,	Eduardo Gildin
	Kan Wu
	Benchun Duan
Head of Department,	Akhil Datta-Gupta

August 2023

Major Subject: Petroleum Engineering

ABSTRACT

Mechanical wave transmission through a material interacts with the propagation of mechanical discontinuity in the material. Machine learning can be used to monitor the propagation of embedded discontinuities by analyzing the resultant waveforms recorded by a multipoint sensor system placed on the surface of the material. Our study accomplishes a first-of-its-kind monitoring of mechanical discontinuity propagation by using data-driven model to process the multipoint waveform measurements resulting from a single impulse source. While conventional data-driven methods, especially supervised learning, rely primarily on statistical correlation/association and lack domain knowledge and causality. The primary objective of this work is to discover new geophysical causal signatures relevant to the multipoint waveform measures caused by mechanical discontinuity propagation inside a solid material. The use of causal signatures also led to the development of a novel knowledge-driven model that creates a versatile and resilient data system for both linear and physical crack propagation samples. The newly discovered causal signatures confirm that the statistical correlations/associations and conventional feature rankings are not statistically significant indicators of causality. The new developments presented in this work, especially the causal-based knowledge-driven model, have both theoretical and practical implications that can improve fracture monitoring, prediction, and early warning. In near future, similar knowledge-driven approaches will gain traction in mainstream applications of data analytics to overcome the drawbacks of current machine learning approaches such as lack of generalizability and explainability.

ACKNOWLEDGEMENTS

First and foremost, I would like to express my heartfelt gratitude to my Ph.D. supervisor and mentor Dr. Siddharth Misra for his support, guidance, and mentorship, which have been invaluable in shaping my academic journey. He has inspired me to become an independent researcher and helped me realize the power of critical thinking. I will forever be thankful for his patience and caring approach in guiding me through the challenges of the research process. His guidance, constructive suggestion, and willingness to listen to my ideas and concerns have been a constant source of motivation.

Besides my advisor, I am also grateful to the members of my thesis committee, including Dr. Kan Wu, Dr. Eduardo Gildin and Dr. Benchun Duan for their time on reviewing my work and providing feedback. Their support has been invaluable in helping me to refine and improve my research.

Then, I am extending my thanks to my friends and colleagues at Texas A&M University, who made my time here a truly great experience. In particular, I am grateful to Dr. Yuteng Jin, Dr. Aditya Chakravarty and Dr. Hao Li, just to name a few, for their helpful discussions, guidance, and support.

Finally, I would like to thank my family and my boyfriend for their unwavering support and understanding at any time, any place. Their love and encouragement have been the driving force behind my success, and I could not have achieved this milestone without them.

CONTRIBUTORS AND FUNDING SOURCES

Contributors

This work was supervised by a dissertation Professor Siddharth Misra of the Department of Petroleum.

The work in Chapter 1 was supported by Dr. Hao Li during the initial phase of this work. The HOSS simulation work depicted in Chapter 4 was partially assisted by Dr. Yuteng Jin of the Department of Petroleum Engineering.

All other work conducted for the dissertation was completed by the student independently.

Funding Sources

Graduate study was supported by a fellowship from Texas A&M University and a dissertation research fellowship from DOE BES Foundation.

This work was founded by the U.S. Department of Energy, Office of Science, Office of Basic Energy Sciences, Chemical Sciences, Geosciences, and Biosciences Division under the Award Number DE-SC0020675. Its contents are solely the responsibility of the authors and do not necessarily represent the official views of the U.S. Department of Energy.

NOMENCLATURE

ANN	Artificial Neural Network
AE	Acoustic Emission
ATE	Average Treatment Effect
ATT	Average Treatment Effect on Treated
CAD	Computer-aided Design
CATE	Conditional Average Treatment Effect
CCD	Charge-Coupled Device
CFD	Computational Fluid Dynamics
CFL	Courant-Friedrichs-Lewy
CID	Complexity-Invariant Distance
CT	Computed Tomography Scanning
DAG	Directed Acyclic Graph
DEM	Discrete Element Method
DML	Double Machine Learning
DRL	Doubly Robust Learning
FAF	Fracture Area Fraction
FDEM	Finite-Discrete Element Methodologies
FEA	Finite Element Analysis
FFT	Fast Fourier Transform
GB	Gradient Boosting
HOSS	Hybrid Optimization Software Suite
IPW	Inverse Propensity Weighting

ITE	Individual Treatment Effect
KNN	K-nearest Neighbor
LANL	Los Alamos National Laboratory
LLE	Locally Linear Embedding
ML	Machine Learning
MLP	Multi-layer Perceptron
NN	Neural Network
PCA	Principal Component Analysis
PML	Perfectly Matched Layer
PSM	Propensity Scoring Matching
RCM	Rubin Causal Model
RF	Random Forest
SCM	Structure Causal Model
SEM	Scanning Electron Microscope
SPS	Samples Per Second
SVD	Support Vector Decomposition
SVM	Support Vector Machine
UCT	Uniaxial Compression Test

TABLE OF CONTENTS

Page

LIST OF FIGURES

Page

LIST OF TABLES

Page

CHAPTER I

INTRODUCTION

1.1 Mechanical Discontinuity

The term “discontinuity” applies to any distinct break or interruption in the integrity of a material (ISRM, 1978). From a geophysical standpoint, discontinuity is a collective term that refers to mechanical separation or interface, such as joints, fractures, bedding planes, rock cleavage, foliation, faults and so on (Osogba et al., 2020). Discontinuities may appear in all sizes from as small as micro-cracks at centimeter scale to joints on the order of meters to faults on the scale of 10's of meters to kilometers as shown in **Figure 1-1** (Bakku, 2015). They are common geological phenomena with varying lengths, frequencies and orientations found in all types of rocks (igneous, sedimentary and metamorphic).

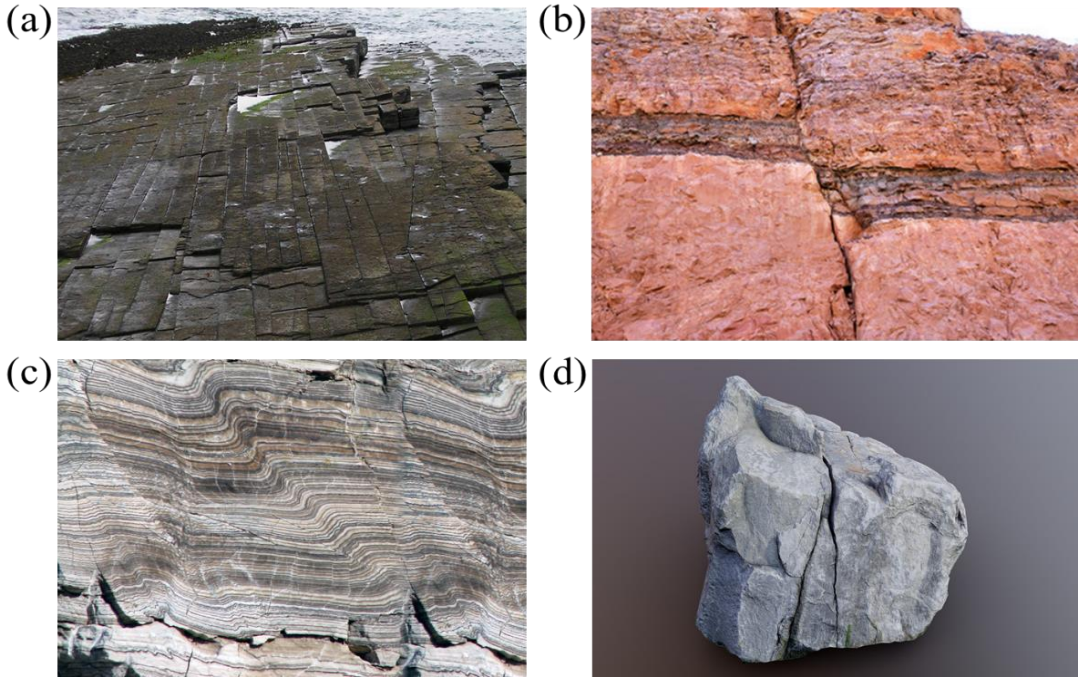

Figure 1-1. Examples of rock with different scale mechanical discontinuities. a. well-developed joint sets on flagstones at St. Mary’s Chapel, Caithness, Scotland (Reprinted from Mike Norton); b. extensional fault around Moab fault, Utah, USA (Reprinted from Herve Conge); c. fractured 7

folded gyprock in the Permian, New Mexico, USA (Reprinted from James St. John); d. cracked rock sample (Reprinted from Kless Gyzen).

Discontinuities play an essential role as a potential transport pathway and dramatically affect the material's bulk mechanical, physical, and chemical behavior (IIIman, 2014). In this study, we will refer to discontinuities as cracks/fractures. Many economically significant petroleum, geothermal, and water reservoirs form in fractured rocks. In petroleum field operations, fractures/discontinuities are often categorized as natural fractures, drilling-induced and hydraulic fractures induced by injection fluid. Proper characterization and understanding of fracture properties and their impact on various recovery mechanisms are essential at any reservoir development stage (Bogatkov & Babadagli, 2010). In this study, the following section mainly focus on various tools and techniques for detecting and characterizing natural fractures in the subsurface.

1.2 Fracture Characterization Techniques and Tools

Subsurface characterization, fracture detection, petroleum exploration and drilling operation have always been challenges to petroleum engineering. Characterization of subsurface fractures is critical for understanding the overall reservoir performance, forecasting and optimizing fossil/geothermal energy production (Al-Bazzaz, et al., 2009; Ameen et al., 2012; Liu, et al., 2015). Subsurface discontinuities can generally categorize into three types: (1) large-scale discontinuity (e.g. fault) associated with surface-based low-frequency measurements, (2) intermediate-scale discontinuity (e.g. fracture) associated with surface-to-borehole and borehole-to-borehole intermediate-frequency measurements, and (3) small-scale discontinuity (e.g. crack) associated with core-scale and microscale high-frequency measurements (Council, 1996). Many measurement techniques are available for describing mechanical discontinuities at different scales.

Outcrops allow detailed fracture surveys from vast and inaccessible areas by visual observation (Olariu et al., 2008; Casini et al., 2016). Although precise, this technique consists of

walking along faults, fractures, exposed contacts between formations, and other significant stratigraphic markers, is labor and time intensive and needs to be improved by the limited amount of data obtained (Maerten et al., 2001). A seismic survey is another critical technology to identify and study the naturally fractured reservoir from pre-stack and post-stack seismic data (Hart et al., 2002; Bakku, 2015). However, seismic-based approaches are challenged in identifying small-scale and microfractures and are strongly influenced by the frequency band (Hu et al., 2022). Conventional or image logging is also applied to characterize beddings, joints, and faults from meter to kilometer scale (Khoshbakht et al., 2009; Aghli et al., 2016; Lai et al., 2017). Resistivity/dielectric imaging is another technique used to quantitate the discontinuities, such as bedding or fractures at centimeter to meter scale for the near-wellbore regions. Conventional logging techniques provide in-situ measurements of the formation at reservoir conditions. However, they are always affected by the wellbore condition and may not be the most suitable for reservoir evaluation (Martinez et al., 2002). Image-based interpretation as a new high-resolution approach is restricted and limited by the high cost and low availability of image data observed in less than ten per cent of all wells (Tokhmechi, 2009). The core study is the most common and intuitive method for identifying small-scale fractures in boreholes. The use of cores, on the other hand, is relatively expensive, and the recovery rate in the fracture zone is low. Characterizing fractured reservoirs in the subsurface poses many challenges: different mechanical properties of geological formations, complicated field operations and minimal, expensive subsurface data, while laboratory experiments are much more accessible and could be controlled and repeated (Kosari et al., 2015).

In laboratory-scale experiments, non-destructive testing (NDT) identifies and characterizes damage or defects on the surface and within a material without cutting or altering the material

(Dwivedi et al., 2018). To date, numerous NDT techniques can be broadly categorized into five groups: 1) visual inspection (Adams, et al., 1978); 2) acoustic wave-based techniques (e.g. Acoustic Emission) and Ultrasonic testing (Scruby, 1987; Arumugam et al., 2011); 3) optical techniques (Gunasekaran et al., 1985), 4) imaging-based techniques (e.g. X-ray radiography) (Bull et al., 2013; Wu et al., 2017; Garcea et al., 2018); and 5) electromagnetic techniques (Wang et al., 2020). The elastic waves obtained through the material are expected to offer potential advantages over conventional techniques for mechanical discontinuities detection (Ibrahim, 2014). In particular, direct NDT techniques such as ultrasonic inspections and acoustic emission have a long history of development and has been applied in numerous areas, including material sciences, medical sciences and engineering fields as excellent diagnostic tools for identifying microcracks (Carpinteri et al., 2007). Even though acoustic emission testing allows for real-time damage detection and localization, this NDT technique is still qualitative. It does not provide quantitative characteristics such as the dimensions of discontinuities. (Dong & Ansari, 2011; Duchene et al., 2018; Du et al., 2020). Moreover, methods that probe deep into the subsurface using low-frequency waves cannot spatially resolve fracture locations (Council, 1996). On the other hand, ultrasonic-wave testing operates in the reflection, transmission and backscattering of elastic waves in the material systems (Ibrahim, 2014). It keeps the transducer and receiver off the surface, which is particularly beneficial when complex geometries do not allow contact (Gholizadeh, 2016).

From the upper literature analysis, most techniques are limited to expensive data acquisition and processing when mapping fractures at the needed scales and resolution. Machine learning (ML) is the application of algorithms, statistical methods, software, and computational systems to develop data-driven models that can perform specific tasks by learning from patterns and trends in real/simulated data to improve efficiency, efficacy, and productivity. ML algorithms

have been exploring, extracting, and recovering of subsurface energy resources, primarily in hydrocarbon E&P industry and potentially in geothermal energy. More ML studies have also been carried out to provide fast and accurate multiscale fracture modelling to improve the subsurface characterization of reservoirs. The following section briefly describes existing ML applications to build automation, intelligent and innovative systems to solve challenges faced by traditional fracture characterization and detection approaches.

1.3 Fracture Characterization with Machine Learning

With the development of computational power and big data technology, there has been a rapid increase in sensor deployment, data acquisition, data storage, and data processing for purposes geothermal/fossil energy development and exploration. This has promoted large-scale deployment of data-driven methods, ML and data analytics workflows to find and extract energy and material resources from the subsurface earth. Subsurface data ranges from nano-scale to kilometer-scale passive as well as active measurements in the form of physical fluid/solid samples, images, 3D scans, time-series data, waveforms, and depth-based multi-modal signals representing various physical phenomena, ranging from transport, chemical, mechanical, electrical, and thermal properties, to name a few. Integration of such varied data sources being acquired at varying scales, rates, resolutions, and volumes mandates robust ML methods to better characterize and engineer the subsurface earth.

2D and 3D scanning seismic images interpretation is usually combined with ML algorithms to provide high-resolution structural models of the subsurface (Hale, 2012; Hale, 2013; Chehrazi et al., 2013; Xiong et al., 2018; Cunha et al., 2020). In particular, the artificial neural network (ANN) method has received the most attention in subsurface geological exploration. The biggest challenge is the computational cost and errors when processing large amounts of digital seismic

data. Over recent years, conventional logging data has also been extensively integrated with ML to predict fractures in reservoir formations near the wellbore (Zazoun, 2013; Aleardi, 2015; Talebkeikhah et al., 2021). Although conventional petrophysical data can contribute to identifying fractured zones and even quantifying fracture density, those logs were only recorded at limited depth intervals along a good path due to the acquiring data budget. Additionally, different logging data exhibited distinctive responses with closed or open fractures (Talebkeikhah et al., 2021).

Reid and Harrison first presented an automated tracing of rock mass discontinuities from digital images in 1997(Reid & Harrison, 1997). After that, imaging tools such as computed tomography (CT) scanning, scanning electron microscope (SEM), charge-coupled device (CCD) camera and X-ray imaging were widely used to investigate structural features of reservoir rocks directly. In recent years, advanced regression algorithms and deep-learning tools have been used to improve the identification and characterization of microfractures (Lemy & Hadjigeorgiou, 2003; Wang et al., 2007; Tian & Daigle, 2018). Application studies include automated fracture trace map extraction (Huang et al., 2018; Chen et al., 2021), fracture parameter (e.g. density, permeability) prediction (Rajabi et al., 2021), porous structure reconstruction (Wang et al., 2018; Kamrava et al., 2019). However, imaging based-ML approach has two limitations. First, commonly occurring interfering objects such as shadows, stripes, scratches, materials filling fractures, and nearby vegetation on the rock images can be misclassified (Byun et al., 2021). Secondly, ML model performance could be more reliable for a small set of training images and is not guaranteed for new types of images.

Fractures significantly impact wave propagation through a medium, so careful analysis of waves in fractured media must be considered, especially in fracture characterization (Cho et al., 2018). Recent advances in machine learning methods have allowed us to process high-dimensional

wave datasets for enhanced detection of anomalies and processes with high granularity at multiple scales (Misra et al., 2020; Chakravarty et al., 2021).

1.4 Organization of the Dissertation

Very little was found in the literature on whether simulated wave data could help to understand the crack-bearing materials better. This study will apply supervised learning, such as classification and regression algorithms, for fracture network characterization combined with multipoint wave-transmission measurements around the materials. The laboratory experiments inspired our 2D numerical models of material containing discontinuities (Bhoumick et al., 2018), wherein multiple sonic sources and receivers are placed around porous cylindrical rock samples to quantify the distribution of embedded cracks. The following section will integrate wave simulation, ML and cutting-edge causal techniques to solve the following questions based on the claims mentioned earlier.

Chapter 1 introduces discontinuity, different scales, and existing traditional approaches for fracture characterization. The motivations of the research and a brief literature review about machine learning applications with seismic interpretation, conventional logging, image-based and wave data in subsurface characterization are addressed.

Chapter 2 focuses on characterizing discontinuity orientation, dispersion, and spatial distribution in formation by processing different-waves travel-time detected at multiple locations with different data-driven methods. The primary purpose of classification algorithms is to visualize the fracture system by learning from the current training travel time and evidence. The developed models can then be applied to any new travel time dataset to predict the crack information.

Chapter 3 aims to visualize linear discontinuity propagation in 2D materials of any composition, velocity, density, porosity, and size. By examining the elastic waveforms captured

by a multipoint wave-transmission sensor system positioned on the material's surface, the suggested data-driven approach enables the tracking of embedded discontinuities across three key stages: initial, intermediate, and final. The optimized sensor system configuration is also carried out to maintain model accuracy with a limited number of sensors and their corresponding placements.

Chapter 4 analyses the causal inference techniques to find the causal signatures of crack propagation (the cause) from a feature space, including time-domain and frequency-domain features captured from waveforms recorded by the nine sensors (the effect). By leveraging the causal signatures, the new proposed knowledge-driven model, which is guided by domain knowledge and causal inference, can provide robust and efficient insights for understanding crack propagation, as discussed in Chapter 5. Generating causal hypotheses in the statement is heavily reliant on domain knowledge. Finally, Chapter 6 summarizes the study's conclusions and outlines future research directions in this field.

CHAPTER II

CHARACTERIZING OPEN OR CLOSED MECHANICAL DISCONTINUITIES NETWORK BASED ON MULTIPOINT, MULTIMODAL TRAVEL-TIME MEASUREMENTS WITH DATA-DRIVEN CLASSIFICATION*

2.1 Fracture Definition and Classification

Fracture is any planar or sub-planar discontinuity that is narrow in one dimension compared to the other two and forms due to external (e.g. tectonic) or internal (thermal or residual) stress. Depending on the relative displacement of discontinuity surface, all tectonic fractures fall into two mechanical types; shear fractures and extension fractures. Different kinds of fractures exhibit different geometry, mechanical effects, and flow properties (Council, 1996). Shear fracture refers to the shear slip surface with relative parallel movements (e.g. faults). Extension fracture shows perpendicular displacement or in other words moving outward from the fracture plane (e.g. joints, fissures). Extension fracture, also known as open fracture, is commonly filled with gas, fluids, magma, and minerals. Mineral-filled extension fractures are named veins, while magma-filled fractures are assigned to dikes. The mineral fillings always have different permeabilities than the host rock, and vein bridges may keep fractures open. The mineral fillings can provide information about the properties of the fluids flowing in the fractures, the original porosity, and the physical and chemical conditions during precipitation (Council, 1996).

Rock fracture mechanics is a promising outgrowth of rock mechanics and fracture mechanics which has been widely applied to hydraulic fracturing, mechanical fragmentation, rock slope analysis, geophysics, earthquake mechanics, hot dry rock geothermal energy extraction and

* Part of this chapter is reprinted with permission from “Characterization of mechanical discontinuities based on data-driven classification of compressional-wave travel times.” By Hao Li, Copyright 2021 International Journal of Rock Mechanics and Mining Sciences, 143, 104793.

many other practical problems (Chang et al., 2002). In the field of fracture mechanics, it is common to classify the crack planar into three different loading types termed mode I, II, and III as illustrated in **Figure 2-1**. The displacement mode on fractures is an essential parameter for rock fracture characterization. Mode I represents the tensile opening mode where tensile stress is normal to the plane of the crack. Mode II is sliding mode stands for the shear stress acting parallel to the plane of the crack. Mode III also involves shear stress but tearing mode acting parallel to the crack plane.

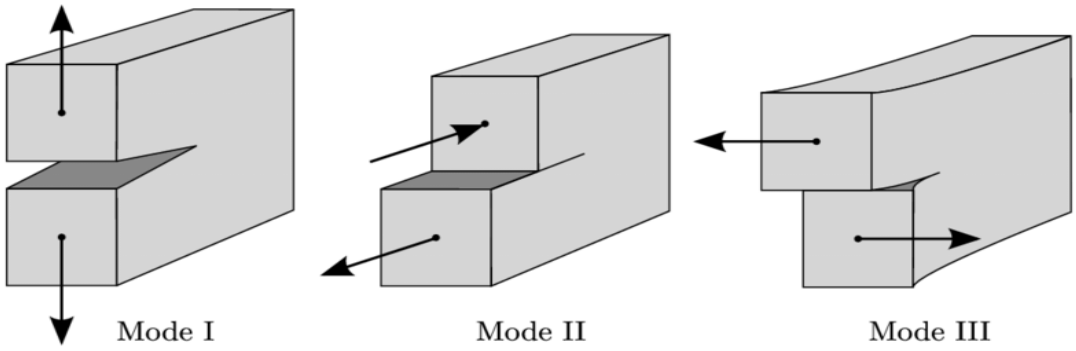

Figure 2-1. Fracture modes classified in study of fracture mechanics. Opening or tensile mode (Mode I), sliding mode (Mode II), and tearing mode (Mode III) (Reprinted from David S. Kammer, (Kammer, 2014))

Fractures combining these modes (mixed-mode fractures) are also possible (Ayatollahi & Aliha, 2007; Richard et al., 2014). While this alternate classification can be beneficial in analyzing fractures in engineering fields, it is restrictive in our applications because of the complex geological structures. Identifying the propagation directions and the mechanical condition at their fronts is often tricky.

2.1.1 Discrete Fracture Network

The broadly defined fractures seldom occur alone, instead, they occur as part of fracture zones or complex fracture networks. The discrete fracture network (DFN) provides a computational paradigm model for describing fracture population (and other discrete features such

as faults, breccia layers, and dikes) embedded inside a rock mass viewed as a set of discrete finite cracks (Dershowitz & Doe, 1988; Dershowitz et al., 2003). The technique was created and discussed by different studies from around 1980s for both 2D and 3D problems (Long et al., 1982; Robinson, 1984; Smith & Schwartz, 1984; Andersson & Dverstorp, 1987), and was continuously developed afterwards with many applications in reservoir engineering and other geoscience and geoengineering fields. By default, the discrete fractures are line segments in the 2D model or planar disks in the 3D model. The properties of individual or discrete fractures are explicitly described in a DFN model, which is distinguished from the matrix. The permeability of fractured zone is usually more extensive than matrix; as a result, the fluid will flow mainly through the fracture network when the fractures are connected (Li & Lee, 2008; Cottrell & Dershowitz, 2012). The construction of a spatial model that describes how fractures are distributed and the inter-relationship between fractures, stratigraphy, lithology, and structure is the key to DFN modelling (Li & Lee, 2008).

2.2 Workflow

2.2.1 Key Fundamental Questions to be Answered

This chapter aims to answer the following questions:

- How to characterize spatial properties of the crack clusters by jointly analyzing multipoint measurements of p-wave, s-wave, and pressure-diffusion travel times?
- Can fracture characterization in crack-bearing materials be adequately achieved using wave arrival time from the fast-marching method?
- How do different fracture types, such as open or closed fractures, impact the understanding of fracture clusters inside the material?

- Based on the experimental configurations, which sensor location is the most important for fracture characterization? How many sensors are required to ensure the workflow performance?

2.2.2 Description of Workflow

Wave propagation and diffusive transport phenomena could work as evidence of the mechanical discontinuities in the material. This work proposes a 2D crack-bearing material characterization approach by processing wave travel-time using different data-driven classification techniques for the low efficiency of the existing fracture simulation methods. We utilize classification models to predict discontinuities orientation, dispersion, and spatial distribution prediction by learning from the different-waves simulation models. **Figure 2-2** shows the basic workflow for this study. A good starting point is accurately identifying the current fracture system created by a discrete fracture network (DFN) with open or closed discontinuities.

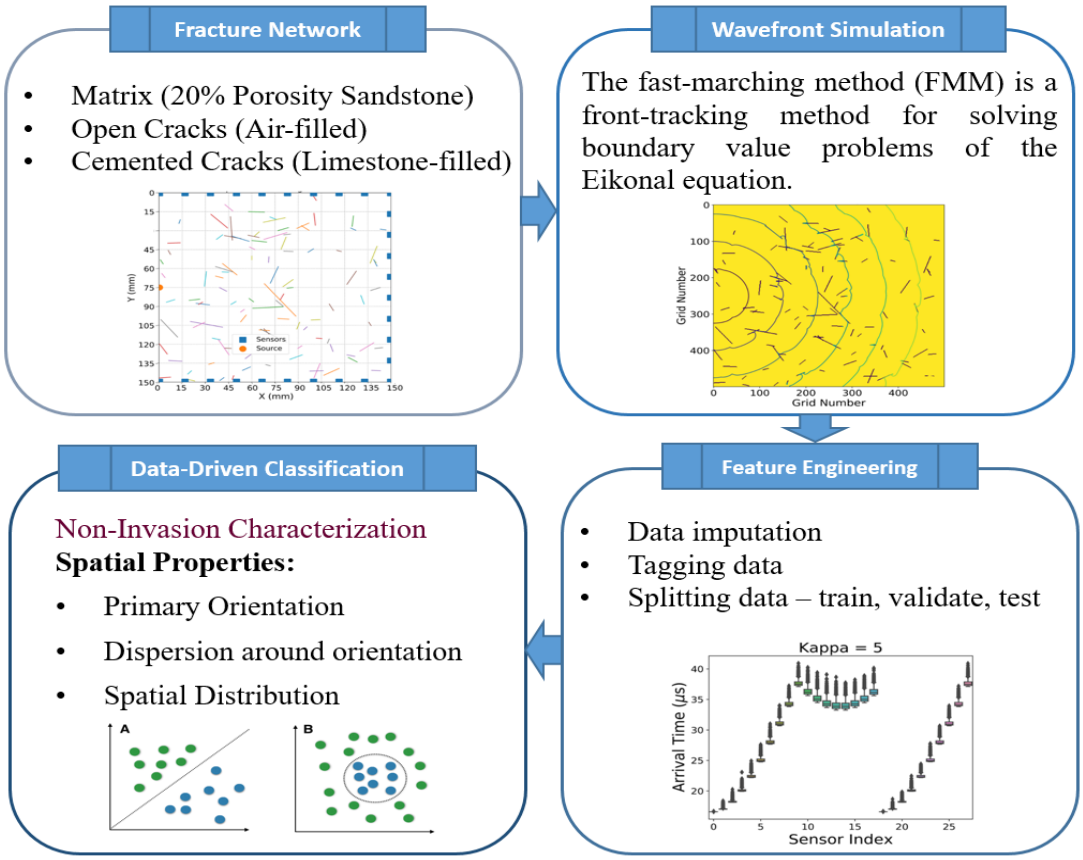

Figure 2-2. Workflow for crack-bearing materials characterization by learning patterns from simulated the propagation of the wave/diffusion front.

The DFN model is established on understanding and representing the two factors: fracture system geometry and properties of individual fractures. Each crack-bearing model is embedded with 100 fractures of randomized length, orientation, and dispersion in this work. The crack cluster embedded in the crack-bearing material is generated using the DFN method. Crack length is selected randomly from an exponential distribution of 0.3mm - 3mm. Crack orientation is sampled randomly from the von Mises distribution, and crack locations are modelled using the intensity function. Then, use the fast-marching method (FMM) to simulate the propagation of the wave/diffusion front from a single source through the 2D crack-bearing material to multiple receivers placed around the crack-bearing material. The wave source and 28 sensors are around a

2D squared crack-bearing material. Next, simulated travel time can be divided into training and testing datasets. A training set is implemented in a dataset to build a model, while a test (or validation) set is to validate the built model. Notably, data points in the training set are excluded from the validation set. Our tests use 70% of the data as training data. Cross-validation approaches split the original training data into one or more training subsets to balance the response variances. The remaining 30% of data is working as testing data to evaluate the classification models.

In the end, the data-driven classifiers are applied to explore the possibility of using wavefront travel time for characterizing specific statistical attributes of the crack-bearing systems. The existence of cracks influences the propagation of the waves/pressure diffusion, resulting in different arrival times. Supervised learning, like classification models, will learn the wave propagation patterns across the training samples to facilitate the characterization of crack-bearing materials.

2.3 Simulation Model Description

2.3.1 Fast Marching Method (FMM) for First Arrival Simulation

FMM is a front-tracking method created by James Sethian for solving boundary value problems of the Eikonal equation (Sethian, 1996). Eikonal equation characterizes the evolution of a closed surface as a function of time with specified velocity on the given surface, expressed as:

$$\mathbf{f}(\mathbf{x})|\boldsymbol{\nabla}\mathbf{u}(\mathbf{x})| = \mathbf{1} \text{ for } \mathbf{x} \in \boldsymbol{\Omega} \quad (1)$$

$$\mathbf{u}(\mathbf{x}) = \mathbf{0} \text{ for } \mathbf{x} \in \boldsymbol{\partial\Omega} \quad (2)$$

where $u(x)$ represents the travel time of the front wave to reach the location x, $f(x)$ stands for the speed at x known as velocity function, Ω is the open set with well-behaved boundary, $\partial\Omega$ is the boundary, and x is the coordinate system. As described, this equation is a non-linear partial differential equation to solve the wave propagation problems. In this paper, we use FMM to

approximate the solution to the Eikonal equation. Scikit-fmm is a python extension module that implements the fast-marching method used in our program. This package only works for regular Cartesian grids, but grid cells may have a different (uniform) length in each dimension.

For pressure diffusion propagate front, the Eikonal equation is described based on diffusivity.

$$\sqrt{\boldsymbol{\alpha}(\mathbf{x})}|\boldsymbol{\nabla\tau}(\mathbf{x})| = \mathbf{1} \tag{3}$$

where, the diffusivity $\boldsymbol{\alpha}(\mathbf{x})$ defined as:

$$\boldsymbol{\alpha}(\mathbf{x}) = \frac{\mathbf{k}(\mathbf{x})}{\boldsymbol{\phi}(\mathbf{x})\boldsymbol{\mu}\mathbf{C_t}} \tag{4}$$

Eq. 3 tells that the pressure "front" propagates in the reservoir with a velocity given by the square root of diffusivity. For homogeneous reservoirs, $\boldsymbol{\tau}(\mathbf{x})$ is related to physical time through a simple expression of the form $t(x) = \frac{\tau(x)^2}{c}$ where the constant c depends on the specific flow geometry. For linear, radial, and spherical flows, c is ¼ 2, 4, and 6, respectively (Kim et al., 2009).

2.3.2 Transmitter-receiver configuration

The 2D numerical models of crack-bearing material implemented in this study are inspired by the laboratory experiments conducted at the Integrated Core Characterization Center (Bhoumick et al., 2018). In those studies, they placed multiple sonic wave sources and receivers around a cylindrical rock sample to comprehensively describe the inside fracture and its morphology (Bhoumick et al., 2018). The 2D simulation models and the position of the sonic sensors in this study are similar to the real-world experiment with 1 sonic source and 28 receivers. The wave source is in the middle of the left boundary. The 28 receivers are equally spaced on the remaining three boundaries. Each boundary has ten sensors. The travel time of the front wave from FMM simulation at 28 sensors will be recorded as the initial dataset for fracture characterization.

Designed squared material has a dimension of 150mm × 150 mm discretized by 500 × 500 grids. The majority of petroleum reserves in the world are found in ancient sandstones, which have porosity and permeability (Weimer & Tillman, 1982). Therefore, we assume the matrix is sandstone with 20% porosity. The velocity set of wave/diffusion is set based on the behavior of the porous sandstone physical ground. The present chapter aims to learn more about the fracture system using P-wave, S-wave, and pressure diffusion propagating through sandstone samples. Without considering the water saturation and pressure effect in the field, we assume the compressional wave velocity is 3760 m/s. The shear wave velocity values in a porous material will always be less than the compressional wave, assumed as 2300 m/s in our case (Hamada & Joseph, 2020). In our cases, the shear wave is assumed to be 2300m/s. Then, our approach draws on the solution to the diffusive-pressure equation that mimics pressure front propagation phenomena.

Fracture systems embedded in the materials models is generated by DFN with different statistical parameters to create different groups of models. Each DFN model is embedded with 100 fractures of randomized length, orientation, and dispersion, representing different fracture systems. This work has considered two different cracks; one type is designed as an open fracture with air. Another type is cemented fracture filled with 0% porosity limestone. Each crack length is randomly picked from an exponential distribution of 0.3mm-3mm. Crack orientation is sampled randomly with the Von Mises distribution. The Von Mises distribution, called the circular normal distribution, is a continuous probability distribution ranging from 0 to 2π (Mardia & Zemroch, 1975). It is similar to the normal distribution, except coordinates are placed on a circular plane. The detailed information is explained in the following section 2.4.

2.3.3 Variable transport properties of mechanical discontinuity

In physics, the transport phenomenon involves the movement of various entities, such as mass, momentum, or energy, through a medium, fluid, or concrete, under nonuniform conditions existing within the medium. The wave energy and pressure difference between the matrix and the mechanical discontinuities drives the transportation through pores media in our study. The travel time of the wavefront is expected to capture the character of the mechanical discontinuities. However, real-world rock discontinuities are more complicated to simulate. In this study, we use a simple numerical model that assumes the open cracks are filled with air; closed ones are cemented by 0% porosity limestone to generate the required travel-time dataset.

In total, we generate multi-modal include compressional wave, shear wave and pressure diffusion to simulate the wave front arrival time. Longitudinal or compression waves are defined as waves where the particle motion is in the same direction in which the wave is propagating (Watson, 2015). For embedded open discontinuities, the compressional wave is traveling through the air. The travel time calculation uses 340 m/s as the fracture velocity, which has a large contrast compared to the matrix velocity of 3760 m/s. For cemented fractures, compression wave traveling faster in limestone than sandstone is 6860m/s.

The shear and compressional waves respond differently to reservoir fluids and pressure (Zhang, 2019). The shear wave travels slower than P-wave because they do not change the volume of the material during propagation. An important distinguishing characteristic of an S-wave is its inability to propagate through fluid or gas because they cannot transmit the shear stress. In our experiments, the open discontinuities are filled with air that is not able to propagate S-wave. We set the S-wave velocity as a small value, 1m/s. However, S-wave travels around 4200m/s through

limestone for embedded closed discontinuities, which is about 1.6 times slower than compressional wave (Greenberg & Castana, 1992).

Diffusion waves have high frequency-dependent attenuation and slow velocity of propagation (Silin et al., 2003). In fluid-saturated rocks, the pressure diffusion mechanism can explain the high attenuation of low-frequency signals (Silin et al., 2003). Diffusivity is an important parameter indicative of diffusion mobility. It described diffusion velocity related to porous media permeability, porosity, compressibility, and fluid viscosity as described in Eq.4. The main difference between fracture and matrix in that equation is permeability. For closed discontinuities, the crack permeability is lower than the matrix. On the contrary, open crack is more porous than the sandstone matrix.

2.4 Description of DFN Model Experiments

This study will include three different tasks with various 2D DFN model setup: (1) identify the crack dispersion with dominated orientation; (2) identify the dominant crack orientation with different fracture dispersion; (3) identify the crack spatial distribution. The numerical models for each task using various mechanical discontinuities systems. The orientation of 100 embedding fractures in the model are drawn from von Mises distribution with specified mode (μ) and dispersion (κ), on the interval [-π, π]. The von Mises distribution was proposed and named for Richard von Mises in 1918 (von Mises, 1918; von Mises, 1964). Its probability density function is defined as:

$$p(\theta) = \frac{1}{2\pi I_0(\kappa)} \exp(\kappa \cos(\theta - \mu)) \quad (5)$$

where θ is the orientation samples, μ is the distribution location parameter and κ is shape parameter, and $I_0(\kappa)$ is the modified Bessel function of order 0.

$$I_n(\kappa) = \frac{1}{\pi}\int_0^{\pi} \exp(\kappa\cos\theta)\cos(n\theta)\,d\theta \quad (6)$$

In other words, the mode μ is the mean orientation of the distribution. In general, it can be any real number. κ can be better understand as the "concentration" which is reciprocal to crack dispersion. $\frac{1}{\kappa}$ is comparable to the variance in normal distribution. High concentrations imply low variance and vice-versa. Values for κ must be non-negative real numbers. If $\kappa = 0$, the distribution is uniform; if values for κ are large, the distribution becomes a normal distribution.

2.4.1. Identification of Crack Dispersion

The first task is the identification of crack dispersion. We built three crack-bearing models with distinct κ value around the dominant crack orientation set as vertical in our case. The simulation models are presented in **Figure 2-3**. The wave source is in the middle of the left boundary (Orange Spot in **Figure 2-3**), and the remaining three boundaries have 28 receives (Blue Square in **Figure 2-3**) equally located. When the dispersion factor is set to 0, the crack orientations are equally distributed in all directions. As a comparison, when dispersion factor is set to 1000, orientations are nearly aligned with the direction of the dominant orientation. For each case, 5000 samples are generated for multiple front wave travel time simulation. The entire dataset comprises 15,000 samples, such that each sample has 28 features and 1 target for only compressional wave.

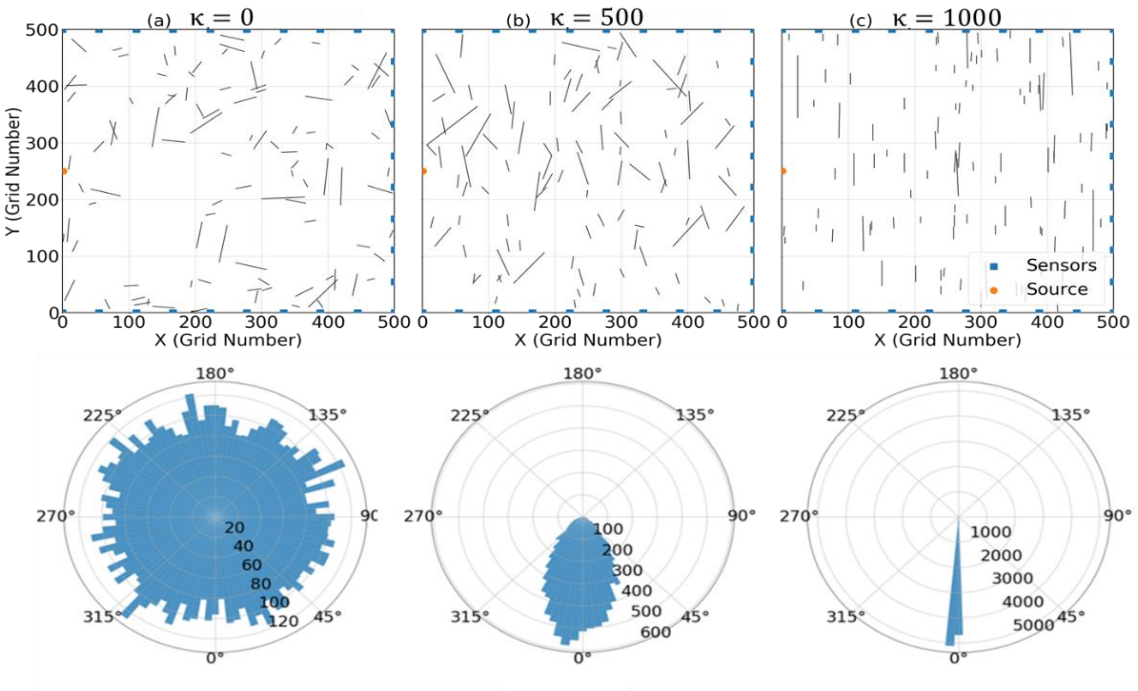

Figure 2-3. Experiment configuration for the identification of crack dispersion factor, κ. (a) First column is κ = 0, fracture orientation is totally random (b) κ = 500, orientation changing range is 50 degree (c) κ = 1000, cracks are almost parallel to the dominant orientation which is vertical.

Our input dataset is a large table with 28*3 columns representing different wave arrival time from different sensor records and the rows standing for the sample numbers. This table can be further simplified by feature engineering to avoid overfitting. The outputs are labeled as 0, 1, 2, which stand for κ value equal to 0, 500, and 1000. In supervised learning, the target labels are known for the training dataset but not for the test. Label not only has a meaning of describing the input but also the expecting output from the classifiers.

2.4.2. Identification of Dominant Crack Orientation

Task 2 and 3 design data-driven workflow to identify four dominant crack orientations of 0°, 45°, 90° and 135°. This task contains 4 different types of crack clusters that differ in orientation with fixed dispersion around the dominant orientation. To compare the effects of dispersion on this task, we set one experiment at dispersion equal to 10, and another experiment at

dispersion equal to 50. **Figure 2-4** shows the experimental configurations for different dominant crack orientations with dispersion factor. For each dominant orientation and dispersion factor combination, 5000 samples' travel time is recorded as the model dataset. It took around 2 hours on a Dell workstation with a 3.5GHz Intel Xeon CPU and 32GB RAM. The front wave travel times at different sensors are features of a data-driven model. Four orientations are labeled as 0, 1, 2, 3 as our targets. In other words, a target value of 0, 1, 2, and 3 represents crack orientation of 0°, 45°, 90° and 135°.

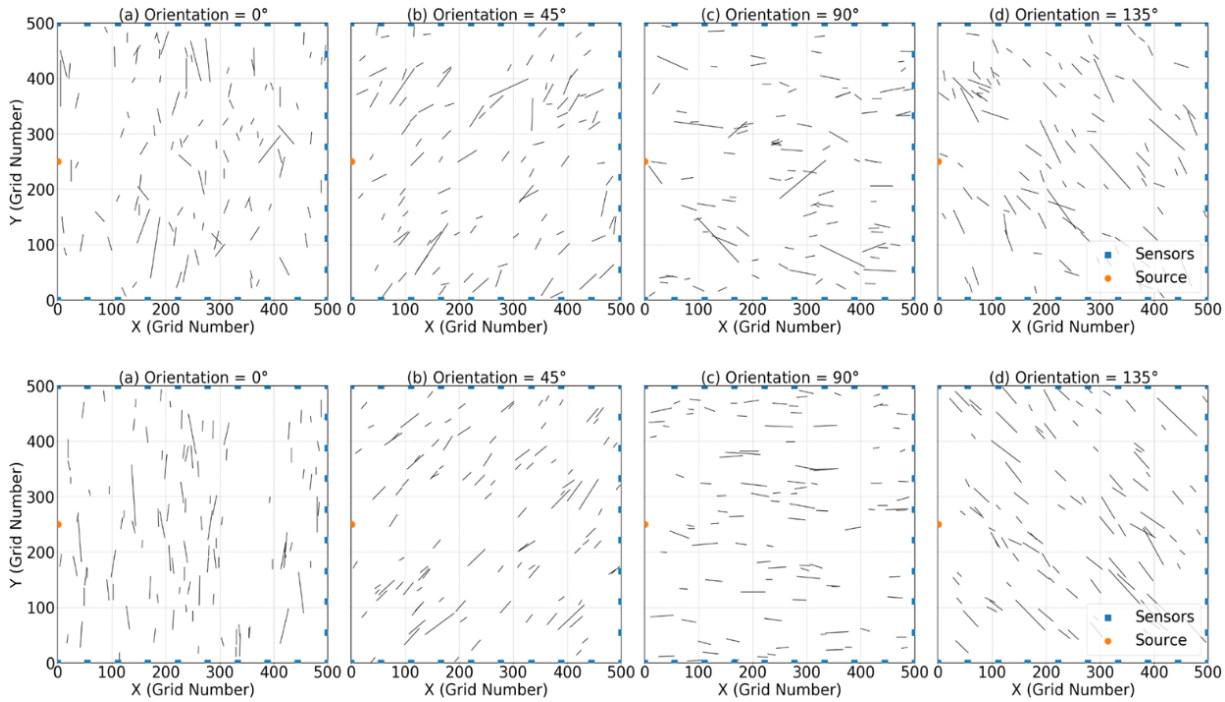

Figure 2-4. Experiment configuration for orientation identification with specific dispersion. The first row is $\kappa = 10$; The second row is $\kappa = 50$. Four columns represent different orientations, θ: (a) $\theta = 0^o$, (b) $\theta = 45^o$, (c) $\theta = 90^o$, (d) $\theta = 135^o$

2.4.3. Identification of Crack Cluster Spatial Distribution

The final task is to identify four spatial distribution types shows in **Figure 2-5**. The spatial distribution classification of mechanical discontinuities in the formation is creating using intensity functions.

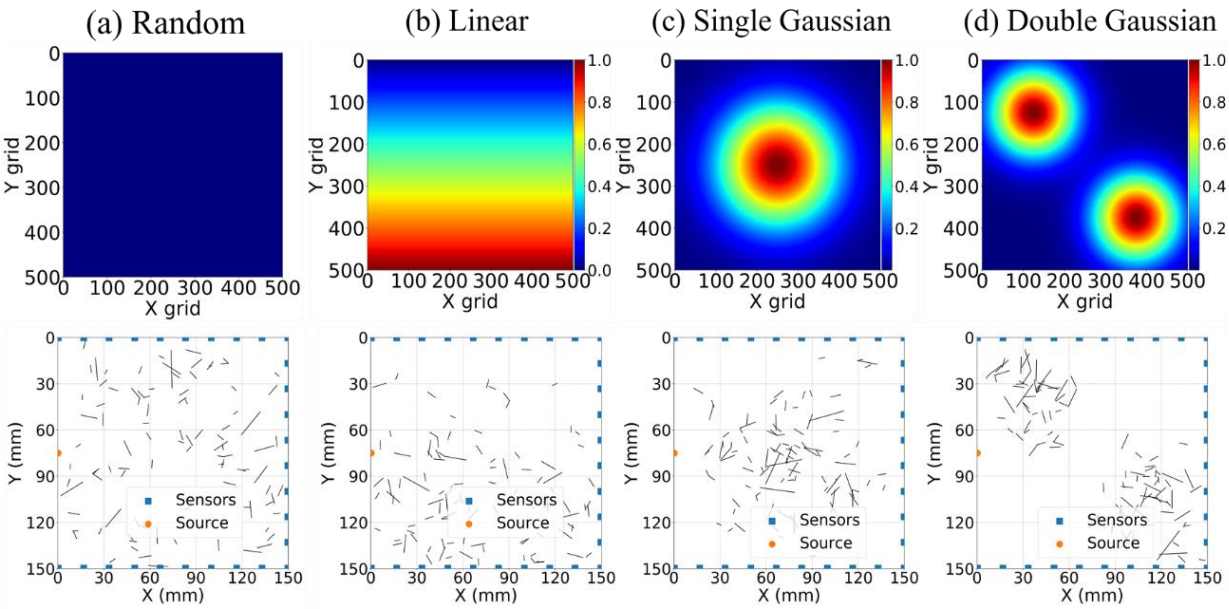

Figure 2-5. Experiment configuration for four distinct spatial distribution classification include random intensity function, linear probability function, single gaussian function and double gaussian function.

These functions describe the crack occurrence probability in the investigated material. In the spatial distribution classification, type 1 is a random distribution created using a constant intensity function, which means that cracks have an equal probability of occurring in the material. Type 2 is the linear distribution followed by the linear probability function that related to y axis:

$$\boldsymbol{\lambda(x, y) = y} \tag{7}$$

In **Figure 2-5**, the upper plot in column (b) shows the possibility of crack acceptance increasing linearly from upper to lower boundary (color goes from blue to red in plot). Therefore, the cracks are more concentrated at the bottom part of the material.

Then, gaussian function is applied on the crack-bearing material as intensity function:

$$\boldsymbol{\lambda(x, y) = c * \exp^{\left(-d*(x-x_o)^2+(y-y_o)^2\right)}} \tag{8}$$

where $\mathbf{x_o}$ and $\mathbf{y_o}$ is the center of the Gaussian distribution both set to 250, d controls the variance of the distribution is set to 0.00005, and c controls the minimum value of the intensity function

equal to 1 in our case. The acceptance probability is high at the center of the crack-bearing material. When adding two Gaussian crack clusters in the material referred as the bimodal distribution. Similarly, the dataset contains 20,000 samples, with 4 targets stand for spatial distribution.

2.4.4 Data description – P-wave, S-wave, Pressure Diffusion

Data collection and preparation are the foundation step for the development of machine learning models. Data visualization is the graphical representation using charts, graphs, maps or even tables to see and understand trends, outliers, and patterns in data. Visualization plots can better support further formal statistical/machine learning tests by allowing researchers to interact with the data points directly without aggregating them.

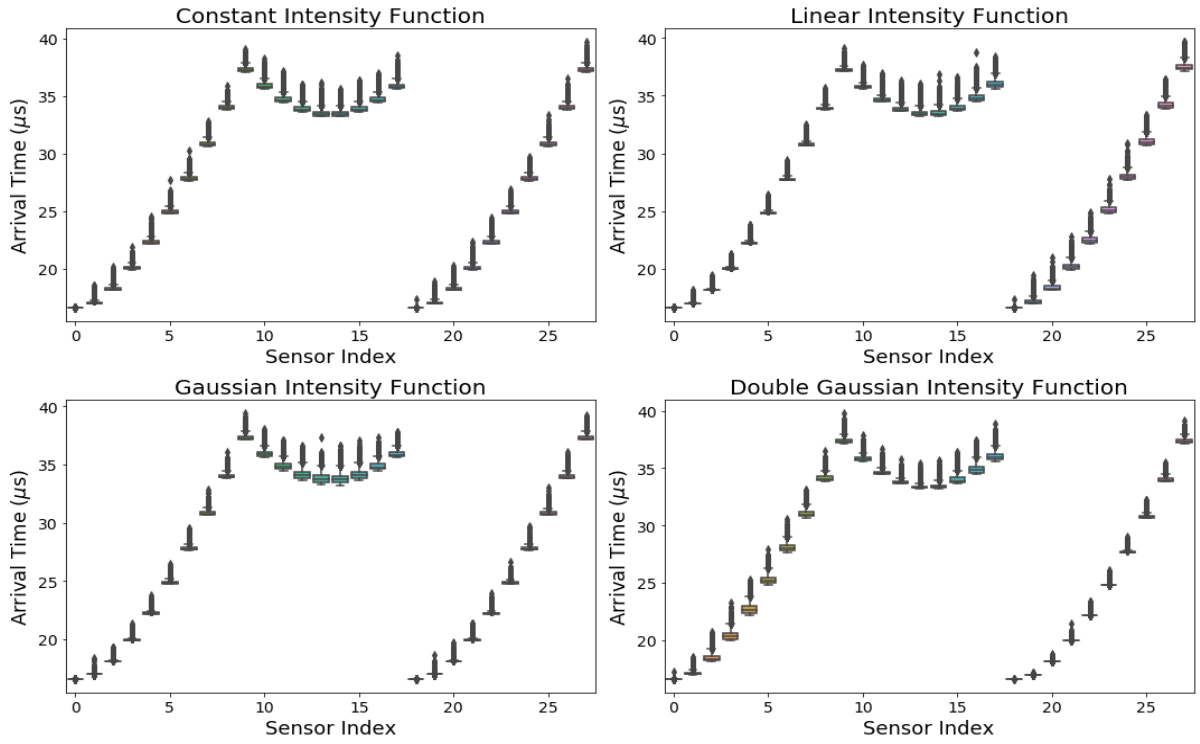

Figure 2-6. Compressional wave arrival time for four types of spatial distribution. x-axis is the sensor number, while y-axis is the wave arrival time in μs.

In this study, our input data is the multimodal wave front arrival time recorded by sensors around the squared materials. **Figure 2-6** is compressional wave arrival time for task 4 with four different intensity

functions from section 2.4.4. All the simulated arrival time in the plots is generated assuming closed fracture with 0% porosity limestone. Each box plot display 5000 samples' sensor arrival time at different locations. It includes five important lines: minimum, first quartile (Q1), median, third quartile (Q3), and maximum. The outliers are shown as individual points. Sensor 1 to 10 is located on the upper boundary, while sensor 19 to 28 are placed on the bottom boundary. The remaining sensors are opposite to the source boundary which exhibit distinct distribution due to the longer reaching distances. The upper and lower corresponding receivers have the same distance to the source. Therefore, their recording arrival time are very similar. **Figure 2-7** reveal the shear front wave reaching time as supplementary information for the mechanical body wave. As comparison, they cannot move through any type of material and travel much slower than the speed of P-wave. Hence, it takes longer for the S-wave to reach the receiver.

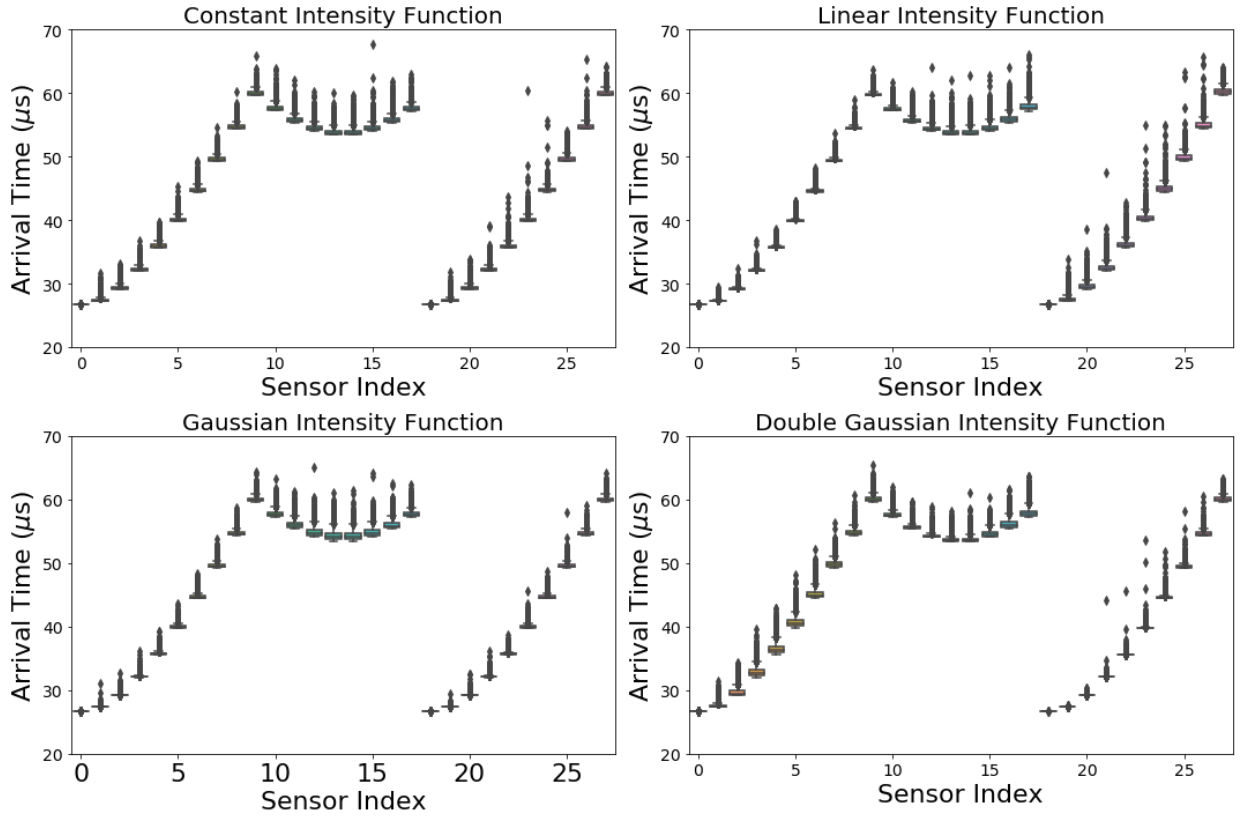

Figure 2-7. Shear wave arrival time for four types of spatial distribution. x-axis is the sensor number, while y-axis is the wave arrival time in μs.

Diffusion waves have been known about since the mid-19th century (Mandelis, 2000). Technologies based on diffusion waves have already improved biomedical diagnostics and the fabrication of optical and electronic devices (Volpert & Petovskii, 2009). Diffusion waves have also spawned novel high-precision analytical techniques. The previous plots showed the crack effect of mechanical waves arrival time. Furthermore, we add pressure diffusion front as another set of features in **Figure 2-8**. In total, 28 sensors recorded 3 set of front time including the P-wave, S-wave and pressure diffusion. The feature number expended to 84.

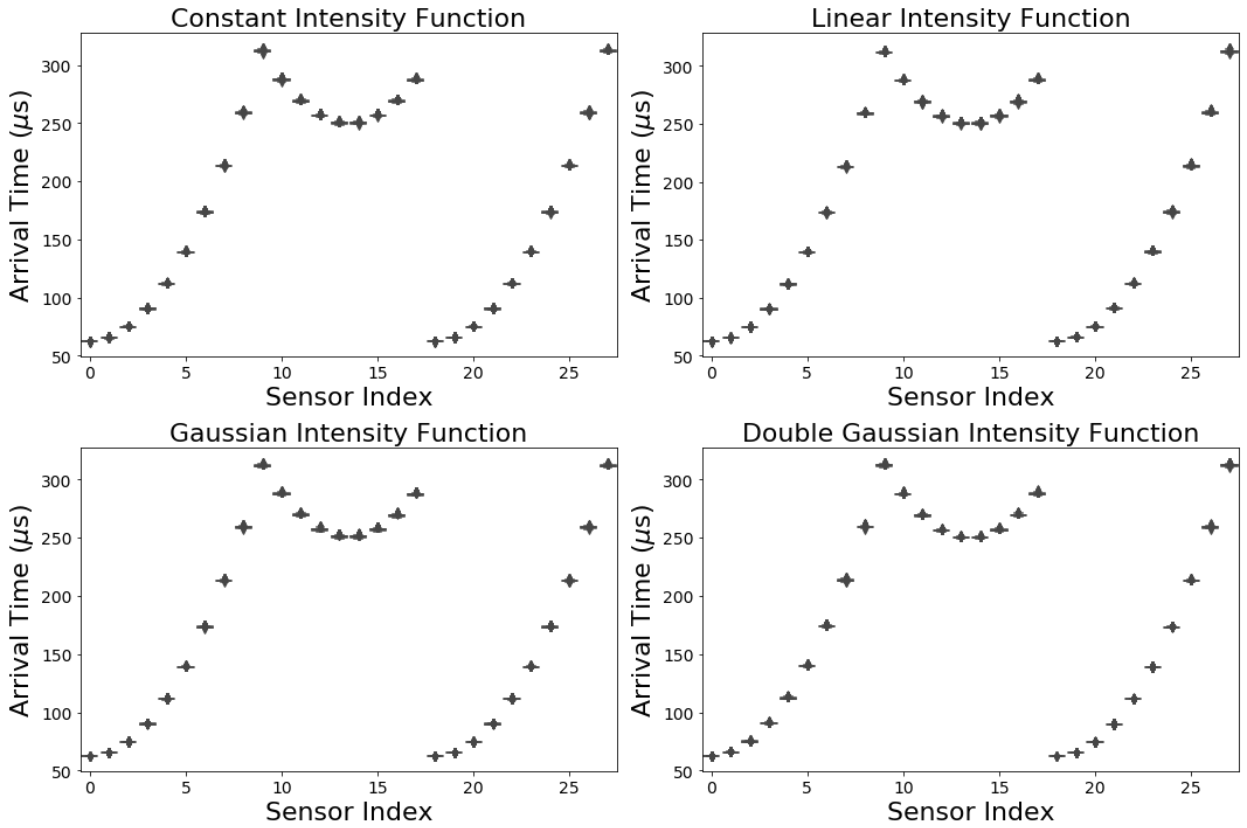

Figure 2-8. Pressure diffusion front arrival time for four types of spatial distribution. x-axis is the sensor number, while y-axis is the wave arrival time in μs.

Good data collection is the key to the reliable classification performance of crack characterization. The front wave travel-time measured by multiple sensors placed around the material serves as our input data for machine learning. For each task, dataset will be divided into

training and testing data to be applied in data-driven models. Before training the model, we should transfer our data to be fed into a machine learning model. The preprocessing in this work deals with features on the same scale by using the standardization approach.

2.5 Data-Driven Classification Models

Supervised learning computes a function that maps available inputs (features) to available outputs/targets (Osisanwo et al., 2017). Subsequently, the computed function can be use used to generate output for any new input. To that end, supervised learning has to find/extract hidden statistical patterns in the data during the training phase and then test the efficacy of the learning and functional mapping during the testing phase. Ongoing research in supervised machine learning focus on improving the prediction accuracy, minimizing the prediction errors, and enhancing the computational efficiency (Schmidt et al., 2019). Regression and classification are two categories of supervised learning. Regression is a task to predict a continuous output based on available inputs. However, classification predicts a class or category based on available inputs. The main goal of a classification problem is to identify the category/class in which new data will fall. Instead of traditional two-class, tasks in this study are multi-class problems including at least three classes. Seven classifiers are selected for crack characterization, namely K-nearest neighbor (KNN), Random Forest (RF), Gradient Boosting, Naïve Bayes, Support Vector Machine (SVM), Multi-layer Perceptron (MLP), and Voting classifiers.

2.5.1 Data-Driven Classification Algorithms

The KNN algorithm is non-parametric method introduced by Fix and Hodges for pattern classification that has since become known the k-nearest neighbor rule (Fix & Hodges, 1951). It can be applied for both classification and regression problems. KNN classification should be one of the first choices for a classification study when reliable parametric estimates of probability

densities are unknown or difficult to determine (Peterson, 2009). KNN is based on feature similarity that does not require any assumptions on the underlying data distribution. It first finds k number of training samples that are nearest to a new, unlabeled sample, which is then assigned a label based on the label of the majority of neighbors. By changing the value of k, the complexity of the KNN model can be changed. Small k values lead to complex models that are sensitive to noise (Liu & Zhang, 2012). The larger k will lead to smoother classification boundaries. KNN becomes computationally expensive when the size or dimensionality of the data increases because of the need to calculate distances. Therefore, the performance of KNN depends highly on the input dataset.

Decision tree is a practical, fast, and robust supervised learning method. It uses a greedy algorithm to iteratively partition feature space by randomly selecting a feature and a corresponding threshold value so as to achieve largest reduction in the impurity/entropy of the dataset leading to information gain (Su & Zhang, 2006). Each partition is a decision based on a condition. The goal of the decision tree is to separate the samples depending on their groups. Therefore, a decision tree is a collection of decisions used to identify the group/class that a sample belongs to. It is primarily designed for classification but can also be used for regression by changing the loss function from impurity/entropy to residual error. However, decision tree tends to be non-unique with high variance (Trabelsi et al., 2019). RF is an improvement machine learning algorithm introduced by Leo Breiman which combines the output of multiple decision trees to reach a single result (Breiman, 2001). It is an ensemble/collection of decision trees, suitable for both classification and regression. It is a bagging technique where several decision trees are trained and deployed in parallel. Each tree is trained on a subset of dataset using a subset of features (also referred as bootstrapping). Consequently, each tree is distinct having various levels of complexity. Finally,

the results from each tree in the random forest is aggregated based on a majority voting scheme for classification problem. The use of hundreds of decision tree in the random forest reduces the variance/uncertainty in prediction without incurring large errors due to bias. Examples of subsurface applications that use random forest as a learning algorithm include subsurface data analysis (Zahedi et al., 2018), fault detection (Marins et al., 2021), and production forecasting (Xue et al., 2021).

Boosting algorithms use several weak learners in series to build a strong learner. A weaker learner refers to model that perform slightly better than random guess (e.g. a shallow decision tree, also referred as a stump). Boosting algorithms are excellent supervised learning with a solid theoretical basis and great success applications in a wide range of practical applications including subsurface data analysis (Zhou et al., 2019; Zhong et al., 2020). They are highly customizable that take advantage of regularization methods, and generally improve the performance of the algorithm by reducing overfitting. Adaboost is the first boosting method designed for classification problem (Freund & Schapire, 1996). Each subsequent learner improves upon the performance of the previous learner by assigning higher weights to samples that were misclassified by the previous learner (Schwenk & Bengio, 1998). The final prediction of the model is the weighted average of all the weak learners, with more weight given to the weak learners exhibiting better performance as compared to the rest. Gradient Boosting (GB) is similar to AdaBoost; however, each subsequent learner in the ensemble improves on the performance of the previous learner based on gradient descent optimization to minimize the overall error of the strong learner. Weak learners train on the pseudo-residual errors of all the previous learners to focus on samples where the ensemble is performing poorly (Natekin & Knoll, 2013).

Naïve Bayes is designed based on Bayes' theorem with strong independence assumptions between the features. Particularly, studies show that naive Bayes works best in two cases: completely independent features as expected and functionally dependent features, while reaching its worst performance between these extreme (Rish, 2001). Despite its unrealistic independence assumption, it is surprisingly effective in practice since its classification decision may often be correct even if its probability estimates are inaccurate (Murphy, 2006; Berrar, 2018).

Support Vector Machine (SVM) is designed to find a hyperplane that leads to the widest possible margin separating two distinct groups (Drucker et al., 1997). It is primarily used for classification and can also be used for regression. SVM is popular because of its excellent generalization performance. SVM finds the best separation between specific samples (known as support vectors) from different groups that are closest to each other; thereby, finding the widest separation between the two distinct groups in the dataset. In addition to performing linear classification, SVMs can efficiently perform a non-linear classification using the kernel trick, implicitly mapping their inputs into high-dimensional feature spaces. SVM method has been successfully applied to several different applications, such as reservoir characterization (Wong, et al., 2005; Anifowose et al., 2015), automated lithology classification (Bressan et al., 2020), natural fracture identification (Leal et al., 2016) and subsurface properties prediction (Akande et al., 2015).

The perceptron is the oldest neural network created by Frank Rosenblatt in 1958. It has a single neuron and is the simplest form of a neural network. Multi-layer Perceptron (MLP) is a widely used feedforward ANN (Mirjalili et al., 2014). This is the simple neural network architecture comprising at least three layers of nonlinearly activating nodes: input layer, hidden layer, and output layer. Input layer does not contain any neuron, it directly takes in the feature

values of a sample. The number of neurons in the output layer depends on the number of classes/targets. An arbitrary number of hidden layers between those two layers are the true computational engine of the MLP (Nicholson, 2019). Learning occurs in the perceptron by changing connection weights after processing a batch of samples. The weights are adjusted based on the amount of error in the model predictions compared to the actual targets. More information about deep neural networks for subsurface characterization is presented by Misra and He (2019) and He and Misra (2019).

Individual classification models are recently challenged by combined pattern recognition systems, which often show better performance. However, combine many same classifiers sometimes does not contribute to anything but the increased complexity of a system. On the other hand, different but much poorer performing classifiers are unlikely to bring any benefits in the combined model (Ruta & Gabrys, 2005). In voting classifier, the optimal set of classifiers is first selected and then combined by a specific fusion method. The voting classifier comes with a variety of voting options, such as hard and soft voting.

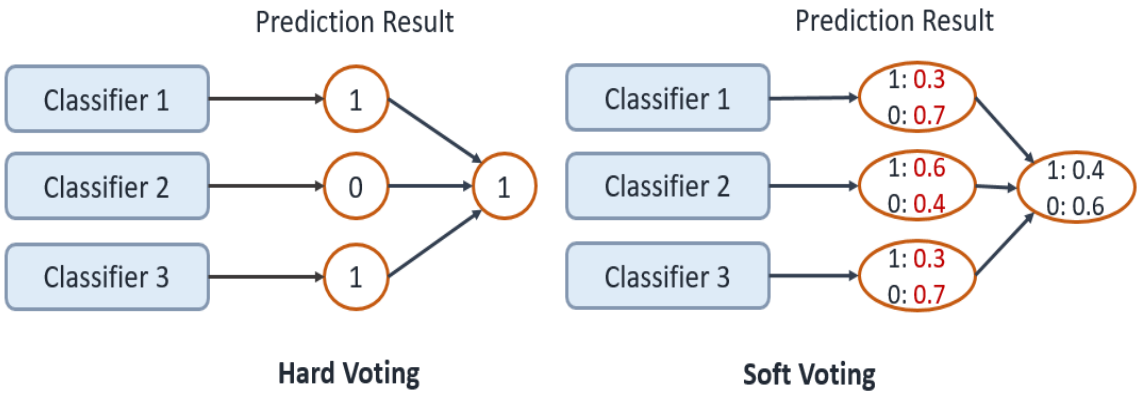

Figure 2-9. The ensemble voting classifier applies three base models to complete two-class classification problem (0 and 1). Hard voting (left side) obtains final prediction result using the most votes from base models. Soft voting (right side) focus on the probabilities for each class from the base models.

Hard voting considers all the prediction results made by different classifiers with majority vote. The majority voting is computed differently when the weights assigned to the different classifiers are equal or otherwise. Soft voting entails the probabilities of prediction classes from each model and picking the highest average probability. Then the label with the greatest sum of weighted probabilities wins the vote. In this study, we use the hard voting of nine selected classifiers including Gaussian Naive Bayes, KNN, SVM, decision tree, RF, Adaboost, MLP, GB, and bagging classifier from scikit-learn. The prediction of each classifier is weighted to make the prediction more accurate.

2.5.2 Data-Driven Classification Metrics

There are several classification metrics used to measure the performance of the classifiers such as accuracy, precision, recall and F-1 score. Accuracy is the proportion of correct predictions among the total number of predictions (Eq. 9).

$$\text{Accuracy} = \frac{\text{TP} + \text{TN}}{\text{TP} + \text{FP} + \text{TN} + \text{FN}} \tag{9}$$

Where TP is True Positive, TN is True Negative, FP is False Positive, FN is False Negative. Precision is the measure of reliability of the assigned positive class. It is the fraction of samples that are true positives out of all the samples that are assigned the positive class expressed in Eq.10. Similarly, recall is the ratio of true positives to the sum of true positive and false negative. High precision and recall mean the model has good identification ability.

$$\text{Precision} = \frac{\text{TP}}{\text{TP} + \text{FP}} \tag{10}$$

$$\text{Recall} = \frac{\text{TP}}{\text{TP} + \text{FN}} \tag{11}$$

F1 score is a harmonic average of calculated precision and recall ensuring a balance between precision and recall. The range of these metrics is from 0 to 1, such that 1 represents perfect model prediction and lower values denote worse predictions.

$$\mathrm{F}-1\ \mathrm{Score} = \frac{2 * \mathrm{Recall} * \mathrm{Precision}}{\mathrm{Recall} + \mathrm{Precision}} \tag{12}$$

2.5.3 Hyperparameter Tuning and Cross-Validation

It is very straightforward to build a data-driven model that is perfectly adapted to the data set at hand. However, the generalizability of the model is always a problem when dealing with new and unseen data. Ideally, we would evaluate the generalization ability of a model using new data that originate from the same population as the data that we used to build the model (Simon, 2003). Neither overfitted nor underfitted model are expected to generalize well, the major challenge is to find the right balance between over- and underfitting.

Hyperparameters are parameters of algorithms that control the learning process and model performance. Hyperparameter tuning is the process of maximizing the model performance by tweaking the parameters of the model. It prevents the model from underfitting and overfitting issues. Grid search is arguably the most basic hyperparameter tuning method. With this technique, we evaluate each model for each possible combination of all of the hyperparameter values provided and then select the architecture which produces the best results. **Table 1** shows hyperparameters range used for selected classifiers. The greatest challenge for this process is computationally expensive and time-consuming.

Table 1. Hyperparameter Tunning Ranges for Classifiers

Algorithms	**Hyperparameters**	**Range**
Random Forest	n-estimators	[50, 100, 150, 200, 300]
	max_depth	[3, 4, 5, 6, 7, 8]

K-Nearest Neighbor	n_neighbors	[5, 10, 15, 20, 30, 40]
Gradient Boosting	n-estimators	[10, 30, 60, 90, 100, 150]
	max_depth	[3, 4, 5, 6, 7, 8]
	learning_rate	[0.01, 0.05, 0.1, 1]
Neural Network	hidden_layer_size	[(100,100), (100,100,100), (100,100,100,100)]
	learning_rate	["constant", "invscaling", "adaptive"]

Cross-validation is another robust statistical method used to prevent models from overfitting by training on subsets of the available input data and evaluating them on the complementary subset of the data (Berrar, 2019). In standard K-fold cross-validation, we need to partition the complete data into k folds. Then, we iteratively train the algorithm on k-1 folds while using the remaining holdout fold as the test set. In this work, all the classifiers are tuned by performing a grid search with 5-fold cross-validation.

2.6 Model performance and Conclusions

2.6.1 Model performance for open discontinuities

First, the numerical experiment is conducted to classify three diverse crack dispersion: 0, 500, 1000, with dominated orientation. The orientation for three dispersions is set as vertical (Orientation = 0°). The dataset includes 15,000 samples, 5000 for each dispersion. Each sample target is either 0, 1, or 2, depending on the dispersion of the crack cluster. The average accuracy of seven classifiers from **Figure 2-10** is around 0.96 for open discontinuities. The best classifiers are gradient boosting and voting classifiers, which give the same precision, around 0.98. Next, four different dominant orientations in the model are the same as the previous cases, and orientations 0°, 45°, 90° and 135° are labeled as 0, 1, 2, 3. The large dataset has 20,000 rows and 84 columns, standing for the features from three different waves. The classifiers' accuracy is 0.95 and 0.99 for dispersion equal to 10 and 50, respectively. The last case identifies different crack

spatial distributions: random, linear, single gaussian and double gaussian. No significant differences were found after added the pressure diffusion to P-wave and S-wave.

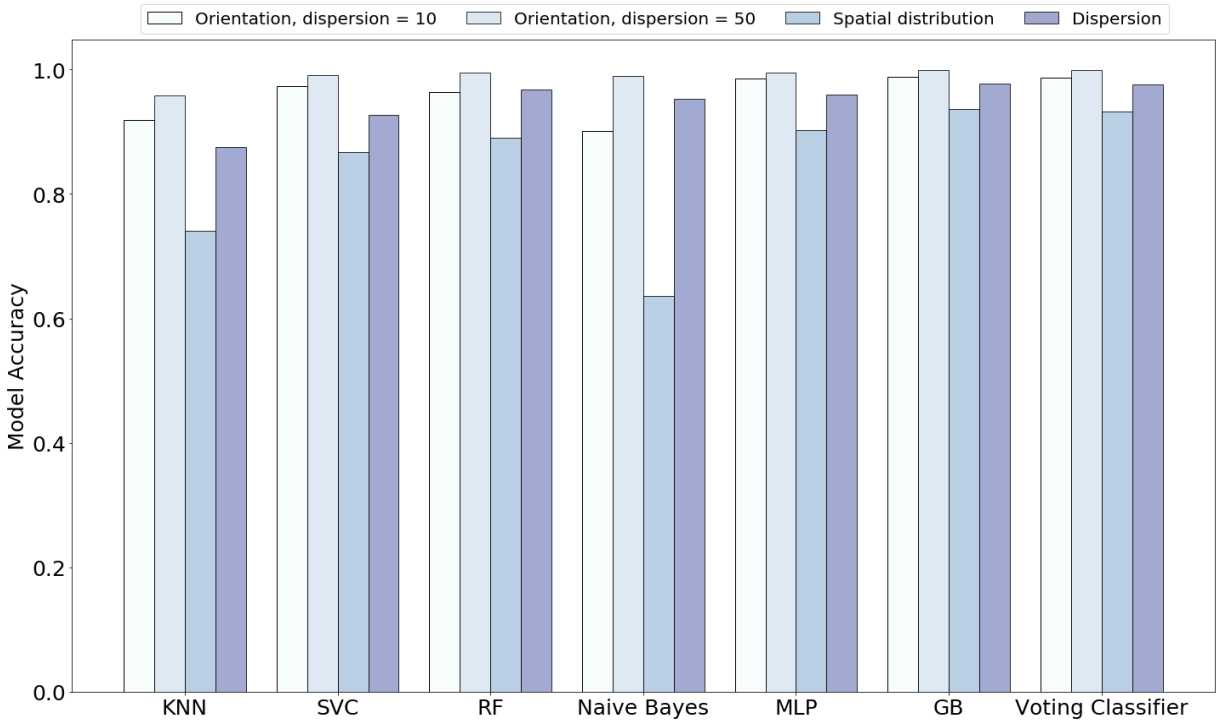

Figure 2-10. Classification accuracy for seven classifiers on four experiments with compressional wave, shear wave and pressure diffusion (P + S wave + pressure diffusion) for open mechanical discontinuities.

The overall accuracy is remaining around 0.85 shows in **Figure 2-10**. Precision, recall, and F-1 score are around 0.92 indicating great model achievement. **Table 2** illustrates precision, recall, and F1 score for both low and high dispersion are good enough. Precision, recall, and F-1 score can even reach 1 at higher dispersion cases, which means the performance of this task is perfect for determining the dominant orientation.

Table 2. Evaluation metrics (precision, recall and F-1 score) from experiments with compressional wave, shear wave and pressure diffusion for open mechanical discontinuities.

Open cracks	**Precision**	**Recall**	**F-1 Score**
Dispersion	**0.98**	**0.99**	**0.99**
Orientation ($\kappa = 10$)	**0.99**	**0.99**	**0.99**

Orientation ($\kappa = 50$)	**1.00**	**1.00**	**1.00**
Spatial Distribution	**0.92**	**0.92**	**0.92**

2.6.2 Model performance for cemented discontinuities

As we mentioned, the embedded closed mechanical discontinuities are filled by limestone. For cemented cracks, we will also discuss four tasks: 1) Dispersion identification, 2) Dominant crack orientation identification for two dispersion (10 and 50), and 3) Crack spatial distribution identification.

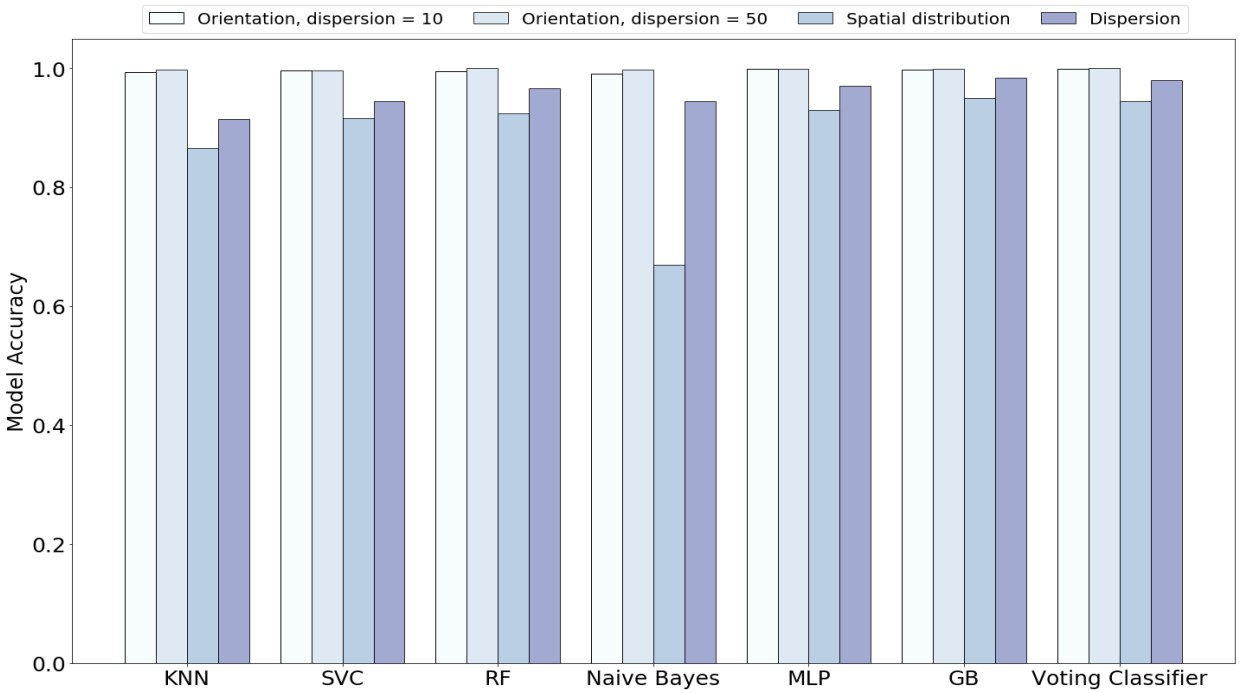

Figure 2-11. Classification accuracy for seven classifiers on four experiments with compressional wave, shear wave and pressure diffusion (P + S wave + pressure diffusion) for cemented mechanical discontinuities.

According to **Figure 2-11,** both lower and higher dispersion cases for orientation classifier can achieve 1.00 when using 84 features in the model. Other metrics such as precision, recall, and F-1 score are also reach 1.00 as shown in **Table 3**. To classify the spatial distribution of crack clusters, the worst model is from Naïve Bayes, which is around 0.67. The other models performed

well with an accuracy in the range of 0.87 to 0.95. Further statistical tests revealed precision, recall, and F-1 score is around 0.93.

Table 3. Evaluation metrics (precision, recall and F-1 score) from experiments with compressional wave, shear wave and pressure diffusion for cemented mechanical discontinuities

Open cracks	**Precision**	**Recall**	**F-1 Score**
Dispersion	**0.97**	**0.97**	**0.97**
Orientation ($\kappa = 10$)	**1.00**	**1.00**	**1.00**
Orientation ($\kappa = 50$)	**1.00**	**1.00**	**1.00**
Spatial Distribution	**0.93**	**0.93**	**0.93**

In general, gradient boosting and voting classifiers are the top two models among the selected seven algorithms. Consequently, the travel time recorded by the 28 sensors for materials containing high-velocity discontinuities (i.e., cemented crack) will have higher information content for purposes of the characterization of mechanical discontinuities.

2.6.3 Feature Reduction and Feature Importance Techniques

The performance of data-driven techniques is highly dependent on the data quality, quantity, and pre-processing steps. However, raw data is often sparse as a consequence of the curse of dimensionality, and analyzing the data is usually computationally intractable. In our case, as the number of features increases by adding wave information, the model becomes more complex. Feature reduction is commonly applied as a preprocessing step to overcome the curse of dimensionality. In general, avoiding overfitting is a significant motivation for performing feature reduction. Otherwise, removing redundant features also helps to save computation time. Feature selection approaches can be divided into filter and wrapper approaches (Kira & Rendell, 1992). Filter methods are often univariate, considering each attribute individually without considering feature interactions and providing scores to each feature. Filter methods use scoring methods, like the correlation between the feature and the target variable.

In our study, we combine chi-square statistic and mutual information approach from the filter method for feature selection. The Chi-Square statistic is commonly used for testing relationships on categorical variables. Mutual information is a different case to measure a relationship between two random variables that are sampled simultaneously. In detail, our work only uses the features in which both chi-square and mutual information scores are higher than 0.2. Consider that the cases for distinguishing crack dominate orientation accuracy have already reached 1.00; we only apply this technique to classify dispersion and spatial distribution to reduce the overfitting and improve model performance. The reduction features create a new training and test dataset with new feature numbers. The number of features selected changes case by case. The new dataset was retrained and tested by the new test samples. Finally, the model performance is reduced by dimensionality reduction from the evaluation metrics like model accuracy and F-1 score. That means all features are highly related to the classification performance.

In machine learning and pattern recognition, a feature is an individual measurable property or characteristic of an observed phenomenon (Bishop, 2006). Features could be powerful, relevant, weakly relevant, or irrelevant (Bootou, 2010). As we discussed, all the features in our model are not deductible. Then we perform a feature importance analysis that aims to provide insight into the relative importance of each feature in determining the outcome. The results of feature importance analysis can be used to optimize the model by removing irrelevant or redundant features or by giving more weight to the most essential features. There are several methods for feature importance analysis in machine learning, including permutation feature importance, mean decrease impurity, and feature importance based on tree-based models.

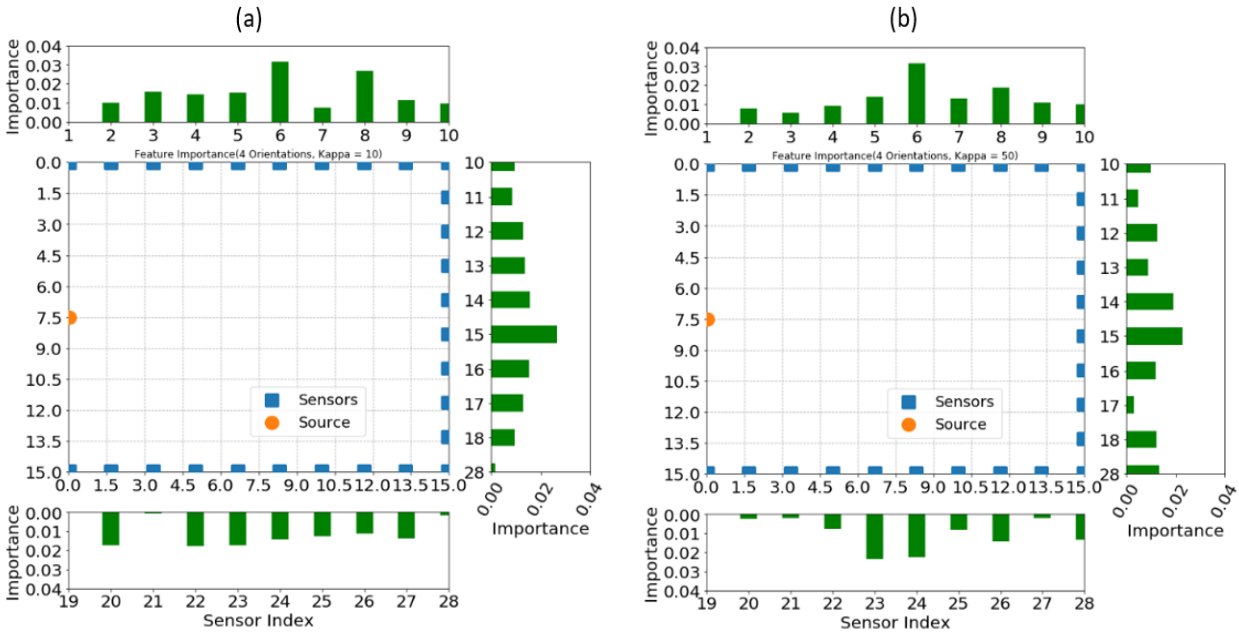

Figure 2-12. Feature importance analysis for dominant crack orientation task. The middle sensors located in each boundary are more crucial than the side sensors. Moreover, the sensors located opposite to the source are the most important as they contain more information about the material.

The basic idea behind permutation feature importance is to randomly shuffle the values of each feature individually and measure the impact of the shuffling on the model's performance. The features are ranked in order of their impact on the prediction performance, with the most important feature being the one that causes the largest decrease in accuracy when its values are randomly shuffled. **Figure 2-12** presents the feature importance of each sensor when identify the dominant crack orientation. It reveals that the middle sensors locate in each boundary, including sensors 6, 14, 15 and 23 are more important than other sensors. The sensors in the middle of each boundary are more reliable and informative for identifying the dominant crack orientation. In contrast, the sensors located at the edges of the boundary are further away from the crack and may be affected by other factors, such as noise or measurement errors.

2.6.4 Conclusions and Discussion

This study presented a noninvasive material characterization method that analyzes the compressional wave travel time detected at multiple receivers (i.e., multipoint measurements). FMM simulation is implemented to simulate the wave front travel time from the sonic wave and pressure diffusion propagation in designed 2D numerical models with open or cemented discontinuities. The arrival times detected by 28 receivers along the material boundaries are used as input datasets to train and test selected seven data-driven methods. As a result, the proposed source-sensor configuration and the data-driven workflow can characterize the dominant orientation, dispersion around the dominant orientation, and the spatial distribution of the cracks. Classification models exhibit the best classification performance in classifying dominant crack orientations. A combination of compressional wave and shear wave is enough to capture the crack information in the material; however, the pressure diffusion can optimize the machine learning algorithms more. Regarding classifiers accuracy, voting and gradient boosting classifier outperform other models in this study, whereas Naïve Bayes methods exhibit the lowest performance. It is to be noted that the workflow performs better on embedded closed discontinuity characterization performs than open discontinuity characterization. Moreover, adding more features to the data-driven model will reduce the difference between the open and closed cracks. In the end, neither reducing feature dimensionality nor adding sensor numbers can improve the algorithms in this study.

CHAPTER III

VISUALIZING MECHANICAL DISCONTINUITIES USING A DATA-DRIVEN REGRESSION*

3.1 Introduction

The fracture process involves two stages, i.e., crack initiation and propagation. The propagation of a crack that results in a fracture provides information about the mode of that fracture. It has become critical to understand the location of the fracture and the extent to which it stimulates a reservoir to plan future drilling and completions. Many experiments have been devoted to studying the crack initiation, propagation path, and eventual coalescence of the pre-existing cracks inside natural rocks or rock-like materials under tensile and compressive loadings (Wong & Chau, 1998; Sahouryeh et al., 2002; Haeri et al., 2014).

In the last chapter, we developed a classifier-based workflow to categorically characterize specific bulk properties of the embedded crack clusters, such as orientation, dispersion, and spatial distribution, by processing multipoint compressional- and shear-wave arrival/travel times (Misra & Li, 2019; Li et al., 2021). However, in the previous works, we did not account for the mode conversion, reflection, and attenuation of the wave propagation and ignored a large amount of the signal behind the first arrival during the analysis. As a replacement for traditional analysis of experimental data, in this work, the combination of machine learning, synthetic data generation using k-Wave simulator, and single-source based multipoint wave-transmission measurements is an effective tool for visualizing/locating the discontinuity. Multiple waveforms are simultaneously processed using a data-driven workflow to non-invasively visualize the propagation of mechanical

* Part of this chapter is reprinted with permission from “A generalized machine learning workflow to visualize mechanical discontinuity.” By Rui Liu, Copyright 2022 Journal of Petroleum Science and Engineering, 210, 109963.

discontinuity through three stages, namely initial, intermediate, and final. Data-driven regression models are used to monitor of the propagation of a mechanical discontinuity by jointly processing the multiple waveforms measured by the multipoint sensor system.

3.2 Workflow

3.2.1 Key Fundamental Questions to be Answered

This chapter aims to answer the following questions:

- How can the entire waveform obtained from K-wave simulation be utilized to enhance the characterization of mechanical discontinuity propagation in laboratory scale rock samples?
- How to detect and locate crack propagation pathway by analyzing the multipoint wave-transmission measurements irrespective of the variations in material composition, density, porosity, and size?
- What is the best strategy for locating the crack propagation pathway by analyzing time-series signal using different feature reduction techniques and data-driven regression model?

3.2.2 Description of Workflow

The primary purpose in our study is achieve robust monitoring of the propagation of mechanical discontinuity in a material by processing multiple waveforms resulting from wave transmission through the material due to a single, impulse source (Liu & Misra, 2022). **Figure 3-1** elaborates the data-driven workflow used in this study. The two main components of the workflow include: 1) wave-transmission data generation using k-Wave; 2) supervised learning to estimate the location, orientation, and length of the discontinuity as it propagates in the material through the three stages. Section 3.3 describes the simulation of elastic wave propagation through

a material with a propagating mechanical discontinuity. Physics-based open-source k-Wave toolbox is used to simulate wave propagation in a 2D material that undergoes three stages of propagation/growth of a mechanical discontinuity. To better simulate the experimental data, the effects of sensor sampling rate and precision of the sensors will also be discussed later. Multipoint waveforms corresponding to each stage of crack growth are recorded by 9 receivers placed around the 2D rectangular material. Each waveform is recorded for 25 microseconds, and discretized into 2500-time steps.

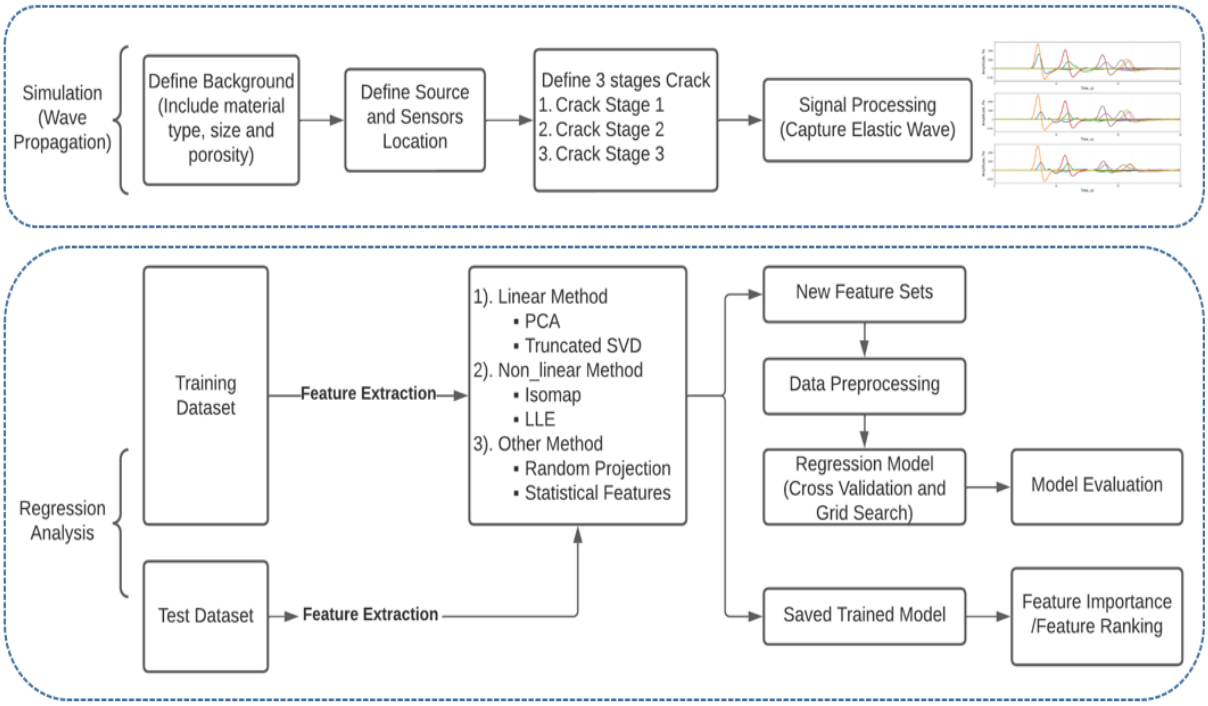

Figure 3-1. Brief overview of the data-driven workflow implemented in this study, which includes simulation of wave propagation, and data-driven regression. Data is simulated to train the regressors to monitor the crack propagation. Feature extraction and data-preprocessing performed on the simulated data prior to training the regressors to reliably monitor the crack propagation.

Overall, we generated a large dataset for 10,000 materials, each undergoing three stages of crack growth with varying lengths, orientations, and locations of cracks. To overcome the curse of

dimensionality, the regression analysis will start with the selection of feature reduction techniques. In Section 3.4, we evaluate the performance of various feature reduction techniques and determine the best feature set to accurately monitor the location, orientation, and length of the crack as it evolves through the three stages of crack propagation. The selected feature sets are divided into training and test sets. The training dataset is used to build the data-driven models, while the test dataset is used to evaluate the generalization of the trained data-driven models. Moreover, during the data preprocessing, involving feature extraction and dimensionality reduction, ensuring that there is no information leakage between the training and testing datasets. The performance of the regressors is evaluated by the root mean square error (RMSE) between the actual and predicted properties of the crack embedded in the material. This metric helps compare the capabilities of the traditional regression models against neural network based regressors.

3.3 Elastic Wave Simulation Model

Many established elastic wave models are developed on low-order finite difference or finite element schemes that require a large number of grid points per wavelength to prevent numerical dispersion (Treeby et al., 2014). K-Wave is an open-source MATLAB toolbox for time-domain acoustic and ultrasound simulations in complex materials (Treeby & Cox, 2010). This toolbox can handle the propagation of elastic waves based on two coupled first-order equations describing the stresses and particle velocities within the material. Moreover, the effects of wave propagation, such as attenuation, dispersion, and multiple modes of propagation, have been considered in k-wave simulation.

3.3.1 K-wave Simulation

This study uses it as an accurate and computationally efficient model for simulating elastic wave propagation. In an elastic medium, the propagation of compressional and shear waves can

be described using Hooke's law and an expression for the conservation of momentum. For viscoelastic materials in which damping or absorption is present, Hooke's law is extended such that the stress-strain relation exhibits time-dependent behavior (Treeby & Cox, 2014). The classical Kelvin-Voigt model of viscoelasticity gives a time-dependent relationship which can be written as equation (13) using Einstein summation notation for an isotropic medium.

$$\sigma_{ij} = \lambda\delta_{ij}\varepsilon_{kk} + 2\mu\varepsilon_{ij} + \chi\delta_{ij}\frac{\partial}{\partial t}\varepsilon_{kk} + 2\eta\frac{\partial}{\partial t}\varepsilon_{ij} \tag{13}$$

Here σ is the stress tensor, ε is the dimensionless strain tensor, λ and μ are the Lame parameters related to the shear and compressional sound speeds by following equations.

$$\mu = c_s^2\rho_o, \quad \lambda + 2\mu = c_p^2\rho_o \tag{14}$$

ρ0 is the mass density. χ and η are the compressional and shear viscosity coefficients.
Equation (13) can be rewritten as a function of the particle velocity vi as equation (15).

$$\frac{\partial\sigma_{ij}}{\partial t} = \lambda\delta_{ij}\frac{\partial v_k}{\partial x_k} + \mu\left(\frac{\partial v_i}{\partial x_j} + \frac{\partial v_j}{\partial x_i}\right) + \chi\delta_{ij}\frac{\partial^2 v_k}{\partial x_k\,\partial t} + \eta\left(\frac{\partial^2 v_i}{\partial x_j\,\partial t} + \frac{\partial^2 v_j}{\partial x_i\,\partial t}\right) \tag{15}$$

where $v_i = \frac{\partial u_i}{\partial t}$. To model the propagation of elastic waves, this is combined with an equation expressing the conservation of momentum. Written as a function of stress and particle velocity, this is given by:

$$\frac{\partial v_i}{\partial t} = \frac{1}{\rho_o}\frac{\partial\sigma_{ij}}{\partial x_{ij}} \tag{16}$$

Elastic wave propagation on the basis of two coupled first-order equations specifying the stress and particle velocity induced within the medium (Treeby & Cox, 2010). A computationally efficient model for elastic wave propagation in absorbing media can be constructed based on the

explicit solution of the coupled equations given in Eqs. (13)- (15) using the Fourier pseudospectral method (Liu, 1999; Caputo et al., 2011).

3.3.2 K-wave Simulation Steps

First, the computational grid is defined using the function makeGrid, which defines the same size matrix as the computing grid. This takes the number and spacing of the grid points in each Cartesian direction and returns an object of the kWaveGrid class. If the Cartesian coordinates do not precisely fit the coordinates of grid points, the output values are generated by interpolation (Treeby et al., 2014).

After the computational grid, the medium properties are defined. For a homogeneous medium, these are given as single scalar values in SI units. For a heterogeneous medium, these are defined as matrices of the same size as the computational grid. Material properties can be stated by variable shear and compressional wave velocities and mass density with no restriction on their distribution or values. There is no restriction on the distribution or values of the material properties. However, a large gap between matrix and crack material properties in our case may lead to unstable, non-convergent simulation. The time step and grid size need to be adjusted to balance the model accuracy and computational cost.

In k-wave numerical models with Fourier pseudospectral, the calculation of spatial gradients using the fast Fourier transform (FFT) implies a phenomenon called wave wrapping. It is displayed as waves leaving one side of the domain reappear on the other side. To solve this problem, a split-field perfectly matched layer (PML) is developed to absorb the waves at the boundaries of domain for free-space simulation (Berenger, 1994). Thus, using PML facilitates infinite domain simulations without increasing the size. By default, it is exerted on a 20 grid-point-

thick layer. For accurate simulation, it is crucial that all the source and sensor do not lie within this layer. In addition, wave propagation effects, such as attenuation, dispersion, and multiple propagation modes, have been largely considered in k-wave simulations. By changing the absorption and thickness of the PML, we could control the reflections and wave wrapping from the boundaries. The absorption within the layer is set by 'PMLAlpha' in Nepers per grid point, default is 2. When the absorption parameters (medium.alpha_coeff and medium.alpha_power) are defined, k-Wave considers the medium as an absorbing material. Nevertheless, high absorption values will need smaller time steps to remain stable.

Next, the locations of the source and sensors are defined on the surface of the material. The numerical models of material containing discontinuities are inspired by the laboratory experiments conducted at the Integrated Core Characterization Center (Bhoumick et al., 2018; Misra & Li, 2019). In those studies, they placed source and multiple sensors/receivers around the porous cylindrical rock to observe the distribution of fractures inside the samples. The source and sensor locations are defined as a set of Cartesian coordinates within the computational grids. If the Cartesian coordinates do not precisely fit the coordinates of grid points, the output values are generated by interpolation (Treeby et al., 2014). Three types of sources are currently accepted in K-wave modeling: initial pressure distribution, time-varying velocity or stress sources. In our study, the initial pressure source is situated at the midpoint of the material's left boundary with nine sensors surrounding the 2D homogeneous material.

Finally, simulation time step is defined by user with kgrid.t_array (0:dt:t_end) or within simulation function (makeTime). The time array must be evenly spaced and monotonically increasing (Treeby et al., 2014). A good discussion is required on Courant-Friedrichs-Lewy (CFL)

condition to balance the computational time and stability. It depends on the maximum speed of sound in the medium and the speed of sound used inside the k-space operator (Mast et al., 2001). Once the input structures are defined, the propagation of the wave field is then computed in simulation function. After each iteration, the pressure changes at the sensor points are stored. Other parameters can also be retrieved by defining them in sensor.record. K-wave simulation has been experimentally validated in many studies (Mallat, 1989; Firouzi et al., 2012; Martin et al., 2019). The visualization of the propagation wavefield and the status bar show that the compression and shear components of the frame are updated every 10 time steps (Treeby et al., 2014).

3.3.3 Experimental Design

There are no restrictions on the values of the material and crack properties. However, a large contrast between matrix and crack material properties may lead to unstable, non-convergent simulation. Material length and breadth are randomly discretized anywhere between 200 and 360 grids with a grid size of 0.3 mm. As shown in **Figure 3-2**, the random samples in stage 3 can be either square or rectangular.

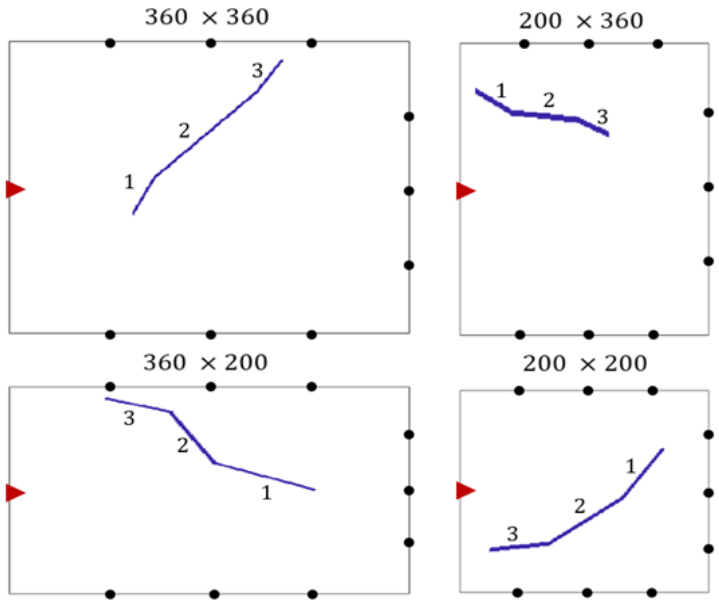

Figure 3-2. Designed Material samples in different size under stage 3 after random crack growth. The red triangle in the left boundary is the impulse source, while the black dots around the material are the 9 sensors. Each sensor records a 25-μs waveform due to the impulse generated by the source.

The red triangle in center of the left boundary is the pressure, impulse source. The black dots around the other three boundaries are the 9 sensors. The sensors on the upper side are marked as sensors 1, 3, and 5. Sensors 2, 4, and 6 are placed on the lower border. The right border has sensors 7, 8, 9. Quartz, calcite, dolomite and clay are chosen as the mineral constituent of the material with variable porosity and corresponding density, velocity and other elastic properties. K wave simulation generated 10,000 samples with different percentages of quartz, calcite, dolomite and clay. The crack locations, orientations and lengths are generated randomly using the Latin hypercube sampling (LHS) method having a width of 0.6mm (3 grids). The orientation and location of the first stage can be anywhere inside the material. For the second stage of crack propagation, the crack can extend any length within the material. In addition, the direction of the propagation during the second stage will be a constant value limited to an angle smaller than 60-

degrees relative to the direction of the crack in the first stage. Similarly, the crack extension in the third stage is also at an angle smaller than 60-degrees relative to the direction of propagation during the second stage. The discontinuities of varying length, orientation, and location are all considered to be filled with fluid with a density of around 800-1200 kg/m^3. Material and crack properties are defined using the density, compressional and shear wave velocity. The elastic waves (body waves) are recorded at different sensors around the crack-bearing materials for 25 μs in three stages.

3.4 Data Generation and Preprocessing

3.4.1 Sampling Rate and Precision

The first two rows in **Figure 3-3** show the waveforms captured for three stages from two random samples. The different colors of the waveforms represent the different sensors around the material. Notably, wave arrival times from 9 sensors in the second row are closer, which indicates a smaller sample compared to the upper sample. But, for both large and small samples, 25 μs is sufficient for sensors to capture the reflections from the boundaries. The sample rate (or sampling rate) of a sensor is the number of samples measured per second. The units for sample rate are samples per second (SPS) or Hertz. The precision of the sensor represents the resolution of the sensor. Sensor sampling rate and precision are configurable to match the experimental objectives.

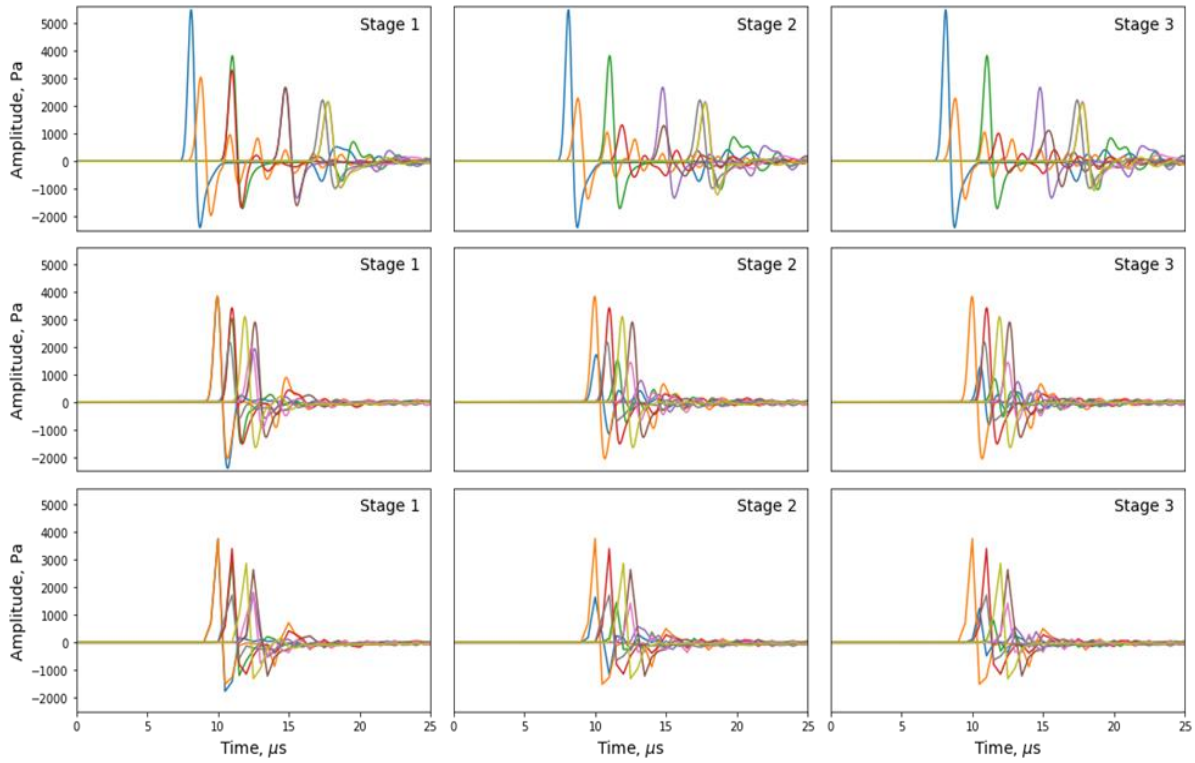

Figure 3-3. First two rows are elastic waveforms captured by 9 sensors around the material from two random samples. The waveforms change with crack propagation through three stages. Different colors of the waveform indicate waveforms recorded by different sensors. The last row is the resampling waveform from realistic sensor with sampling rate of 2MHz and precision of 0.001pa.

In our simulation, 2500 points were captured in 25 μs, which stands for a sampling rate of 100MHz. This is to satisfy the stability of the simulation, however, the physics of the sensor and the process under investigation limit the sampling rate and precision of the sensor. Therefore, we resample the simulated data to 2MHz which much closely match the real experimental conditions. The precision of the sensor represents the resolution of the sensor. A resolution of 0.001pa means that the sensor can detect changes in pressure of 0.001pa. In **Figure 3-3**, the third row displays the waveform from sensor-realistic simulation computer resampling with a sampling rate of 2MHz and precision of 0.001pa. A lower sampling rate and precision may lose parts of the information

in the waveform. Nevertheless, it is necessary for the reliability of the subsequent prediction model and the further applications of this work.

3.5 Data-Driven Regression Models

Regression analysis can discover relationships between features and continuous-valued multiple targets. Features need to be extracted from raw data and dimensionally reduced prior to training the regression model. After feature extraction, the dataset corresponding to each stage of crack growth can be visualized as a table/matrix with 10,000 sample instances as rows, N features as columns, and T continuous-valued targets as columns. The total sample is divided into training and testing dataset. Using the training data, regression model is built as a function of some input parameters. Testing dataset needs to be unseen new data but follow a similar distribution with training data to ensure the generalization performance of the regressor. Validation set is a subset of training data held back from training that is used to monitor and evaluate the model accuracy. Grid search is the most basic approach used for searching any possible combination of hyperparameter space provided, evaluating each model, and selecting the architecture which produces the best results. In addition, K-fold cross validation uses different portions of the data to valuate regressor and access how model perform for an independent test dataset. Finally, multiple continuous-valued targets are the x and y coordinates that define each stage of the crack, i.e., eight target values (four x coordinates and four y coordinates that define the crack propagation from the initial to intermediate then to final stage).

3.5.1 Feature Reduction Techniques

Feature selection/extraction is a critical step in data analysis and machine learning for reducing computational costs, reducing uncertainty due to noise, and improving model generalization (Bolón-Canedo et al., 2015). Designing the optimal dimensionality reduction

workflow for specific predictive modelling requires extensive numerical testing. Principal component analysis (PCA) is a popular multivariate statistical technique which maps data onto a linear subspace and reduces the dimensionality of the variable space by representing it with few orthogonal vectors (Abdi & Williams, 2010). Similar to PCA, Truncated support vector decomposition (SVD) is a matrix factorization technique suited for linear dimensionality reduction. However, it operates on sample vectors directly instead of on a covariance matrix. Moreover, Isomap and locally linear embedding (LLE) are well-known manifold approximation algorithms for nonlinear dimensionality reduction (Chakravarty & Misra, 2021). Isomap attempts to preserve local topology on all scales, mapping nearby points close and distant points far away from each other (De Silva & Tenenbaum, 2002). LLE does the same basic thing as Isomap, except that small neighborhoods are stitched together in a different way (Ventura, 2008).

Random projection includes Gaussian random projection (GRP) and sparse random projection (SRP) can also reduce the dimensionality by projecting the original input space on a randomly generated matrix. Finally, we also extract twenty optimal statistical features from each waveform per sensor per stage of crack growth. This led to 20×9×3 equal to 540 features. The 20 statistical parameters extracted from each waveform include measurements of shape (skewness, kurtosis), central tendency (mean, medium), position (percentile, zero crossing), impurity (entropy) and other statistical parameters. The detailed list of all 20 statistical parameterization-based features and their definitions are elaborated in Appendix A. Similar statistical parameterizations have been used by Foster et al. (2021) to assist machine learning methods.

3.5.2 Data-Driven Regression Algorithms

In this study, we use RF, KNN, GB and neural network (NN) to perform the desired regression to relate the features extracted from the waveforms measured during the three stages of

crack propagation to the location, orientation, and length of crack during each propagation stage. KNN is a non-parametric machine learning method that approximates the association between features and targets by averaging the targets of the K nearest neighbors in the feature space. It is a lazy algorithm that needs all the training data during the testing and deployment phases (Song et al., 2017). KNN delivers a simple, flexible and adequate model for nonlinear problems but is computationally expensive and requires feature scaling.

An RF regression is a bagging technique that constructs several decision trees and aggregates the predictions of all the trees to generate the final prediction. A RF regressor works with data having a numeric or continuous output. Each tree makes its prediction and then takes an average to provide a final prediction result for the forest. The idea of boosting is to add new learners to the ensemble sequentially. The weak learner improves the inadequacy of the model generated by the prior sequence to enhance the model's capability. In this technique, a set of simple learners (decision trees) are combined into a stronger learner by using gradient descent optimization of a loss function (Friedman, 2001; Friedman, 2002). Random forest trains and deploys the trees in parallel, whereas gradient boosting trains and deploys the trees in series. However, gradient boosting is susceptible to overfitting. Pruning a decision tree of gradient boosting helps to prevent overfitting and thus optimize model performance. Shallow decision trees are commonly used as base learners due to their simplicity and robustness in practice (Quinlan, 1996).

NN is a set of computational units that perform linear algebraic summation followed by a sigmoid-based activation. NN has a complex node system with adaptive solid learning capabilities. It is often applied to supervised learning problems that train feature-target pairs and learn to map the correlation between those features and targets. Single layer NN has three components: input layer, hidden layer, and output layer. Data is fed to the input layer, and predictions are made on

the output layer, also called the visible layer. There can be one or more non-linear layers, referred to as hidden layers, between the input and the output layer. Each layer of the neural network has multiple nodes as computational units (Misra & He, 2019). Nodes, or neurons, are the computational units put into each layer that constitutes the neural network. A node on one layer can be fully or partially connected to the nodes on the next layer. A single-layer network can be extended to a multiple-layer network by adding hidden layers. A multilayer perceptron (MLP) is a specific neural network with multiple hidden layers. It is often applied to supervised learning problems that train feature-target pairs and learn to map the statistical correlation between those features and targets. Neural networks are susceptible to overfitting and hard to design optimally. No unique rule has been found for determining the best configuration for the network structure (i.e., the number of hidden layers, number of input nodes, type of activation function, and number of nodes in each hidden layer).

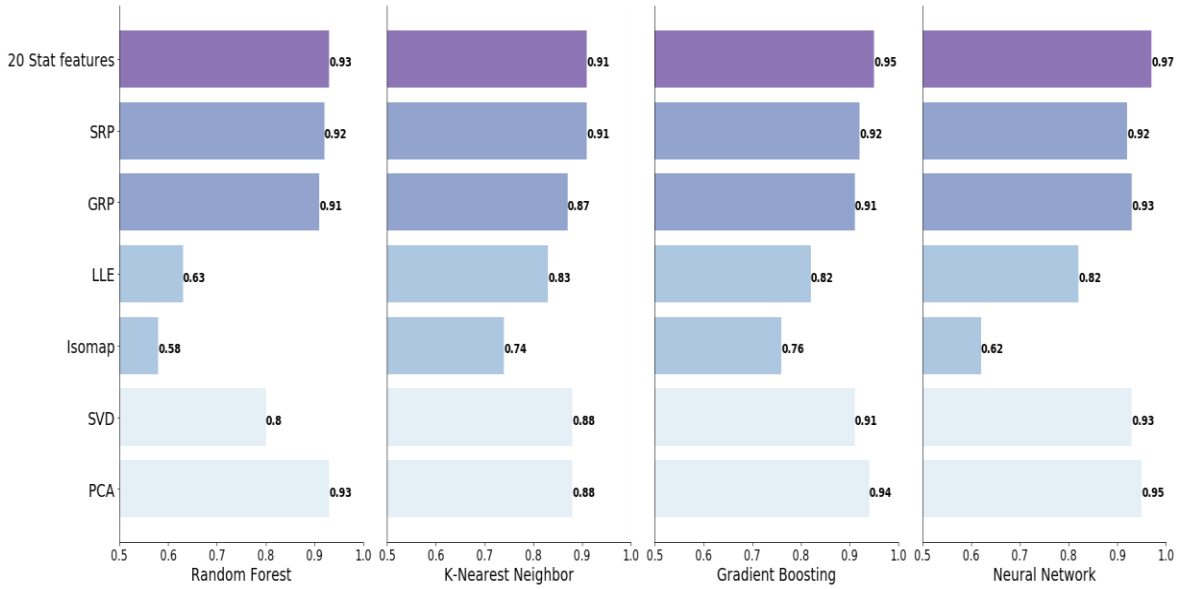

Figure 3-4. Generalization performances of the four regression methods for the seven different feature extraction techniques. Neural network and gradient boosting enable the best monitoring of crack propagation. Statistical parameterization and principal component analysis-based features enable the best monitoring of crack propagation.

Hyperparameter tuning is applied with grid search to optimize the trained regressors for the best performance on the test data. **Figure 3-4** compares the testing performances of RF, KNN, GB and NN for the seven different feature extraction methods discussed in the previous subsection. The numbers labelled in the figure are provided to assess the performance of the regressors, in terms of R-squared, which provides a measure of how well the predictions replicate the crack properties in the testing samples as a proportion of the total variations in crack properties. The performances presented indicate that neural networks and gradient boosting are more accurate than KNN and random forest for the prediction problem under investigation. Regarding the feature extraction techniques, features obtained through statistical parameterization and those obtained using principal component analysis led to more accurate regression performance as compared to the remaining five techniques. For most of the feature extraction techniques, KNN has the lowest performance. Topology-based feature extraction led to lower regression performance, where Isomap had the lowest performance and LLE had a slightly higher performance than Isomap.

3.6 Results

3.6.1 Prediction Results

The train-test split is a technique to evaluate model performance by randomly splitting the original dataset into two subsets. In this section, we will explore the influence of different train-test split percentages on the evaluation of regression models. Random selection is necessary to ensure both training and testing datasets are representative samples of observations. A rule-of-thumb for machine learning is dividing 80% of the samples into a training set and the remaining 20% as a testing dataset. Furthermore, we also build a model with 50:50 split proportion. With more testing datasets, the evaluation metric will have enough points to reflect the real model

performance. From another perspective, if the training set is insufficient, the model may suffer high variance as a result. **Figure 3-5** demonstrate how training and testing split affects the regression model error in 20% testing samples and 50% testing samples with the optimal regression model after hyperparameter tuning with cross validation. Violin plot is a hybrid of box plot and kernel density plot shows distribution of numeric data for one or more groups. **Figure 3-5(a)** is a split violin plot that compares the 20% testing dataset error distribution (blue part) and 50% testing dataset error distribution (orange part). The calculation of the error is calculated as the expression:

$$\text{Error} = \frac{\text{absolute grid error in x dimension}}{\text{Nx}} + \frac{\text{absolute grid error in y dimension}}{\text{Ny}} \tag{17}$$

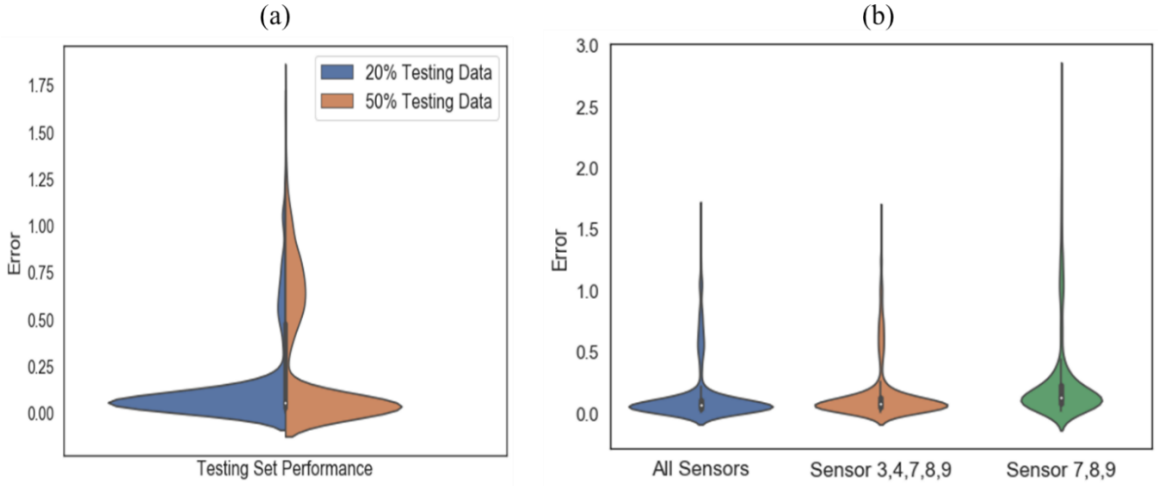

Figure 3-5. Violin plots for error distribution of regression model and sensor optimization. (a) Split violins for on 20% (2000 samples) testing and 50% (5000 samples) testing dataset. (b) Sensor optimization with three cases: (1) 9 sensors: three sensors uniformly distributed on each side except for the side where the source is located. (2) one sensor at the top (sensor3) and the bottom (sensor5) border and three sensors at the opposite boundary (sensor 7,8,9) to the source. (3). Only sensor 7,8,9 at the opposite border to the source.

The white middle point is the median which inside the black box represents the interquartile range. The thin black line is 1.5 times the interquartile range. The peaks, valleys, and tails of the

density curve can be compared to find where two groups are similar or different in a split violin. A wider section of the violin part means a higher probability that data fall in that range. Skinner's shape represents a lower probability. By comparison, most of the errors from the two models are smaller than 0.25. However, the left side of the violin has a broader peak and fewer outliers corresponding to a more stable and accurate model performance.

An optimization of sensors placement optimization is carried out to minimize the number of sensors without losing any information for the regression model. In the original model, we have 9 sensors located in three boundaries except for the boundary where the source is placed. Then, we test the regression model with one sensor at the middle of the top (sensor 3) and the bottom (sensor 4) boundary and all three sensors (sensor 7, 8, 9) at the opposite boundary. We further reduce sensor numbers to only three sensors on the opposite border, as they contain more information from feature importance analysis (Liu & Misra, 2022). **Figure 3-5(b)** displays the violin plots for three sensor conditions. It is apparent that 5 sensors could have similar results with 9 sensors for different material sizes in 2000 testing set. However, the further reduction will affect the detection results. It suggests that for future work, one sensor in the top and bottom boundary, and three sensors at the opposite boundary will be sufficient for the discontinuity boundary for both large and small materials.

The performance of the regression models is evaluated using root mean squared error (RMSE), which is the standard deviation of the residuals (prediction errors). Compared to mean absolute error, RMSE is preferred when large errors are particularly undesirable. **Figure 3-6** is a boxplot displaying the distribution of RMSE of the predictions obtained using the data-driven regressors.

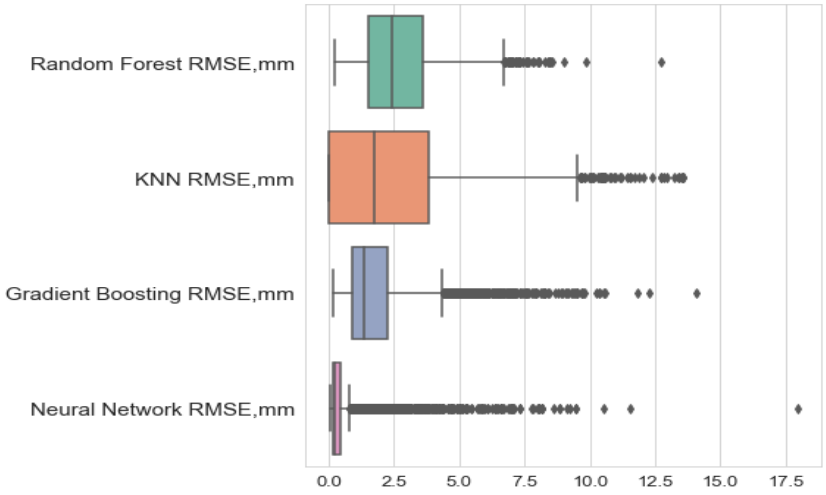

Figure 3-6. Box plot of root mean squared errors for various regression methods for the task of monitoring the crack propagation. Distribution of RMSE for predictions of crack path when monitoring the crack propagation for the 4000 testing samples.

The boxplot includes five important vertical lines: minimum, first quartile (Q1), median, third quartile (Q3), and maximum. In the boxplot, the outliers are shown as individual points. It is apparent from boxplots that 75% of errors in the neural-network predictions are lower than 2.5mm. The other three prediction models also perform well with a maximum error of less than 10mm. All in all, the neural network regressor performs the best both in terms of accuracy and computational cost.

To visualize the predicted results, we get some random samples in stage 3 presented in **Figure 3-7**. The red line segments represent the known crack path as the crack propagated from stage 1 to stage 3, while the blue line segments are the neural network model estimations based on the data-driven processing of the multipoint waveform data. The known and the predicted crack paths show a striking similarity. Notably, the proposed model can precisely estimate the location, orientation, and length of the crack as the crack grows. Alternatively, the data-driven boosting algorithm model for crack growth is a useful supplement to the existing methods. The accuracy of this model could meet the requirement of discontinuity detection.

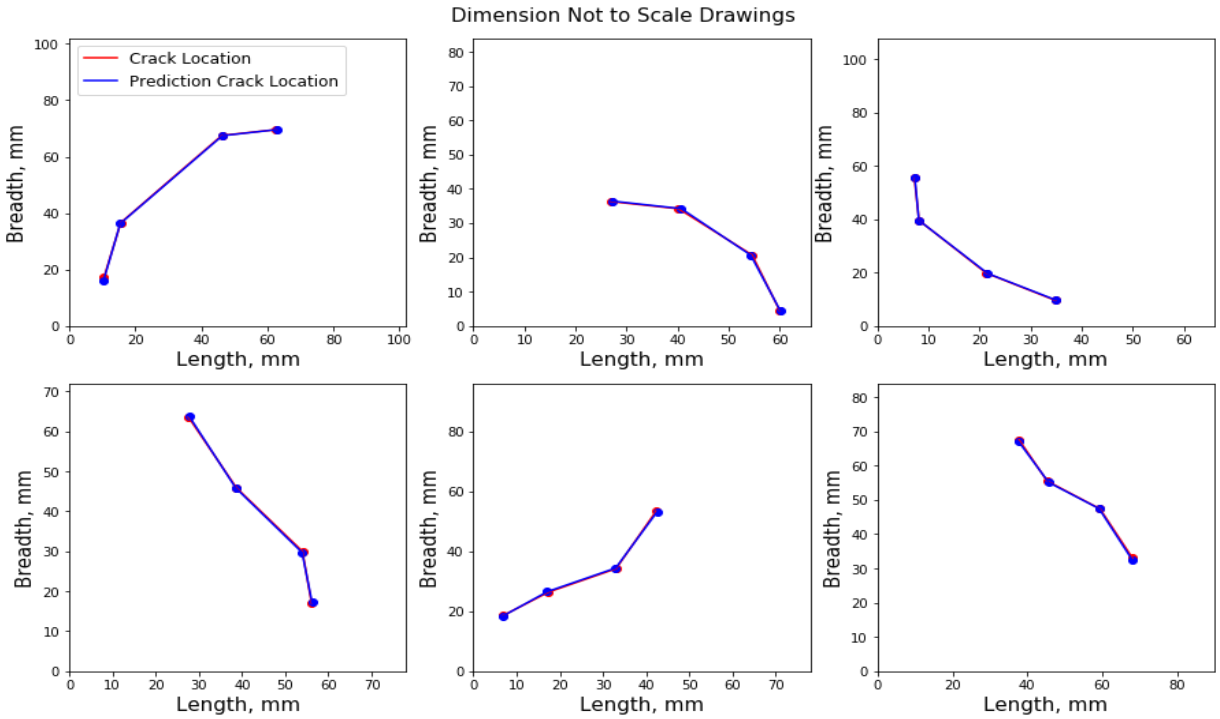

Figure 3-7. Data-driven approach monitoring of crack propagation from initial to final stages by processing multipoint waveforms recorded in 9 sensors. Regression performance visualization for 6 samples from 20% (2000 samples) testing dataset.

3.6.2 Feature Importance Analysis

Feature ranking is the process of sorting the importance of features. We could use the permutation-importance testing and the SHAP (Shapley Additive explanations) impact for feature ranking. This ranking informs which feature has the highest importance for the desired monitoring of the crack propagation pathway. Permutation-based feature ranking is defined as the reduction in the model's prediction performance on the testing dataset when a specific feature is randomly shuffled (Breiman, 2001) while preserving the originality of all other features. When the permutation is repeated, the results might vary.

SHAP or Shapley value is computed using a method from coalitional game theory (Shapely, 1971; Shapely, 1988). While the Shapley value was originally used to quantify the

contribution of each player to the game, and later developed to quantify the contribution of each feature to the prediction of the model. SHAP values determine the importance of feature by comparing the results of different combinations of the feature. For example, if we have three features (A, B, C) in the dataset, we could have 2^3 $(\emptyset; A; B; C; AB; AC; BC; ABC)$ possible combinations to predict the target. Each different combination trains a unique prediction model. Thus, we will have 2^3 models and corresponding predictions. Then shapely value is the average marginal contribution of an instance of feature among all possible coalitions. To evaluate the contribution of A, we could calculate the marginal contribution for subsets with/without A and summarized by weighted average.

$$\text{Shap (A)} = w1 * MC_{A,\{A\}} + w_2 * MC_{B,\{A,B\}} + w_3 * MC_{C,\{A,C\}} + w_4 * MC_{\{B,C\},\{A,B,C\}} \quad (18)$$

where MC is the marginal contribution measured by the difference of two outcomes with two subsets. w_1, w_2, w_3, w_4 are weights ($w_1 + w_2 + w_3 + w_4 = 1$).

SHAP Explainer can provide an explanation for many different ML algorithms, such as tree-based models with TreeExplainer, linear models with LinearExplainer, and neural network models with KernalExplainer. The superiority of SHAP value over permutation feature importance is that tree-based SHAP is fast implementation with positive and negative impacts. The idea behind SHAP feature ranking is that simple features with large absolute SHAP value are important. **Figure 3-8** shows the results obtained from given global or local importance of statistical features in testing dataset.

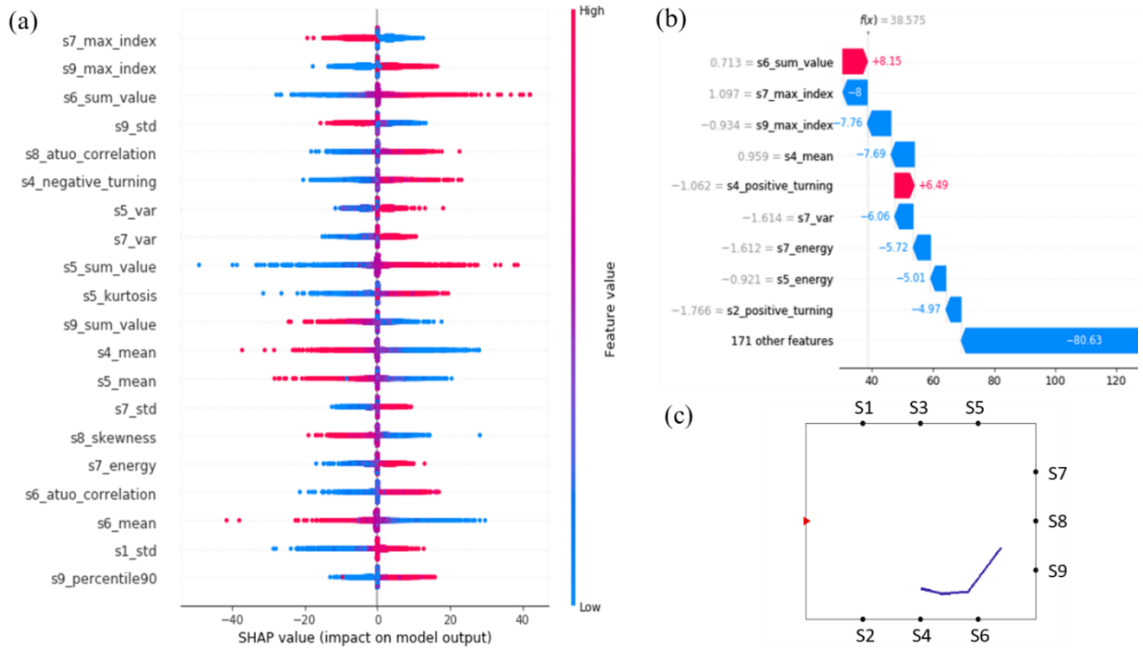

Figure 3-8. Feature importance with SHAP: (a) The summary plot combines feature importance with feature effects. (b) Waterfall plot with SHAP values for a random sample in testing dataset. (c) Diagram of sensor location. Top table group top 20 important features according to their causality.

Figure 3-8(a) sorts the global importance by the sum of SHAP value per feature across all samples in the testing set with the neural network-based explainer. This summary plot combines feature importance from the most important at the top to the least important at the bottom with feature effects. The top features in feature ranking contain significant helpful information for prediction. It consists of several sample points with vertical positions showing the feature name, horizontal positions showing the impact on the model output, and color indicating the feature values from low (blue) to high (pink). Many overlapping points are jittered in the y-axis direction, hinting at the distribution of SHAP value for each feature. In contrast to the mutual information non-linear correlation, the top three features importance to the target became the index of wave peak, the sum value of all signal points and standard deviation. If compared from a sensor perspective, it is notable that S7, S8, S9 contain more information on the problem of crack

detection in terms of both mutual information correlation and feature ranking. As the sensor locations are labelled in **Figure 3-8(c)**, they are the sensors located at the opposite boundary from the pressure source. This provides a great overview of the model, but we might want to delve into a single sample. As presents in **Figure 3-8(b)**, the waterfall plot gives the importance of features based on a randomly selected sample. This ranking varies sample by sample to local feature importance.

3.6.3 Conclusion and Discussion

An important objective of this paper is to develop a generalized machine learning workflow that can successfully visualize mechanical discontinuity by accurately predicting the location, orientation and length of a mechanical discontinuity embedded in a material of any composition, velocity, density, porosity, and size. The study is based on the hypothesis that the use of robust signal processing followed by machine learning can identify small differences and minute patterns in the waveforms recorded at multiple locations due to the presence of mechanical discontinuity; following that, machine learning can use those differences/patterns to predict the location, orientation, and length of the embedded discontinuity.

To that end, the designed workflow successfully monitored the propagation of mechanical discontinuity by processing multipoint sensor measurements of waveforms resulting from the interaction of a wave transmission with the mechanical discontinuity. The data-driven workflow can successfully predict the location, orientation, and size of mechanical discontinuities by identifying small differences and minute patterns in the waveform in 0.003s per sample. The monitoring of the three stages of evolution of the mechanical discontinuity has a median RMSE lower than 2.5mm in the material. A neural network (NN) based regression model significantly outperforms all other regression models.

CHAPTER IV

DISCOVERING THE CAUSAL SIGNATURES FOR THE EVALUATION AND IDENTIFICATION OF MECHANICAL DISCONTINUITIES*

4.1 Causal Inference

In the eighteenth century, philosopher David Hume pointed out the conceptions of causality in terms of repeated "conjunctions" of events (Hume, 1751). Hume claimed that the labelling of causality relies on the empirical regularities involving previous phenomena (Eagleman & Holcombe, 2002). In other words, we cannot confirm the inevitability between cause and effect; instead, we can only understand the repeated connection between cause and effect through observations. Judea Pearl (Pearl, 1998; Pearl, 2009) provided a comprehensive causation study with significant applications in the fields of statistics, artificial intelligence, economics, cognitive science and health science. In fact, there are several well-established and operational causal models in many fields that accurately reflect our intuitive understanding of cause and effect and can be described in precise mathematical terms.

4.1.1 Cause and Effect

The departure of cause and effect analysis is given by famous statistician professor Donald Rubin (1974, 1977, 1978, 1980). Now, cause and effect (or causality) is known as the relationship between events, where an occurrence of an event (e.g. change in a property) causes an occurrence of another event, such that the cause precedes the effect. It is important to note that the later event may have multiple causes in the past and may lead to multiple effects in the future. The essence of

* Part of this chapter is reprinted with permission from "Monitoring the propagation of mechanical discontinuity using data-driven causal discovery and supervised learning." By Rui Liu, Copyright 2022 Mechanical Systems and Signal Processing, 170, 108791.

the cause-effect relationship is the generation or determination of one event by another event. Donald Rubin proposed a potential outcome framework, also called Rubin causal model, to understand causal mechanisms (Rubin, 2005). The inability to simultaneously know the potential outcome/effect and observed outcome/effect is the fundamental problem of causal discovery. To overcome this problem, we need to design a treatment group and a control group to compare the differences in outcomes with and without the cause. In general, treatments are applied to the samples in the treatment group, while no treatments are applied to the samples in the control group. The treatment serves as the cause. The presence and absence of treatment cause varying effects/outcomes. Individual treatment effect (ITE) estimation aims to compare the different outcomes with and without the treatment of a specific unit. The average treatment effect (ATE) measures the average difference between the outcomes for the treatment group and the outcomes for the control group. ATE enables the quantification of causal relationships when performing data-driven causal discovery. It is expressed as:

$$\mathrm{ATE} = \mathrm{E}[\mathrm{Y}_1 - \mathrm{Y}_0] \tag{19}$$

where E is expected value, Y_0 is outcome wound occur for individual if they are not treated and Y_1 is outcome wound occur for individual if they are treated. By definition, we estimate the ATE by a comparable set of differences in outcome with and without treatment.

Another metric, ATT is the causal effect of the treatment for individuals in the treatment group, defined as:

$$\mathrm{ATT} = \mathrm{E}([\mathrm{Y}_1 - \mathrm{Y}_0]|\mathrm{T} = 1) \tag{20}$$

Where, $\mathrm{T} = 1$ means treatment group. The way can distinguish between the two is that ATE is the average causal effects in the population under consideration. ATT, on the other hand, is the average causal effect for the treatment group only. In other words, ATT is pre-post difference in the

treatment group. They are not good or bad, which to use just depends on what your problem is. For example, ATT tells us what the effect with different drug treatment is, while ATE tells us what the effects of people taking or not taking the drugs are. Medical studies typically use ATT because they often only care about the causal effect of administering a drug for various patients. Additionally, in reality, we do not always have both control and treatment groups. In this example, if a person takes the medication, then the result of that person not taking the medication does not exist. Therefore, in non-experimental studies, causal discover is fraught with uncertainties. Causal relations could only establish by careful attention to all relevant variables and should involve active manipulation as final confirmation.

Confounding variables (or confounders) are often defined as extraneous/irrelevant variables whose presence affects the variables under study, leading to an erroneous obscuring or emphasizing of their relationship (MacKinnon et al., 2000). Since confounders obscure the real effect of a treatment on the outcome, the confounders need to be eliminated as much as possible (Jager et al., 2008). There are various ways to exclude or limit the influence of confounders, which include randomization, restriction and matching. To give a simple example, **Figure 4-1** is a causal graph tries to find out if taking medication affects the disease. The fundamental problem in causal inference is that one outcome is observed factual outcome, while another compared outcome is always counterfactual outcome in the same unit (Holland, 1986). That is why we need to have a treatment group and a control group for comparison. The treatment group was those who took the drug, while the control group was those who did not. Next, by comparing the disease changes in two group we could get treatment effect. However, individuals in two groups are always differed on other variables. In this case, people who decide to take the drug are older than people in control group. Age may affect both the disease status and whether they remember to take their medication.

Therefore, the effects from the confounding variable (age) are also accounted for when calculating ATE, which led to a spurious effect. There might be a correlation between taking medicine and disease either because of the causal path or the confounding correlation path through age/gender. Note that if the variable differed between the treatment and control group, but had no association with the outcome, then that parameter would not be considered a confounder. Causal inference is a practical technique to eliminate the different qualities/confounders between the two populations and make them comparable with different statistical methods.

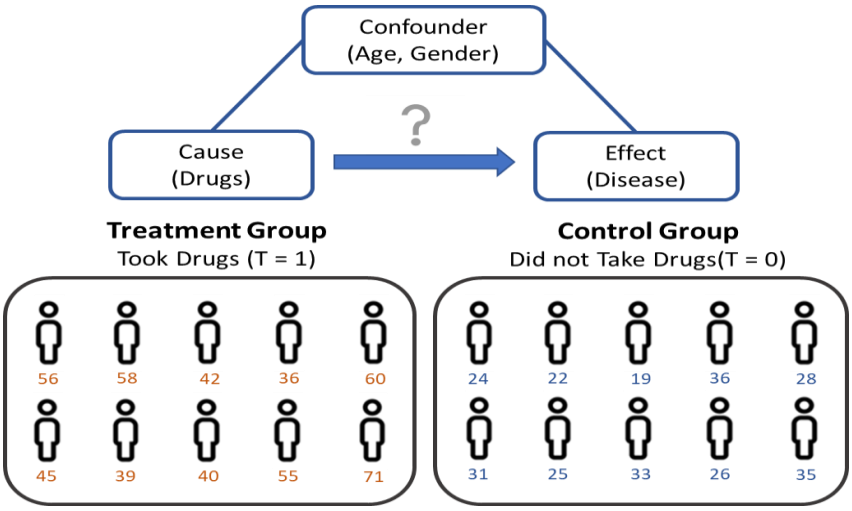

Figure 4-1. Causal diagram to measure whether the drug will cure the disease. Treatment group subject receives a specific drug and those in the control group do not receive drug. The orange and blue number under individual is age. Then the age or unknowledge gender as difference between treatment and control group which also influence the outcome are confounders need to consider for causal analysis.

4.1.2 Causal Inference Toolbox

We are witnessing a highly accelerated phase of progress in artificial intelligence and machine learning. they have significantly progressed in many complex tasks from different areas. Supervised learning is good at training to learn a very accurate mapping from inputs to outputs, whether they are images, sentences, signals, etc., from large amounts of labelled data. However,

current machine learning algorithms have fundamental limitations. It should be noted that an acknowledgement of supervised learning's shortcomings does not in any way diminish its success. Firstly, the trained machine learning may perform poorly in a new environment. In real-world tasks, the testing set is often distributed differently than the training data. Secondly, most machine learning algorithms, especially deep learning remain 'black boxes' that are unable to explain their predictions and recommendations. Prediction models are purely focused on correlation features, while correlated things may not even relate (Niles, 1922; Duesberg, 1998). Correlation based methods can lead astray. In addition, intelligence outcomes should not solely rely on data but also incorporate domain knowledge. Suppose the learning direction is a cause-and-effect relationship, all input features are potential effects/causes of the label in supervised learning, and it is possible to reach the next AI state. Intrinsically, causality facilitates prediction because finding causal relationships is crucial for building explainable machine learning models. Causality suggests the primary mechanism of a process being modelled by the data-driven model. However, the current evaluation of data-driven models and machine learning algorithms are primarily focused on the statistical correlation between the features and targets rather than potential causality.

In recent years, several studies have examined the connection between machine learning and causality (Scholkopf, 2019; Guo et al., 2020; Moraffah et al., 2020). Causality research can generally be divided into two main branches: causal discovery and causal inference (Nogueira et al., 2022). Actually, these two tasks are antipodal. The former focuses on estimating causal relationship between variables directly from observational data without making any assumptions. The latter assumes the causal relationships at the beginning and then aims to quantify the causal impact deriving from a change of a cause over an outcome of interest. The causal graph is a

directed acyclic graph (DAG) that depicts the causal-effect relationships between variables with the hypothesis. Despite the availability of various frameworks and methods for causal inference in numerous toolboxes, most of them suffer from a lack of robust validation and reliable implementations. Causal inference is a framework used to address causal conclusions by using a particular model. There are two popular models used for causal inference. One is the potential outcome framework, also known as Rubin causal model (RCM). Another one is structure causal model (SCM) proposed by Professor Judea Pearl in 1995 (Pearl, 1995). RCM and SCM are in fact strongly equivalent. However, when it comes to event-based causality, SCM is considered the most well-established and widely used model. Hence, this paper will introduce the SCM according to its development concept.

Table 4. Python toolbox for causal analysis with pros and cons

Library Name	Description	Advantages	Disadvantages	License
Causal Discovery	Causal Discovery Toolbox (CDT) is an end-to-end package aimed at learning causal graphs from observations.	• Unify pairwise and score-based multi-variate approaches within a single package.	• Hard to validate causal graph. • Do not take advantages of machine learning.	MIT license
CausalNex	CausalNex uses Bayesian Networks to uncover structural relationships in data by combining machine learning and domain expertise.	• Able to visualization the causality. • Able to adjust structural model easily.	• Hard to validate the structure graph.	QuantumBlack
EconML	EconML applies the beauty of machine learning algorithms to measure the causal and effect of observational or experimental data.	• Algorithms could improve the computational cost of causal analysis.	• Do not provide causal graph.	Microsoft
DoWhy	DoWhy is a causal inference library focuses on modeling causal assumptions and validating them.	• Effective even with unobservable confounders. • Combine features from EconML. • Focus causal inference on identification and frees up estimation using any available statistical estimator. • Automated robust check on the obtained estimate.	• Reliable assumption needed.	Microsoft
Causal ML	Causal ML provides tree-based and meta-based algorithms to estimate causal impact of intervention on outcome.	• Stable and allow to estimate CATE and ITE.	• Fewer functions and models. • Do not provide causal graph.	Uber Technologies
Causallib	Causallib is a Python package for Causal Analysis which allows a complex learning model with the fit-and-predict method.	• Causal analysis API unified with the Scikit-Learn API. • Build-in evaluation plots.	• Do not provide causal graph. • Limited causal models.	IBM

Table 4 presents an overview of well-documented computational tools for performing causal inference in Python. Each library provides various statistical methods for causal analysis with its advantages and disadvantages as well as the scope of application. There are multiple

Python packages that implement various statistical and econometric methods within the causal inference framework. Causal inference may seem tricky, but almost all methods follow four key steps: 1). Model a causal inference problem using assumptions. Researchers need to create an underlying causal graphical model for each problem. 2). Identify an expression for the causal effect under these assumptions. 3). Estimate the expression using statistical methods such as propensity score-based approach or double machine learning. 4). Finally, verify the validity of the estimate using a variety of robustness checks. Causal discovery, CausalNex and DoWhy can provide graphs through analysis to describe and visualize causality of the dataset. However, it is hard to validate the provided causal graph/causal structure. In this situation, the combination of DoWhy and EconML is a powerful and comprehensive solution that covers numerous algorithms, model validations, and interpretation techniques (Zhao & Liu, 2023).

4.1.3 Methodology

Generally speaking, causal models are mathematical models representing causal relationships within a given system or population (Hitchcock, 2020). Many algorithms for estimating causal effects have been developed in recent years. We review a non-exhaustive list in **Table 5** of causal inference methodologies from EconML and DoWhy, discussing their advantages and disadvantages. Drawing causal inferences in observational data without randomization is challenging due to the different qualities/confounders between the two populations. The rough idea is to do some "balancing" of the samples from the treatment and control groups for reasonable comparability.

Table 5. Summary of the pros and cons used to control confounding in observational studies

Selected Algorithms	Advantages	Disadvantages	EconML	DoWhy
Propensity Score Matching (PSM)	• PSM is conceptually straightforward for non-technical audience. • PSM make well balanced samples in treatment and control groups. • PSM performs well with high number of confounders.	• Unmatched samples excluded from the analysis. • Requires more control samples than treated samples.		✓
Inverse Propensity Score Weighting	• Compared to PSM, IPSW retains all study samples with pseudo population. (No excluded samples) • Simple to analyze, present and interpret.	• IPSW can be unstable when extreme weights occur.		✓
Propensity Score Stratification	• A simple and intuitive method to divide samples into groups according to various covariates.	• It is inherently limited because one can only control for a few covariates at once.		✓
Double Machine Learning	• DML offers an data-driven way to control confounding effect in observational studies. • DML allows to utilize powerful prediction methods for causal analysis in high dimensional dataset.	• Sample-splitting and cross-fitting are needed to get rid of the other sources. • DML is mathematically complex compare to propensity score-based approaches.	✓	
Doubly Robust Learning	• DRL maintains many favorable statistical properties related to the final model (e.g. small mean squared error, asymptotic normality, construction of confidence intervals). • DRL debiases model by combining regression model and propensity model.	• DRL is typically has higher variance estimation. • Computational cost is higher compare to other approaches.	✓	

Propensity score analysis describes a family of statistical techniques that are effective for accessing treatment effects (Guo & Fraser, 2014). The propensity score is a balancing score which estimates the conditional probability of receiving the treatment, given the observed covariates (Rosenbaum & Rubin, 1983). Formally, defining the propensity score as:

$$e(w) = P(T = 1|W = w) \quad (21)$$

Where, $e(w)$ is the propensity score, T is the treatment, W is the confounders. Propensity score can be calculated from logistic regression. There are two popular strategies that use propensity scores-based model to reduce selection bias between treatment and control group: matching and inverse propensity weighting (IPW) (Xu et al., 2010). Propensity scoring matching (PSM) is a statistical matching technique the balance the potential covariates in the treatment and control group (Caliendo & Kopeinig, 2008). Matching the similar propensity score can significantly reduce the observation number, particularly if the sample pool is already small. PSM matching may seem appealing at the first glance, but there have been numerous debates and studies

highlighting the potential pitfalls associated with PSM. They believe PSM can match very different observations just because they have similar propensity scores. IPW includes sample weight defined as the inverse of the propensity. Inverse-probability weighting removes confounding variables by creating a "pseudo-population" with weighting. Specially, the weights are defined as $w_1 = \frac{1}{e(w)}$ for treatment group, $w_0 = \frac{1}{1-e(w)}$ for control group. Although propensity score analysis may be used to assemble comparable study groups, the quality of the propensity score model depends on the quality and size of the available data and how the model was built (Haukoos & Lewis, 2015).

Double Machine Learning (DML) is a method for understanding the causal effect without being unduly influenced by the covariates. This idea has been introduced and developed by Chernozhukov et al. in a series of papers (Chernozhukov et al., 2016; Chernozhukov et al., 2017; Chernozhukov et al., 2018). It provided a general framework to estimate estimating causal effects with confidence intervals using machine learning techniques. With the known DAG in **Figure 4-2**, we could define the following partially governing equations. Here for better explanation and interpretation, we only use one confounder and assume a linear model in this DAG.

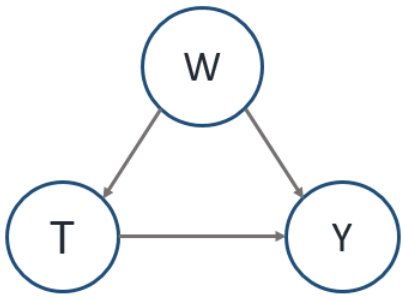

Figure 4-2. Example represented as a DAG: T is the treatment indicator, Y is the outcome, and W is a confounder.

$$Y = \theta_o T + g_o(W) + U, E[U|T, W] = 0 \quad (22)$$

$$T = m_o(W) + V, E[V|W] = 0 \quad (23)$$

Where, Y is the outcome, T is the treatment, W is confounder, and U and V are disturbances. In equation 22, θ_o is the average causal effect that we would like to estimate. Nuisances functions $g_o(W)$ and $m_o(W)$keep tracking the influence from confounder. The confounding factors affect the treatment via function $m_o(W)$and the outcome variable via function $g_o(W)$. A naïve approach to estimate θ_o is construct regression estimator for function $Y - g_o(W) = \theta_o T + U$. However, regularization bias occurs between θ_o and predicted $\widehat{\theta_o}$ without considering the effect of W on T.

$$\widehat{\theta_o} = \left(\frac{1}{N}\sum_{i\in N} T_i^2\right)^{-1} \frac{1}{N} T_i\left(Y_i - g_o(W)\right) \tag{24}$$

$$\begin{aligned}\sqrt{N}\left(\widehat{\theta_o} - \theta\right) = &\left(\frac{1}{N}\sum_{i=1}^{N} T_i^2\right)^{-1} \frac{1}{\sqrt{N}}\sum_{i=1}^{N} T_i U_i \\ &+ \left(\frac{1}{N}\sum_{i=1}^{N} T_i^2\right)^{-1} \frac{1}{\sqrt{N}}\sum_{i=1}^{N} T_i(g_o(W_i) - \widehat{g_o(W_i)})\end{aligned} \tag{25}$$

Inspired from the Frisch-Waugh-Lovell Theorem (FWL Theorem) which shows how to decompose a regression of y on a set of variables X into two pieces. This theorem states that, given the linear model $Y = \beta_0 + \beta_1 T + \beta_2 W + U$, the two following approaches for estimating β_1 yield the same result: a). linear regression of Y on T and W. b). three-step procedure: 1) regress T on W; 2) regress Y on W; 3) regress the residuals from 2 on the residuals from 1 for getting β_1 (all regressions using Ordinary Least Squares, OLS). Therefore, back to our example, DML can be done in two stages. Stage 1 includes outcome equation and treatment equation. Outcome equation fits a model to predict Y from X to get the predicted $\widehat{Y}$. Treatment Equation fits a model to predict T from X to get the predicted $\widehat{T}$. Stage 2 performs a regression model on the residuals which could partial out W with a regression model to predict $Y - \widehat{Y}$ on $T - \widehat{T}$. Chernozhukov et al. show that

combining these two algorithms removes regularization bias during the training of the ML algorithms. The pros and cons have been listed in **Table 4**.

Doubly Robust Learning (DRL) is a method for estimating treatment effects when the treatment is categorical. It consists of several variants depending on what type of estimation algorithm is chosen for the final stage, including forestDRLearner, linearDRLearner, sparselinearDRLearner and so on (Buhlmann & Van De Geer, 2011). It simplifies the problem to two regression tasks: 1) predicting the outcome from the treatment and controls, 2) predicting the treatment from the controls. Then the method combines these two predictive models in a final stage estimation to create a model of the heterogeneous treatment effect. It can also be used if our goal is to understand the effect of each of the treatments on the outcome as a function of a set of observable characteristics of the treated samples, also known as the conditional average treatment effect (CATE). This estimator performs automatic featurization and can fit non-linear models.

4.2 Workflow

4.2.1 Key Fundamental Questions to be Answered

This chapter aims to answer the following questions:

- How to discover generalizable and scalable causal signatures of crack propagation by analyzing the multipoint wave-transmission measurements using causal inference approach?

Terminology: Generalizable and scalable refers to discovered causal signatures can be applied to any composition, velocity, density, porosity, and size of material. Physically relevant means discovered signatures are get from the real-world inspired measurements with limited sampling rate and precision.

4.2.2 Description of Workflow

In its broadest and most straightforward sense, signatures are any information that unique, recognizable, and valuable. They come from raw data that can then be translated into knowledge. A good signature allows us to perceive, predict, and react appropriately to changing situations (Smith & Peterson, 2012). The most critical step is characterizing measures, signals, and properties in or of complex systems to detect or attribute change. Difficulties lie in extracting relevant information from a complex environment cluttered with numerous irrelevant phenomena that obscure meaningful signatures or in mining new information from existing data or instrument signals. The objective of this study is to identify the causal signatures of crack propagation by analyzing multipoint wave-transmission measurements from simulation tools (Liu & Misra, 2022). **Figure 4-3** shows the whole workflow which includes two main parts: crack propagation model and causal signature discovery. The crack propagation model collects multipoint wave-transmission measurement data from simulation model.

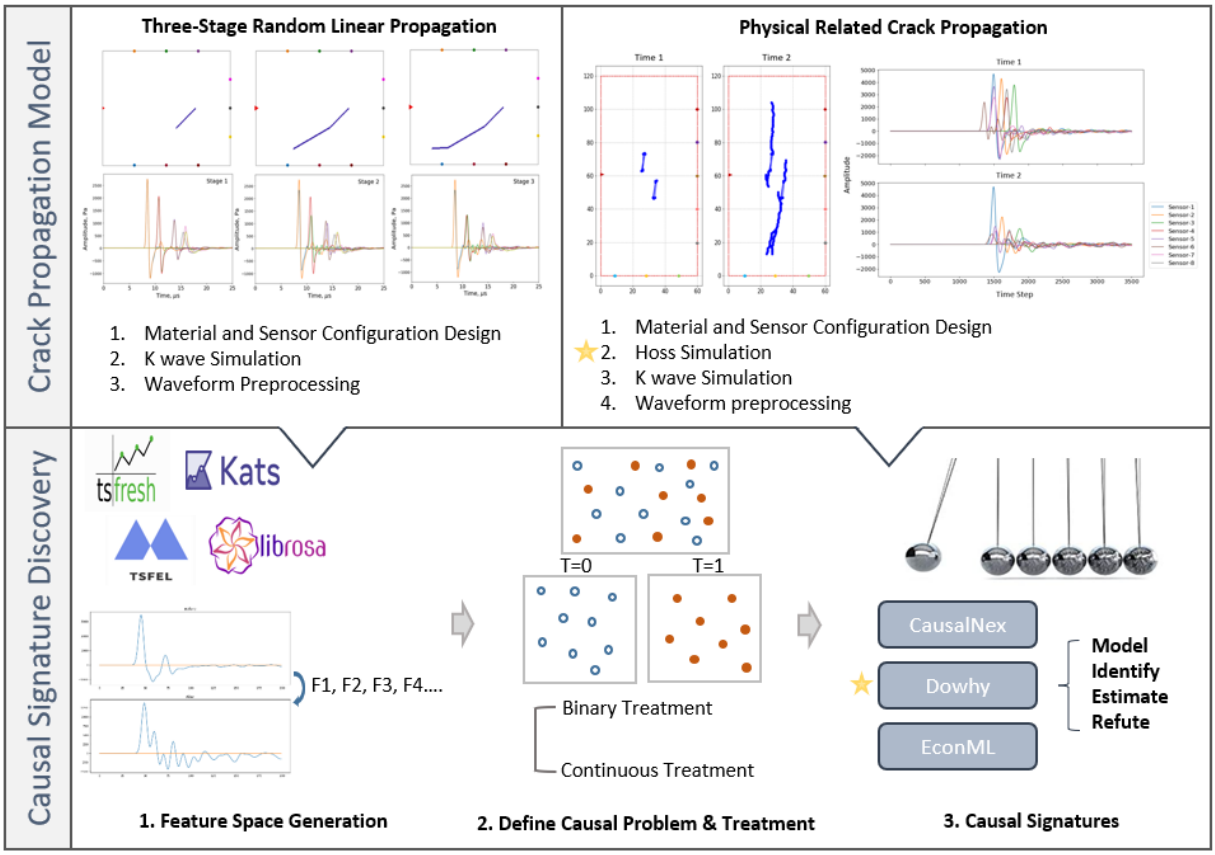

Figure 4-3. Workflow for identifying causal signatures of crack propagation using multipoint wave-transmission measurements. The workflow includes waveform data collection, feature space generation, causal problem definition, validation, and discussion.

This study includes two case studies: random linear crack propagation and crack path from the simulation model. Each crack path is then transferred to the K-wave simulator for elastic wave simulation. Then, causal signature discovery will involve developing large feature spaces, implementing methods to extract causal relationships between variables, identifying key variables that contribute to crack propagation by using causal inference, and testing the generalizability of the identified causal signatures. The workflow provides a structured approach to understanding the underlying mechanisms of crack propagation and can aid in designing systems for fracture propagation identification.

4.3 Causal Signature Discovery for Three-stage Linear Crack Propagation

4.3.1 Causal Signature Discovery with Binary Treatment

Our study aims to identify specific signatures in the recorded multipoint waveforms that have strong causal relationships with crack propagation. For our dataset, samples with crack propagation from stage 1 to stage 3 longer than 8mm are considered the treatment group (T=1). Conversely, other samples with crack extensions shorter than 8mm constitute the control group(T=0). The scaled statistical-parametrization-based features (The features used here are the same with the regression features listed in Appendix A) derived from the corresponding multipoint waveforms constitute the effects for a sample in the control or treatment group. The changes observed in these features between stage 1 and 3 can be attributes to the propagation of the crack. Pre-processing of the data is required to ensure that all the features in the control and treatment groups have the same range. This step ensures that the ATE values, which quantify the causality corresponding to various effects, are comparable between the 20 highest-causality features. Here, we use the DoWhy toolkit to evaluate the causal relationship between the crack propagation and the signatures in the multipoint waveforms. In step one, DoWhy creates an underlying causal graphical model for a given problem, including confounders and instrumental variables with causal hypotheses. **Figure 4-4** lays out the causal graph in our case, where the cause is the crack propagation and effects are statistical parameters change derived from the multipoint waveform measurements. Other variables such as crack location, orientation and background properties are known confounders that influence cause and effect.

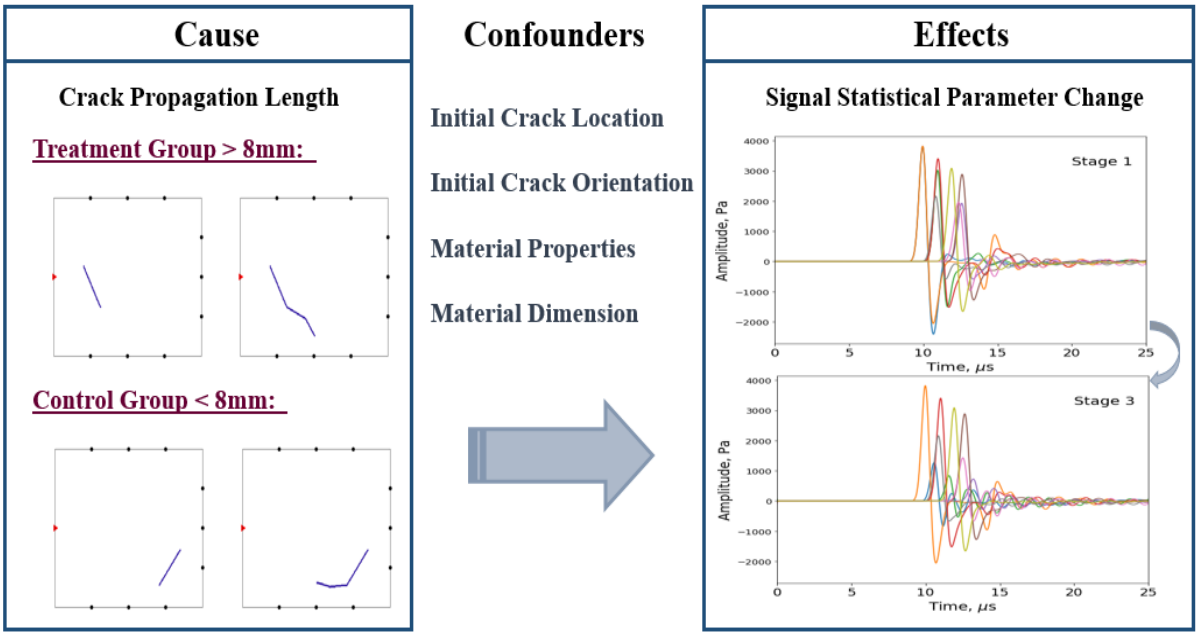

Figure 4-4. Simplified causal graph analysis of our dataset reveals certain confounders that influence the effects of crack propagation on the statistical-parameterization-based features extracted from the multipoint waveforms.

With a given cause and effect, DoWhy automatically considers the rest of the variables as potential confounders. Next, we use supported identification criteria (back-door criterion, front-door criterion, instrumental variables, and mediation) to recognize the causal and effect based on the given model. Identification can be achieved with graph-based criteria and do-calculus without access to the data. Then, we compute the target estimand (ATE/ATT) identified in the previous step with a statistical estimator. To model non-linear data, it also provides machine learning-based methods like gradient boosting tree to learn the relationship between the outcome and confounders, and the treatment and confounders, and then finally compares the residual variation between the outcome and treatment (Sharma & Kiciman, 2019). Finally, the key benefit of using DoWhy is that they offer multiple refutation methods to check the robust of estimate. The common refutation methods could check how sensitive is the causal estimate when replace the true treatment variables with a simulated dataset close to given variables. Or if the effect goes to zero when we replace the

true treatment with an independent random variable. The most important part of this work is illustrating whether instability/changes in our statistical features derived from the multipoint waveform measurements stem from crack propagation. Each statistical feature has 9 corresponding ATE calculated for the 9 waveforms recorded by the 9 sensors placed on the surface of the material. Any feature that fails the refutation test is assigned a value of zero, which means no causation is found. The causal effect can be positive or negative. Positive causation means the change in the effect variable is in the same direction as the change in the cause. By calculating the average of the absolute ATEs for statistical features, it is possible to compare their causal intensity and determine the signatures of crack propagation.

The most obvious observation from the causal analysis is that the number of zero-crossing, negative-turning, and positive turning are the top three features affected by crack propagation. A zero-crossing occurs when the sign of the signal changes. Positive/negative turning is the number of positive/negative turning points for the entire 25-μs waveform. These three signal features are the hallmark signatures in seismic waveforms of crack propagation. This indicates anomalous fluctuations in the seismic waveform signaling crack growth in the material. In addition, significant changes in high-order moments such as variance, skewness and kurtosis are also caused by crack propagation in the material based on the bar plots in Appendix B. It was originally thought that the index of peaks and dips in the waveform, as well as their amplitude, would change dramatically due to the effects of crack growth. However, the observed causal estimate from maximum and minimum index in this study were negligible. Here, we report the impact of crack propagation on the elastic waveform, which does not affect the wave shape or crest but triggers unstable fluctuations near the zero point. In terms of sensors, we notice that the signal from sensor 8, located on the opposite side of the source, was most sensitive to the changes in

fracture length. This is highly consistent with the findings in the feature ranking. One unanticipated finding was that sensor 2 and sensor 1 became the other key spots in the causal study replacing sensor 7 and sensor 9 from feature ranking and correlation ranking.

4.3.2 Causal Signature Discovery with Continuous Treatment

In this study, the cause is crack propagation from stage 1 to stage 3 represented by fracture area fraction (FAF). The biggest difference from the previous section is that the treatment here is of continuous value. As two red lines shown in **Figure 4-5**, samples with FAF change above 0.55 from stage 1 to stage 3 belong to the treatment group. Those with FAF changes less than 0.45 are the control group.

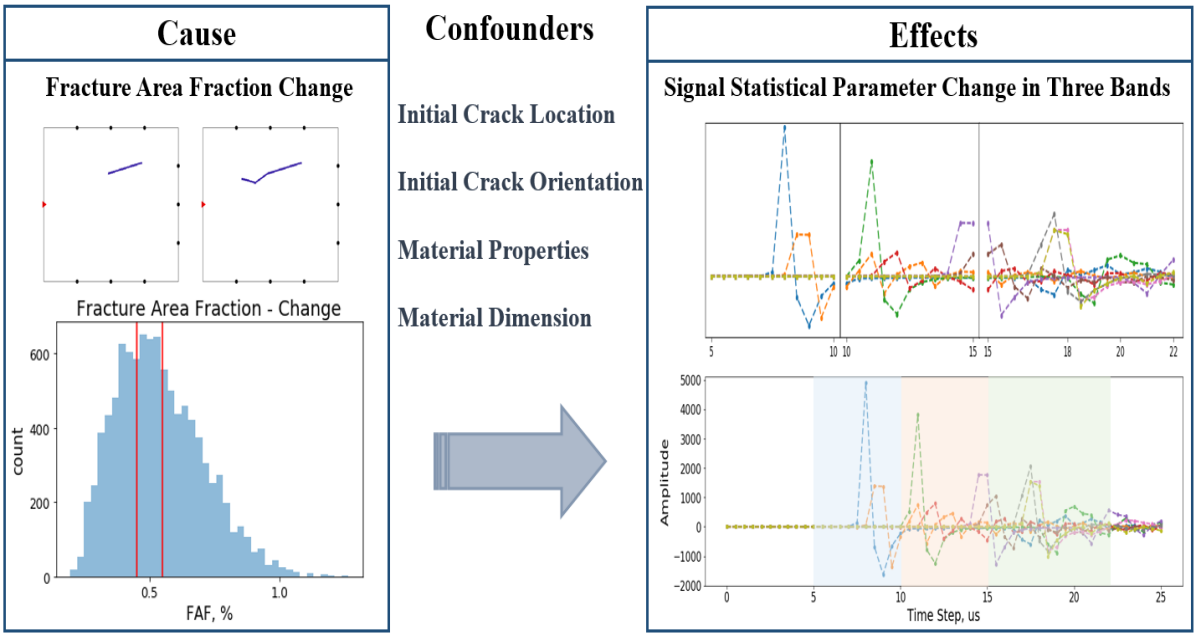

Figure 4-5. Simplified causal graph analysis for continuous treatment that influence the effects of crack propagation on the statistical-parameterization-based features extracted from the multipoint waveforms in three bands.

Our mean goal is to find the true effect of crack propagation in new extended effect space, including time-domain and frequency-domain features in **Table 6**. In the end, the high causality parameters are defined as the signatures of crack propagation. It means that in future when we

notice an abrupt change in that parameter. It indicates that there is a high probability of crack propagation within the material. There are 12-time domain features, including statistical features of the elastic signal from different sensors such as mean, standard deviation, skewness, kurtosis, RMS energy, zero crossing number, the maximum signal index, minimum signal index, peak numbers, positive turning, negative turning, complexity-invariant distance (CID). Features are captured from a python package named Time Series Feature Extraction Library (TSFEL) and librosa. They are open-source libraries designed to support fast exploratory data analysis and feature extraction on signal data. Most of them are straightforward, we will only explain the RMS energy, CID and zero crossing in detail. RMS energy is the root-mean-square value of a signal that relates to the average amplitude of the waveform. CID is a shape-based complexity estimation in time series signal involves the Euclidean distance calculated as (Batista & Keogh, 2011):

$$CID = \sqrt{\sum_{i=1}^{n-1} (x_i - x_{i-1})^2} \tag{26}$$

Table 6. Time-Domain and Frequency-Domain Feature Space for Signature Discovery

16 Extracted Features		
Time Domain		Frequency Domain
1. Mean	8. Min Index	1. Spectral Flatness
2. Standard Deviation	9. Peak Number	2. Spectral Centroid
3. Skewness	10. Positive Turning	3. Spectral Roll-off
4. Kurtosis	11. Negative Turning	4. Spectral Bandwidth
5. RMS Energy	12. CID	
6. Zero Crossing		
7. Max Index		

A more complex time series has more peaks and valleys. Zero crossing computes the number of zero points of the time series signal. It corresponds to the total number of signals that

change from positive to negative or vice versa, as shown in **Figure 4-6**. Zero crossing points are the red dots that fall on the red zero line. Positive turning records the inflection point where the signal value rises, and negative turning shows the point where the signal value falls. They are represented by the green and yellow dots in the figure below. These characteristics reflect the fluctuations of the signal.

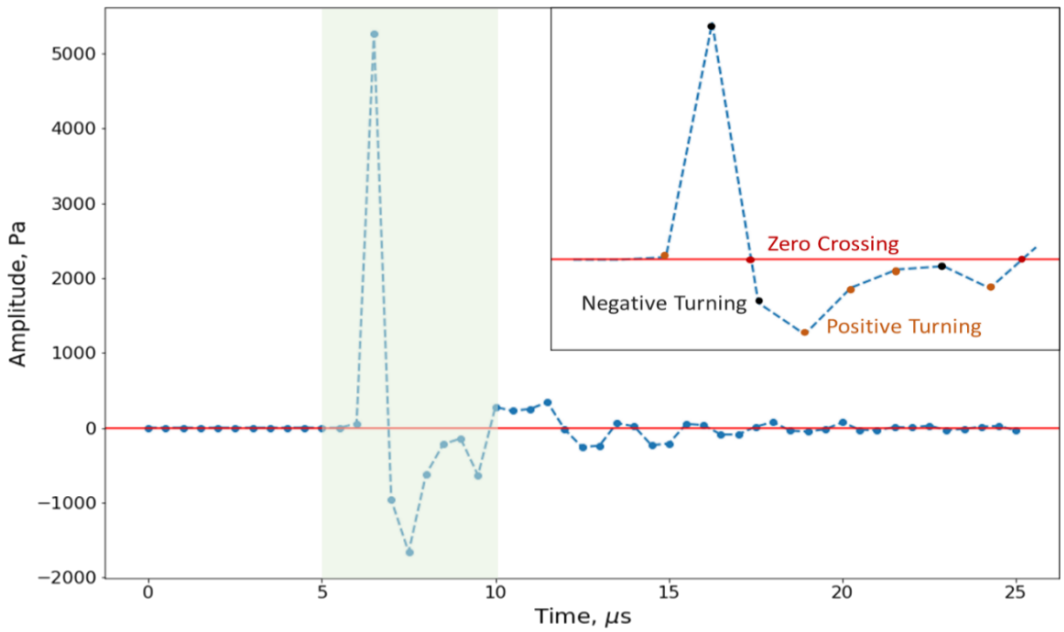

Figure 4-6. Zero crossing, positive turning and negative turning detection. The main figure is a random signal from one sensor. Red line is the zero-points reference line. The upper right part is zoomed-in plot from 5 μs to 10 μs. Zero crossing compute the number of zero point of the signal as marked red dots. The green points are negative turning where signal value decrease. The yellow points are positive turning where signal will rise in the next part.

The short-time Fourier transform (STFT) is a Fourier-related transform that provides the frequency contents over time. It evaluates the Fourier transform in the short time windows used for time-frequency analysis (Durak & Arikan, 2003). Let us discuss, in short, these features generated from the frequency domain.

1. **Spectral Flatness**: Spectral flatness is a metric used in signal processing to quantify how much noise-like the signal is (Dubnov, 2004). A high spectral flatness (closer to 1.0) indicates the

spectrum is similar to white noise. Low spectral flatness (near 0.0) indicates that the spectral power is concentrated in a relatively small frequency band.

2. **Spectral Centroid**: Spectral centroid measures spectral position and shape. It indicates at which frequency the energy of a spectrum is centered upon (Klapuri & Davy, 2007). A high value of spectral centroid implies more signal energy is concentrated in higher frequencies.

3. **Spectral Roll-off**: Spectral roll-off computes the roll-off frequency of a spectrum. It is the frequency below which a specified percentage of the total spectral energy, e.g. 85%, lies in librose.

4. **Spectral Bandwidth**: Spectral bandwidth is defined as the width of the wavelength range (Klapuri & Davy, 2007).

In signal processing, a signal/waveform is viewed as a function of time. Breaking the waveform into several segments helps to detect the effect of crack propagation at different time periods. As **Figure 4-5** shows, the whole waveform per stage could be divided into three bands. The initial band is from $5\mu s$ to $10\mu s$. The intermediate band contains information from $10\mu s$ to $15\mu s$. Then the last band is from $15\mu s$ to $22\mu s$. We remove part of the waiting period at the beginning and part of reflection at the end. For each band, there are 9 corresponding ATE for each feature, which come from the 9 waveforms recorded by 9 sensors placed around the material. The cause is FVF change, while the effect is the features change through propagation from stage1 to stage3. We will search for the most substantial causal effects in each feature space based on ATEs as causal signatures of crack propagation. The detailed ATEs from three bands are displayed as bar plots in Appendix C. The grey line around our estimate is constructed 95% confidence interval calculated by the bootstrap resampling method with 100 simulations. The causal effect could be positive or negative. Positive causation means the effect variable changes in the same direction as the cause. Causal intensity for different features is compared by averaging the ATES from 9

sensors. The determined causal signatures are defined as the FracTag that signifies an early alert for crack propagation.

In band 1, RMS energy, standard deviation, and CID show high causality from sensor 1 to sensor 4 as this part contain more information about the sensors near the source. One unanticipated finding was that the sensor 8, located opposite to the source, have higher causality for shape-based features such as maximum amplitude index, positive turning, negative turning and zero crossing. Compared to band 1, features from band 2 have stronger causality. Positive turning, negative turning and zero crossing rates have strong positive causality. That means as the FVF increase in the material, the frustration of the signal also increases. For band 3, we notice the stronger causality from frequency domain features in the last row compared to the earlier time bands, especially spectral centroid. In summary, in the early time of crack growth, crack propagation has the most significant influence on the maximum index. The median and late time of the propagation need to focus on monitoring the change of positive turning, negative turning, and zero crossing for crack detection.

In terms of sensors, the signal from sensor 8, located on the opposite side of the source, has the highest causality with crack propagation. What is interesting about the ATEs in band 2, sensor results could be divided into two groups, sensors 1 to 4 which are closer to the source are always have the same tend. Then sensor 5 to sensor 9 are relatively far from the source may have different performances from the first group. RMS energy, standard deviation, peak number, CID, and spectral centroid show positive causality for sensors 1 to 4, but negative causality for sensors 5 to 9. Maximum amplitude index causality is exactly the opposite. The maximum index of sensor 1 to

4 reveals a significant negative effect on the variation of FAF, while sensors 5 to 9 have a positive response.

4.4 Causal Signature Discovery for Crack Growth from HOSS Simulation

4.4.1 Introduction

The mechanical behavior and fracture toughness of brittle materials may be affected by the pre-existing cracks and micromechanical behavior of the cracks (Kato & Nishioka, 2005). In a crack propagation process of a brittle material such as pre-cracked rock specimens, usually two types of cracks are observed originating from the tips of pre-existing discontinuities – wing cracks and secondary cracks (Shen et al., 1995; Wong et al., 2001). **Figure 4-7** displays the wing cracks and secondary cracks generally observed in previous investigations with a single pre-existing fracture or two pre-existing parallel fractures loaded in uniaxial compression. Wing cracks usually appear first, which are produced due to tension. In those cases, it is noted that wing cracks initiate at an angle to the pre-existing flaw and tend to propagate in a curved path from the initial flaw tip towards the maximum loading direction (Cao et al., 2015).

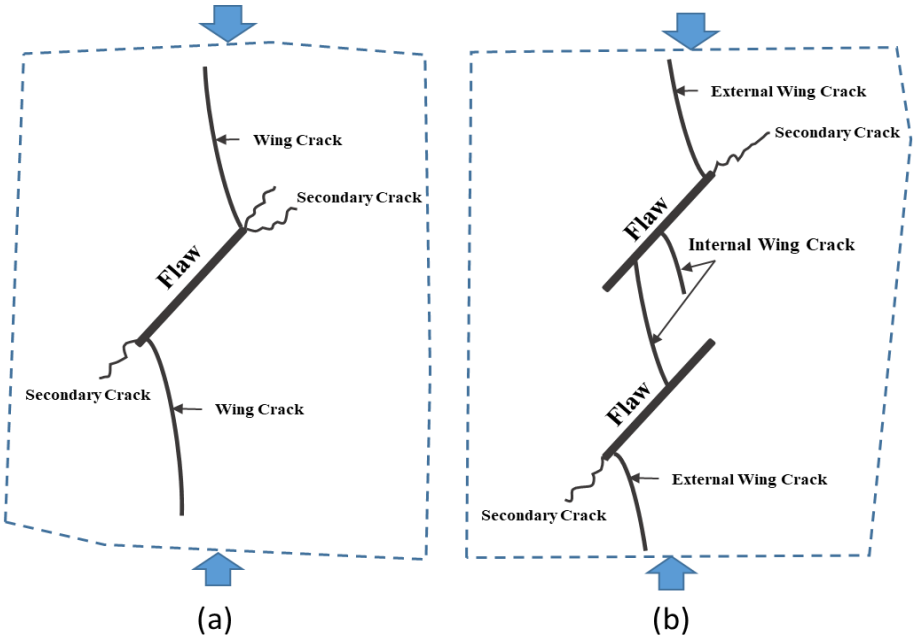

Figure 4-7. Crack types observed in pre-existing cracked material under compression. (a) Single initial crack with wing crack and secondary crack. (b) Two parallel cracks with internal wing crack, external wing crack and secondary crack.

Whereas secondary cracks appear later and are responsible, in most cases, initiated by shear stress. In multiple flaw systems under uniaxial loading, internal wing cracks and secondary cracks also occur and eventually lead to coalescence (Cao et al., 2015). Coalescence may occur in the bridge area due to the propagation of wing cracks emanating from the tips of the pre-existing cracks. The bridge area can be defined as the area in-between the two pre-existing cracks can be investigated in **Figure 4-7 (b)**. Afterwards, if the wing cracks grow to a critical length to the top/bottom of the material, the specimen begins to fail. Many studies have experimentally shown that wing cracks are responsible for crack coalescence and the final crack propagating paths (Haeri et al., 2014).

Compression tests are the natural complement to the tension test, which is used to understand the mechanical behavior and properties of rocks. It has been widely applied to petroleum industries, rock drilling, tunnel design and the design of waste depositories (Isah et al.,

2020). Uniaxial compression test (UCT) is a destructive test developed by the America Society of Testing and Materials (ASTM) and then extended to comprise confined testing and different state of stress and temperatures in the laboratory (ASTM, 1986). During UCT, the specimen is loaded axially to failure, and then stress, the axial and lateral deformation could be recorded with special equipment through an electronic system. The failure load and testing data can be used to calculate the failure stress and determine the elastic constants of the rocks (i.e. Young's modulus, Poisson's ratio). UCT can also be combined with acoustic emission (AE) module to monitor the response of the specimen from the initial to the final failure, which corresponds to the change of stress-strain curve under uniaxial loading (Wu & Huang, 2020). However, the rock mass properties are highly affected by other factors, including pre-existing crack and equipment setup. Then numerical tools are needed to describe material deformation (i.e., fracture and fragmentation, etc.), in-situ stress, and in-situ geologic structures (i.e., faults, joints, etc.) under user-prescribed boundary conditions.

4.4.2 HOSS Simulation Description

The conventional computational approaches generally use continuum-based methods and rely on several assumptions that have limitations when dealing with discontinuous processes, such as fracture and resolution of particle-particle interactions (Bui et al., 2014). At Los Alamos National Laboratory (LANL) researchers developed a hybrid multi-physics software called Hybrid Optimization Software Suite (HOSS). It integrated computational fluid dynamics (CFD), finite-discrete element methodologies (FDEM), finite element analysis (FEA) and discrete element method (DEM) into a single simulation platform with the latest technology to overcome these limitations through a hybrid continuum-discontinued approach. HOSS is designed for solving complex problems in many engineering applications, including oil and gas retrieval and processing, construction, mining, defense and materials development and analysis (Moore et al., 2018;

Schwarzer et al., 2019; Wang et al., 2021). Current application spaces range from hydraulic fracturing to hypervelocity impact (bolides), earthquake rupture, even other more specialized applications such as underground test containment, nuclear weapons effects (cratering, pyroclastic flow, etc.), high explosive performance, and weapons penetration are also considered. Numerous experiments have been devoted to validating the results obtained by HOSS including crack initiation, propagation path, and eventual coalescence of the pre-existing cracks under tensile and compressive loadings (Knight et al., 2020).

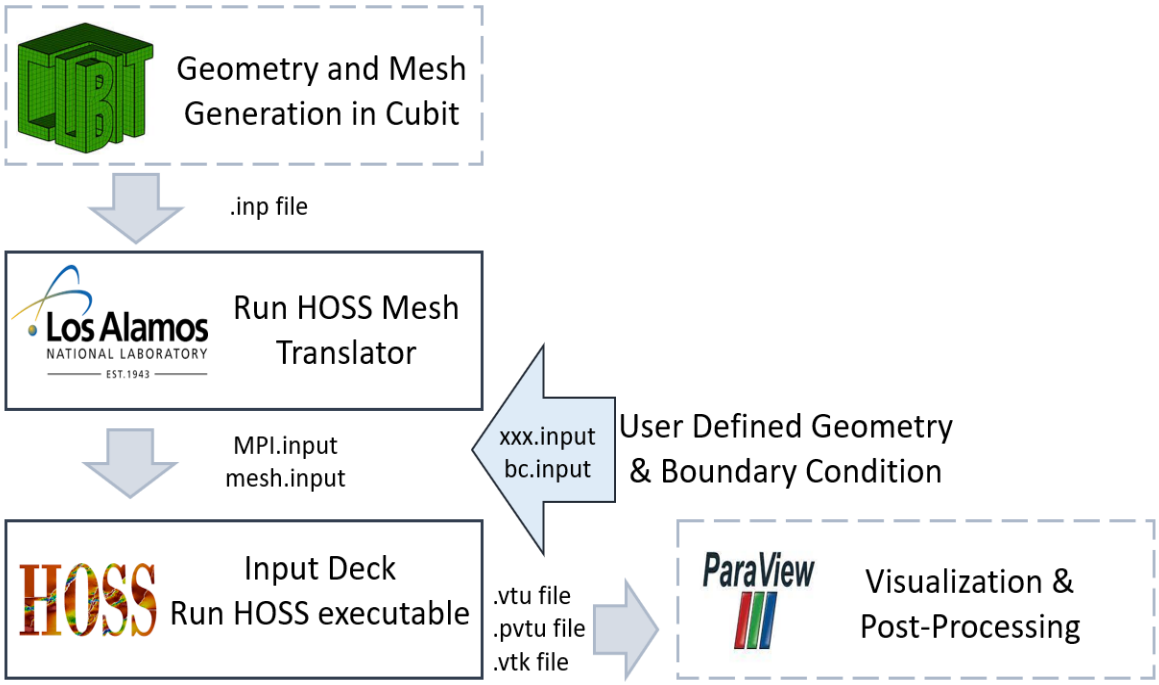

Figure 4-8. General workflow for a HOSS simulation

In the present work, the crack propagation and coalescence process of rock-like specimens under uniaxial compression will be numerically studied in the HOSS platform and K-wave simulation. HOSS is also compatible with other software like Cubit to aid in model generation and post-processing visualization. **Figure 4-8** is the typical workflow for a HOSS simulation. The first step is model geometry and mesh generation which can be complete using any Computer-aided

Design (CAD) meshing tool with Abaqus '.inp' extension. The recommended meshing tool is Cubit created by Sandia National Laboratories. Users creates journal file to define important entities and different material properties to specified regions in geometry model. Next, using the HOSS mesh translator, the '.inp' file can be automatically converted to a format readable by the HOSS executable. The default options always produce two new files 'mesh.inp' and 'MPSDomains.input' for further manipulation. On the other hand, important parameters of simulation including material size, time step, bulk density, Young's Modulus, Poisson's Ratio and boundary conditions are written in the 'xxx.input' and 'bc.input' files. The material constants used in the simulation assume base SI units (i.e., m, kg, s, etc.). The elastic properties are used to calculate the Munjiza constants implemented in HOSS. After preparation of four separate files: 'xxx.input', 'MPIDomains.input', 'xxx.input' and 'bc.input', it is time to run the HOSS executable with established input deck. Finally, the results of the simulation (.pvtu file) can be viewed using multi-platform post-processing software Paraview. All damaged elements throughout the model will be visible.

The problem of interest for this work is the crack propagation and coalescence in 2D pre-cracked samples under pure compression load. HOSS considers two primary modes of failure in 2D: Mode I, which is opening mode due to tensile load, and Mode II, which is sliding crack growth because of shear loading (Hunter et al., 2019). At each time step, the HOSS simulation outputs a 2-way tensor (matrix) representing the position of current cracks and a 3-way tensor representing the entire stress field (Wang et al., 2021). The damage channel denotes the position of the cracks, in which 0 represents undamaged material and 1 represents completely damaged crack. The sample may completely fail at the end and cannot carry any load later.

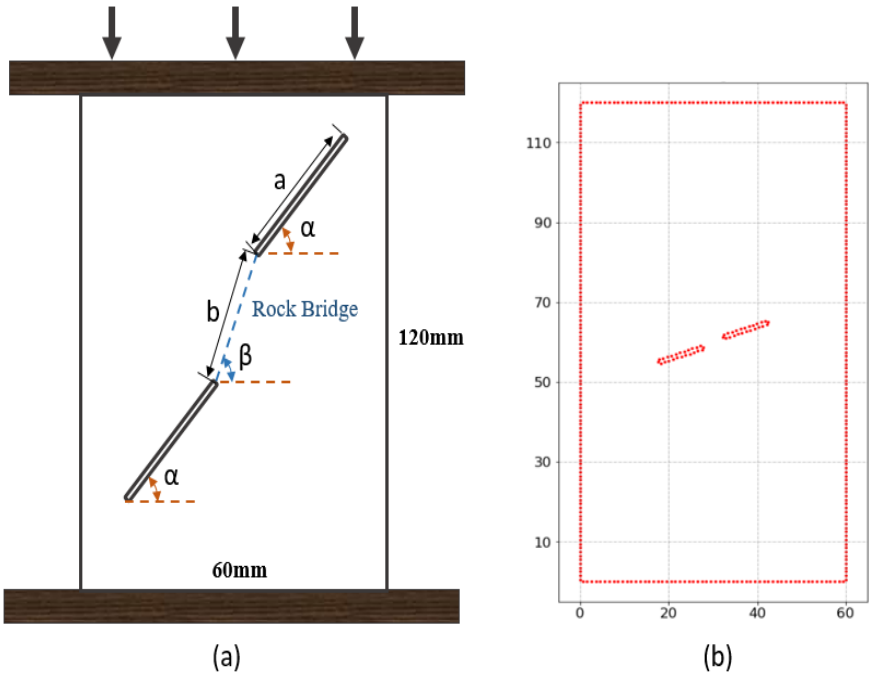

Figure 4-9. HOSS simulation setup for the problem of interest. (a) Schematic view of HOSS simulations which explains the setup of initial parallel cracks. All other geometry, loading, and material parameters were kept the same for all simulations. (b) One simulation sample with $b = 5\text{mm}, \alpha = 10°, \beta = 30°$.

In this study, the material sample is seeded with 2 cracks that mimic initial defects in the material at the beginning of each simulation. **Figure 4-9** presents the initial pre-existing cracks setup in the rectangular 2D material with dimension of 120mm × 60 mm. In the schematic view (**Figure 4-9 (a)**), α is the inclination angle of pre-existing flaw measured from the horizontal plane, β is the inclination angle of the rock bridge and b is the length of the rock bridge. In HOSS simulation, the pre-existing discrete fractures in the rock media can be explicitly modelled and influenced both solid and fluid domains during the testing. To impose this loading condition, the bottom platen of the sample is kept fixed while the top platen is moved with a constant speed of 0.1 m/s. The material is assumed to be elastically isotropic for all cases. The material is assumed to be elastically isotropic in all simulations and the material parameters for the concrete sample are the density of 2650 kg/m^3, Young's modulus of 55 GPa, and Poisson's ratio of 0.15.

Due to the limitation of computational cost, this study only contains 1000 samples running for 35 ms divided into 35-time steps. The initial cracks of each simulation are generated with the different combinations of b, α and β that are randomly selected from a given range. Hence, the crack network evolution will be different for every simulation, yet the overall material response should be nominally the same. **Figure 4-9 (b)** shows the initial setup of a random simulation sample with $b = 5mm, \alpha = 10°, \beta = 30°$. The high-fidelity model from HOSS simulates fracture and fragmentation processes in designed 2D systems, providing accurate fracture growth leading to material failure. However, running such simulations requires large memory available and may be computationally prohibitive.

Figure 4-10 demonstrates the crack propagation and coalescence for two randomly picked samples for five equally spatial time steps. The first sample is generated with the inclination angle other pre-existing flaw $\alpha = 20°$, the inclination angle of the rock bridge $\beta = 90°$ and the length of the rock bridge b is $8mm$. The second row displays the fracture graph for another sample with two relatively further pre-existing flaws. In the last time step, the rock material breaks as a myriad of fragments are created. More crack growth examples with diverse initial cracks setup can be found in Appendix D.

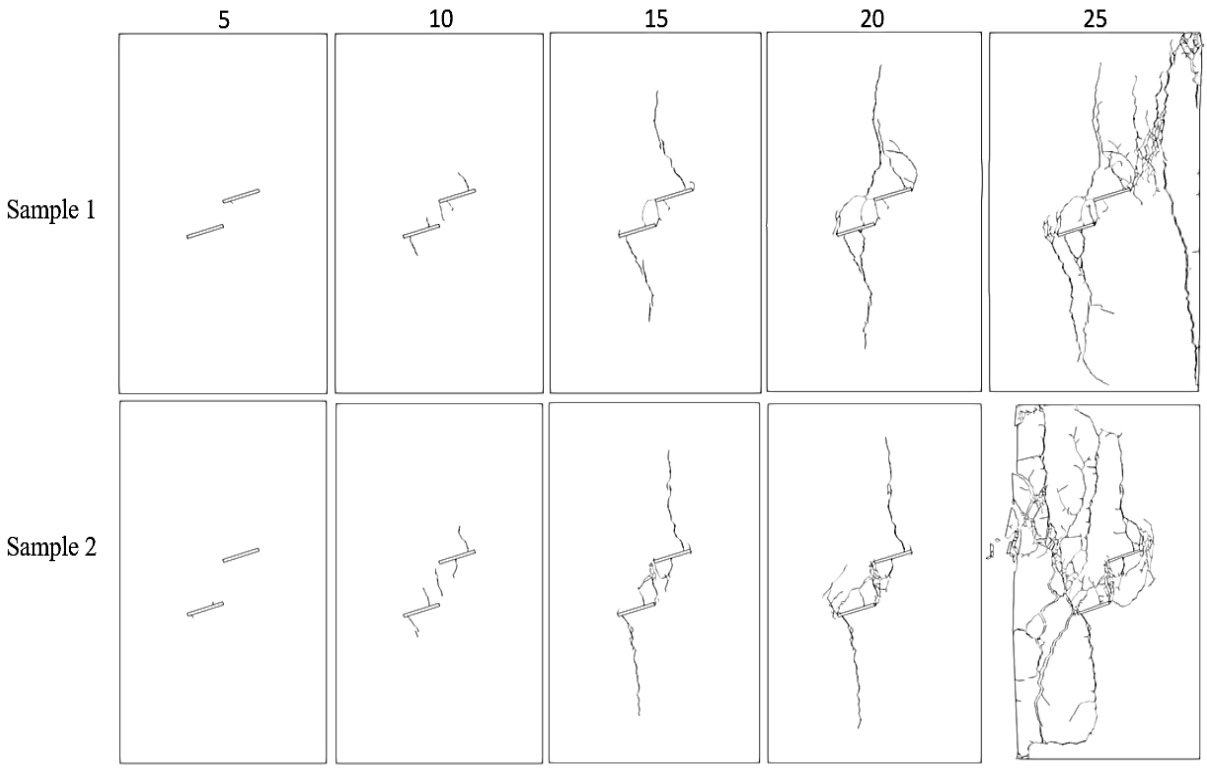

Figure 4-10. HOSS simulation samples of fracture coalescence and propagation with five different time steps. Sample 1 the pre-existing cracks generated with $b = 8mm, \alpha = 20°, \beta = 90°$. Sample 2 the pre-existing cracks generated with $b = 14mm, \alpha = 20°, \beta = 90°$.

4.4.3 Dataset Description and Waveform Generation

As a result, initial cracks inside the laboratory-scale samples propagate and coalesce with hundreds to thousands of incipient microcracks due to the compression loading, which can easily result in terabytes of data. In total, our dataset is around 500 GB and composed of 1060 high-fidelity HOSS simulations, each containing 35 time-steps to simulate the detailed fracture propagation process. To simplify the problem, we narrow our discussion with several critical criteria: 1) first and large crack number increase (>30) in the defined sliding time window; 2) Inside the time window, the crack number cannot be higher than 300. The time window selected is three points with 2-time steps, which is 0.2ms. **Figure 4-11 (a)** gives an example of crack number change in 35-time steps and how the sliding time window works to select the target crack

growth window. It indicates the material has broken after time step 24, and there is no recorded crack number after that point. In this case, the time window selected is 16-18, satisfying all the setting condition. After the criteria filtering with the time window, the sample number was reduced from 1060 to 937. Each sample has one pair of crack graphs illustrating the crack evolution over a time window. **Figure 4-11 (b)** draws the crack points in Python for the start and end points within the selected time window.

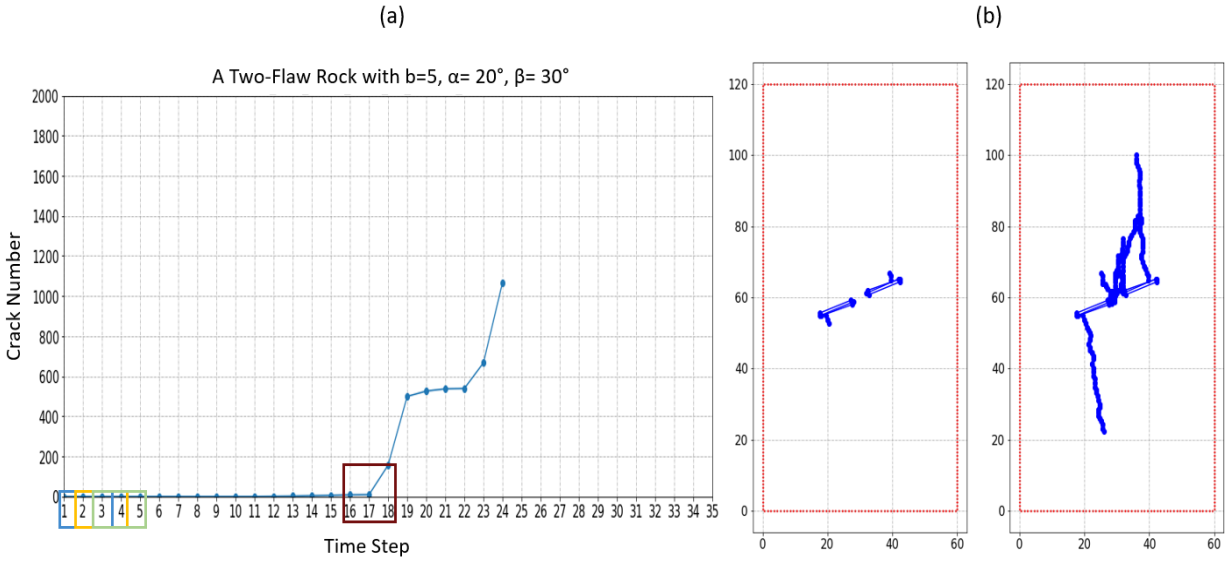

Figure 4-11. Sliding time window to capture the target crack growth with defined criteria: 1) First and large crack number change (>30) 2) Crack number < 300 within the crack window to reduce the complexity.

Figure 4-12 presents four typical types of crack change within the selected time window for different samples. Categories (a) and (c) are similar, including the process for initial crack propagation and coalescence, but coalescence in the rock bridge is not yet accomplished. The apparent difference is their shape. Class (b) is purely crack extension from both sides of initial parallel flaws. Type (c) is crack propagation and completed coalescence. While class (d) focuses on the coalescence between the pre-existing cracks. For these four types, no rule regarding the range of variation in the crack number was figured out. That means the crack number changes are

random and independent of the shape. Failure paths are generally perpendicular to the loading direction, and crack propagation is mainly along the vertical direction.

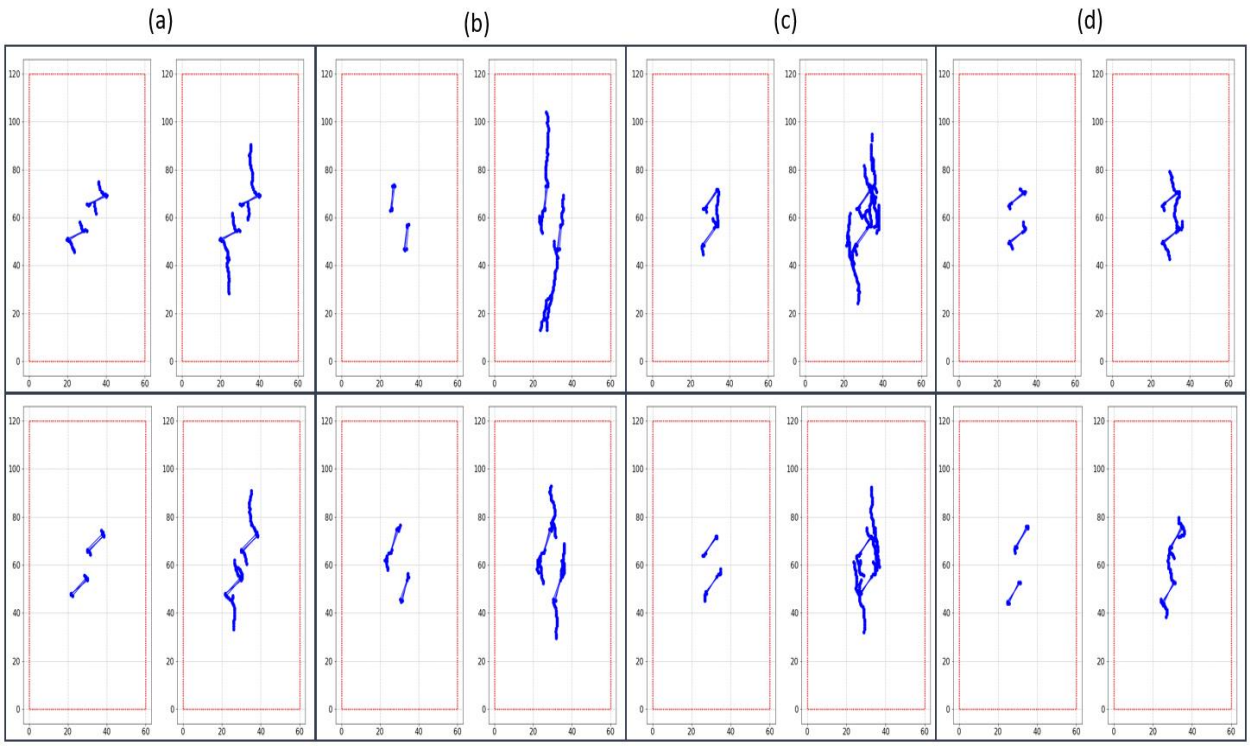

Figure 4-12. Summarized 4 typical types of crack change within the selected time window for different samples. (a). crack propagation and coalescence (not completed); (b) crack propagation; (c) crack propagation and coalescence; (d) crack coalescence.

These are chosen with the goals to validate the causal inference methods, also highlight which causal features stand out and can be used as a generalizable indicator for crack propagation. We found that applying a causal model to discover signatures of crack growth in materials can be done by engineering the features that can be generalized to a wide array of problems. Therefore, we add source and sensor around the material to capture the waveforms that can be used to generate feature space for causal analysis. Similar to Chapter 4, we combine the source and sensor configuration and K-wave simulation to learn the crack information as non-destructive testing. However, the top boundary of the upper platen moves at a speed of 0.1 m/s and is not ideal for

accommodating sensors. In **Figure 4-13**, there is a pressure source placed in the middle of the left side of the material. Then there are 3 sensors at the fixed bottom layer, marked as sensors 1, 2 and 3. To capture sufficient information, the other 5 sensors are placed at the opposite border of the source. It is an assumption that we ignore the position change of these five sensors in the time window of 0.2ms. This actual deformation is around 0.2mm.

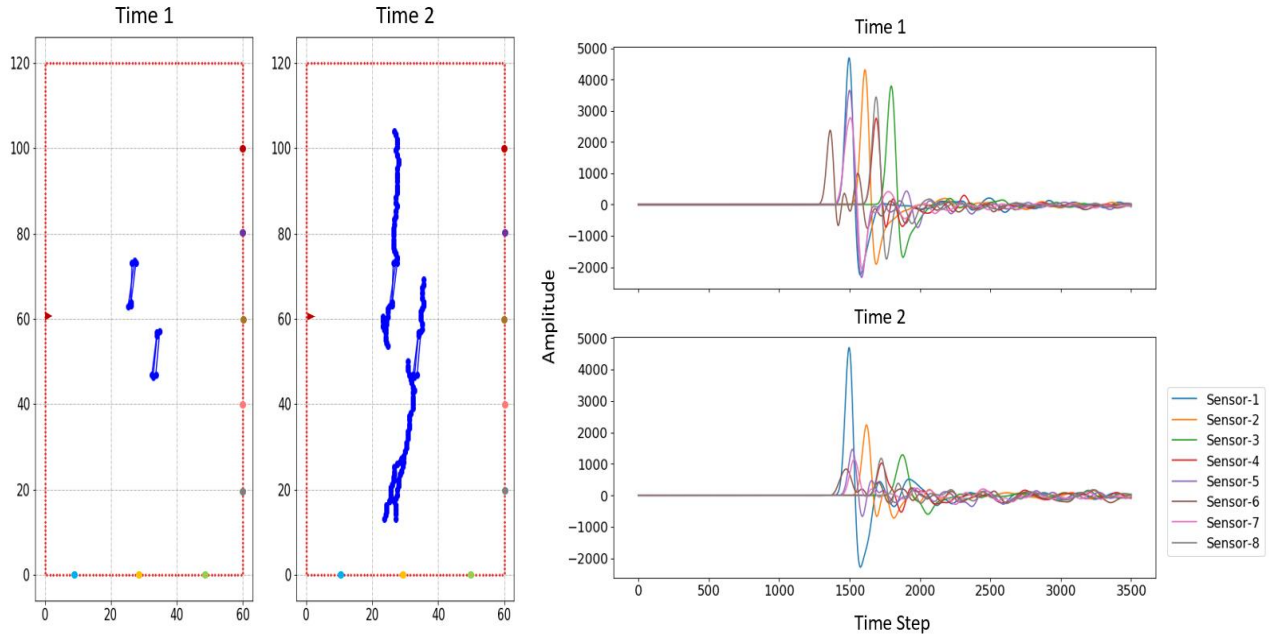

Figure 4-13. Source and sensor configuration and captured waveforms ate the start and end of the time window (0.2ms).

The crack graph and the waveform received at the start of the time window are titled ‘Time 1’. Sensor 6, in brown color, is the first arrival waveform due to its shorter distance, which was postponed in time 2 after the crack graph became complex. The amplitude of sensor 2(orange) and sensor 3(green) are strongly influenced by crack propagation. Therefore, we believe that the parameter changes of the waveforms, such as the peak position and peak amplitude within the time window, can be used as an indicator of crack growth.

4.4.4 Causal Signature Discovery

The purpose of this section is to identify causal signatures from the recorded multipoint waveforms, but the crack propagation and coalescence are more realistic and physically informed instead of random linear extension compared to the previous section 4.3. This section presents a causal inference scheme to discover new signatures from complex fracture systems to detect the fracture changes in the rock. Discovered signatures are generated from a need of understanding the response of waveforms during crack propagation and coalescence, then could further expand as the mission broadened in future including the detection and prediction of fractures. Transforming raw data for useful analysis is a critical step. Time series data is passed as inputs to the extraction method and then quickly transferred into features for further predictive modelling with ease. There are many open-source python packages designed to support the process of fast exploratory data analysis and automated feature extraction on time series sensor data (Naul et al., 2016; Christ et al., 2018; Barandas et al., 2020). Available features in all libraries can be grouped into three categories according to the domain where they are calculated: temporal, statistical and spectral domain. Different existing related packages may be combined to integrate a more thorough analysis.

Table 7. New Time-Domain and Frequency-Domain Feature Space for Signature Discovery

New Extracted Features	
Time Domain	
1. Mean	13. Entropy (Shannon Entropy)
2. Skewness	14. Autocorrelation
3. Kurtosis	15. Nonlinearity
4. Standard Deviation	16. Flat spots
5. Peak Number	17. Peak to peak distance
6. Maximum Index	18. Median crossing points
7. Minimum Index	19. Variation coefficient (std/mean)
8. Zero Crossing	20. Sum of reoccurring points
9. Positive Turning	21. Mean changes
10. Negative Turning	22. Sum of reoccurring values
11. Longest_strike_below_mean	23. Count above mean
12. Longest_strike_above_mean	24. Count below mean
Frequency Domain	
1. Spectral Centroid	4. Spectral Skewness
2. Maximum Frequency	5. Spectral Positive Turning
3. Spectral Kurtosis	6. Spectral Spread

Table 7 is the searching feature space computed from recorded waveforms as the signature candidates consist of 30 features from the time-domain and frequency-domain. The first 10 features from time-domain (red color) are exactly the same as those in section 4.3. In this work, tsfresh, tsfel and librosa are implemented to choose the desired feature space. Thirty features are generated from the signal with different sampling rates of 20MHz, 10MHz, and 5MHz, to ensure the generalizable discovered causal signature.

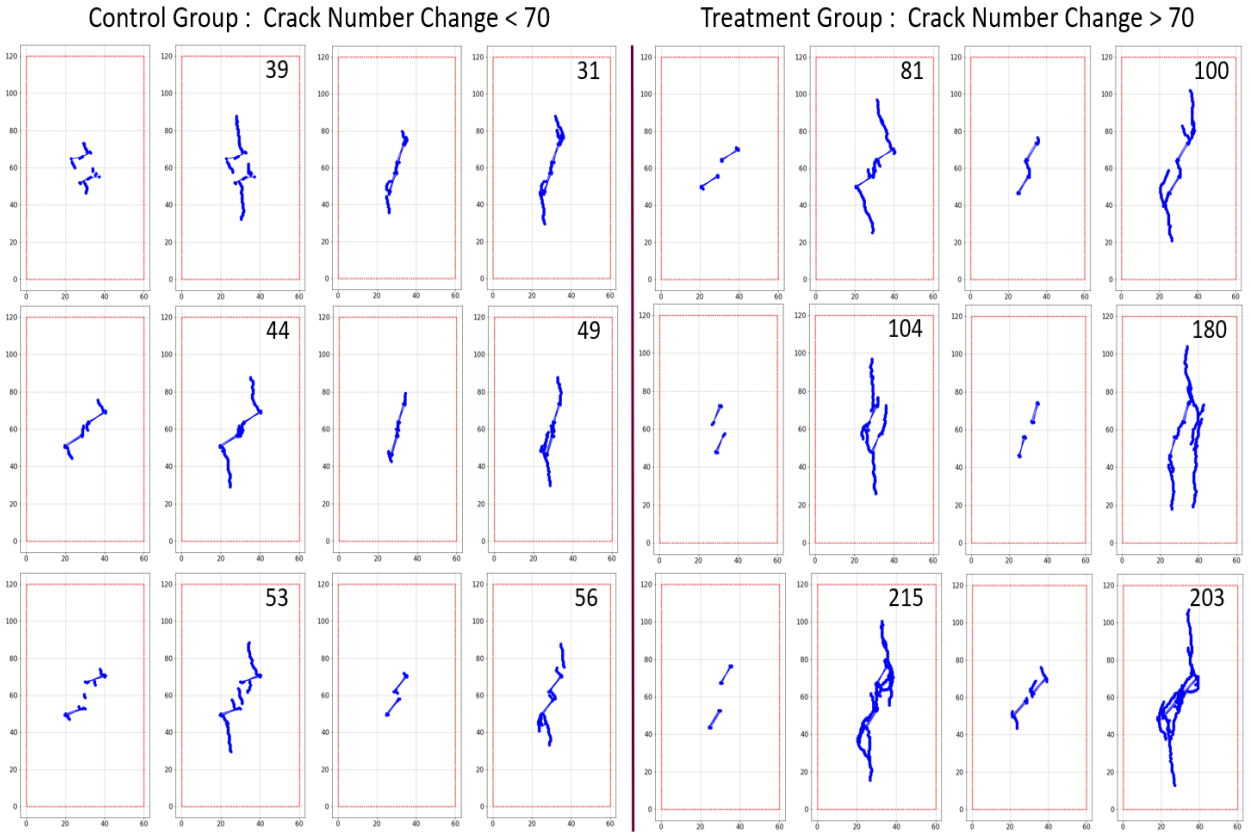

Figure 4-14. Treatment (T = 1) and control (T = 0) group for causal inference. Treatment group has crack number increase higher than 70 grids while control group has crack number change smaller than 70 grids.

In causal inference, binary treatment refers to a treatment that has only two possible values or levels. Conversely, continuous treatment indicates that any treatment value can be taken within a specific range. To conduct binary treatment study, two groups are created: a treatment group (T=1) and a control group (T=0) shown in **Figure 4-14**. The treatment group is the group of individuals or units that receive the intervention being studied. The control group, on the other hand, is a group of individuals or units comparable to the treatment group in all relevant aspects except that they do not receive intervention. The control group serves as a baseline against which the treatment group is compared. In this study, treatment group was defined as having a crack number increase of over 70 grids (408 samples), while the control group was described as having

a change in the number of cracks less than 70 grids (529 samples). By comparing the waveform parameters of different sensors in the treatment group, which experiences crack propagation, to those of the control group, researchers can determine the average treatment effect (ATE) of crack propagation on the waveform parameters.

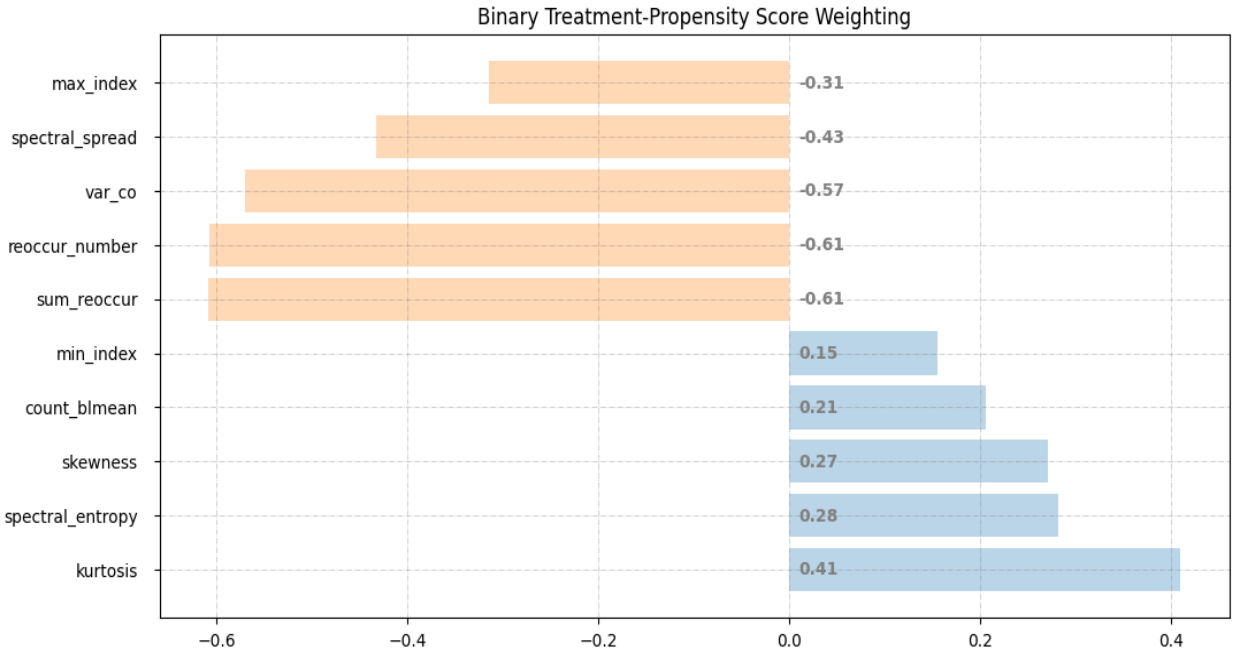

Figure 4-15. The average of eight Average Treatment Effects (ATE) for binary treatment from different sensors at a sampling rate equal to 10 MHz calculated by propensity score weighting.

A positive ATE means that the treatment had a positive effect on the outcome, meaning that the outcome for the treatment group was higher than that of the control group. It's worth noting that ATE only measures the average effect of treatment on the outcome, and there may be individual variation within each group. **Figure 4-15** illustrates the top 5 positive and negative ATE from propensity score analysis for the signal with a 10 MHz sampling rate. ATE for each parameter inside the figure is the average ATE from 8 sensors representing different locations around the specimen.

The top three parameters most influenced by crack propagation are reoccur number, the sum of reoccur values, and variation coefficient of the waveforms. Reoccur number returns the sum of all values that are present in the time series more than once (reoccur_number ([2,2,2,2,1,1,1,4]) = 2×4+3×1 =11). In comparison, the sum of reoccurring values summed up all reoccurring values (sum_reoccur ([2,2,2,2,1,1,1,4]) = 2+1 =3). The variation coefficient is the ratio of the standard deviation to the mean which measures the extent of variability in relation to the mean of the waveforms. When the coefficient of variation is high, it indicates that there is greater variability or dispersion of the data points around the mean value. Spectral spread and kurtosis also exhibit a strong causal relationship with high ATE. In signal processing, spectral spread refers to a measure that characterizes the distribution of frequencies present in a signal's spectrum. It provides information about the extent or dispersion of the frequency components in the signal. A higher spectral spread value suggests that the frequency components of the signal are spread over a wider range, indicating a broader distribution of frequencies. On the other hand, a lower spectral spread value indicates a narrower concentration of frequencies. Kurtosis is a statistical measure that quantifies the shape of a probability distribution. It provides information about the tails and the peakedness or flatness of a distribution compared to the normal distribution. In the context of time series signal, the combination of those parameters describes the degree of variability or fluctuations in the signal over time.

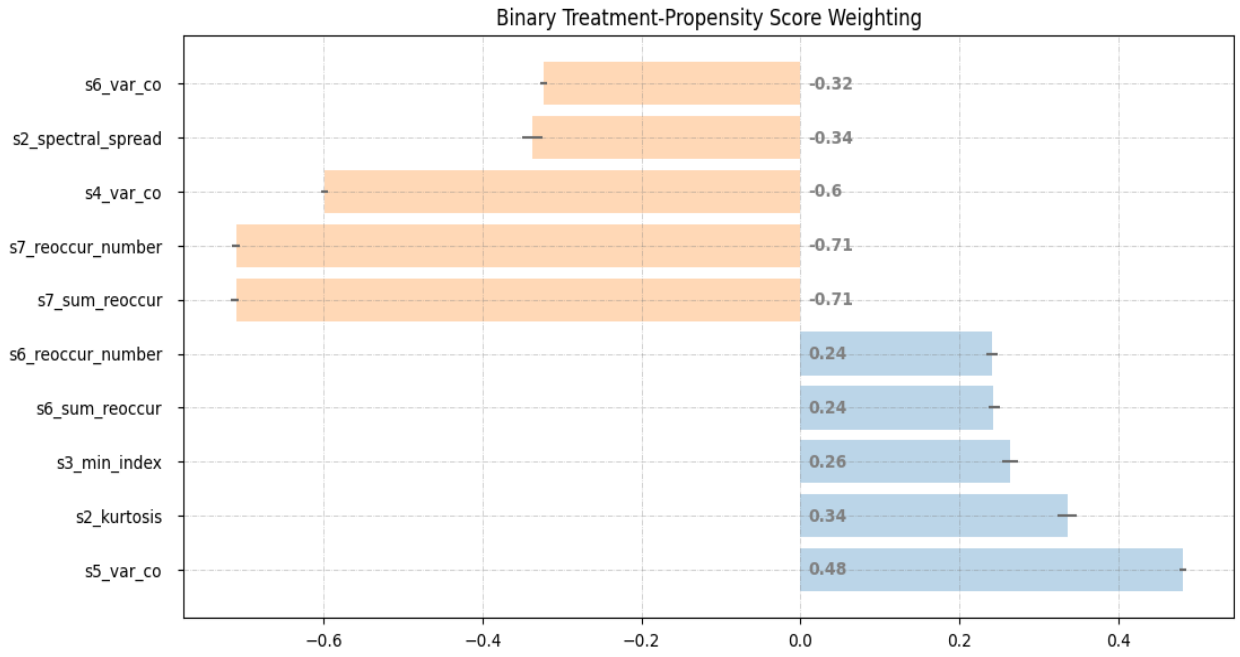

Figure 4-16. Average Treatment Effect (ATE) ranking for binary treatment with a 95% confidence interval using bootstrap sampling. The parameters in orange color are the ranking of the top 5 negative ATE, while blue colors are the top 5 positive ATE parameters.

Instead of focusing on the average ATE of all sensors, **Figure 4-16** demonstrates the overall top parameters for different sensors. In this case, reoccur number, the sum of reoccur values, and the variation coefficient of the waveforms occurs twice in the top 5 positive and negative ranking ATE parameters. Most of them originate from sensors 4, 5, 6, and 7, which are positioned on the boundary opposite to the source. The gray bars are 95% confidence intervals computed from the bootstrap sampling, that provides a range of values within which a population parameter (i.e., mean or median) is likely to fall. Bootstrap sampling is a powerful non-parametric statistical method used to estimate the population parameters without making any assumptions about the underlying population distribution. It is calculated by repeatedly resampling a dataset with replacement to create multiple new datasets of the same size as the original.

Continuous treatment is often used for causal inference because it allows for a more nuanced analysis of the effect of the intervention. In contrast to binary treatment, continuous treatment can vary in intensity or duration. By analyzing the effects of continuous treatment, researchers can gain a better understanding of the propagation-waveform parameters relationship between the treatment and the outcome of interest. In this study, each sample will have a varying amount of crack propagation as the continuous treatment. However, the methods used to estimate the treatment effect may differ depending on whether treatment is binary or continuous. DML is a flexible and robust approach that can handle a wide range of treatment and outcome types, including continuous treatments. Specifically, DML uses two separate machine learning algorithms, one for estimating the treatment assignment and the other for estimating the outcome. These algorithms are then combined to estimate the causal effect of the treatment. Similar to binary treatment outcomes, **Figure 4-17** reveals the number of recurrences, the total sum of recurrence values, and the coefficient of variation of the sensor waveforms are among the top ranking ATE parameters from DML of the waveforms at a 10 MHz sampling rate. The difference with binary treatment is that their causal effect exists in the direction of a positive effect. A positive causal effect is an effect that occurs when an independent variable causes a change in a dependent variable, resulting in a positive outcome. In other words, when crack propagation increase, it leads to an increment in the dependent variables captured from the waveforms.

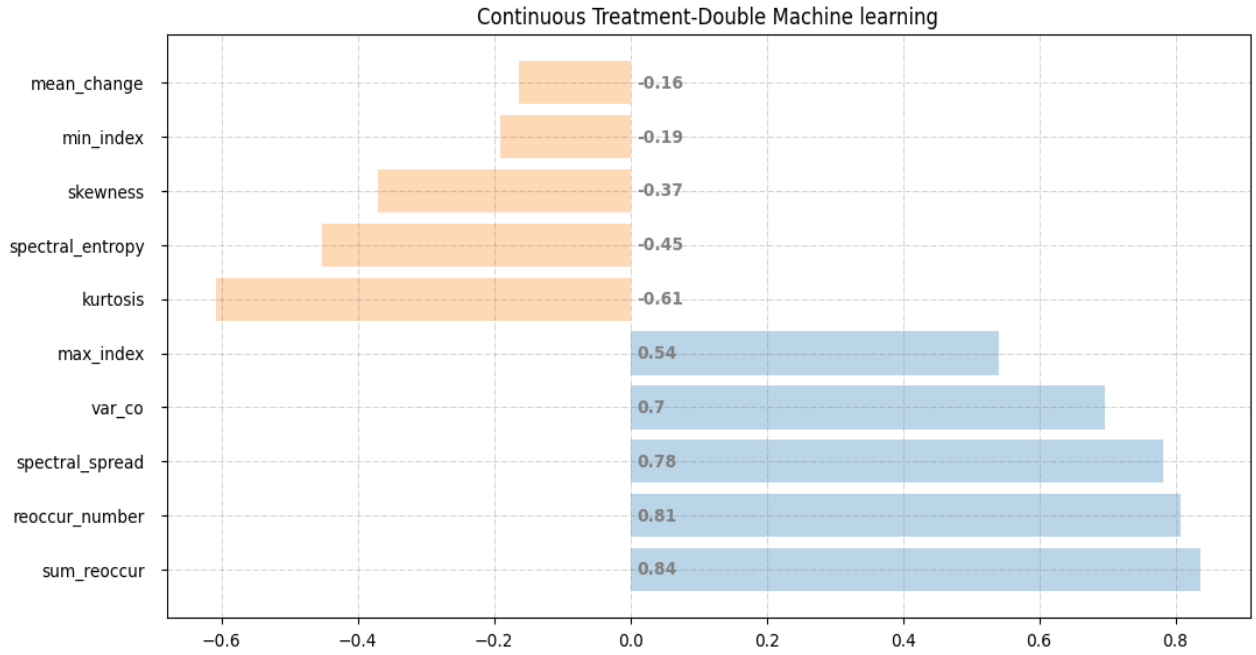

Figure 4-17. The average of eight Average Treatment Effects (ATE) for continuous treatment from different sensors at a sampling rate equal to 10 MHz calculated by double machine learning.

For detailed parameters with sensor information, these three causal signatures are present not only in the top 5 positive ATEs but also in the top 5 negative ATEs as shown in **Figure 4-18**. The wider confidence interval for the continuous treatment indicates that there is a large uncertainty in the true value of the ATE. This may be caused by small sample size, high variability in the data or other factors. It's important to note that a large confidence interval does not necessarily mean that the sample estimate is inaccurate or unreliable. Instead, it reflects the degree of uncertainty in the estimate and highlights the need for caution when interpreting the results.

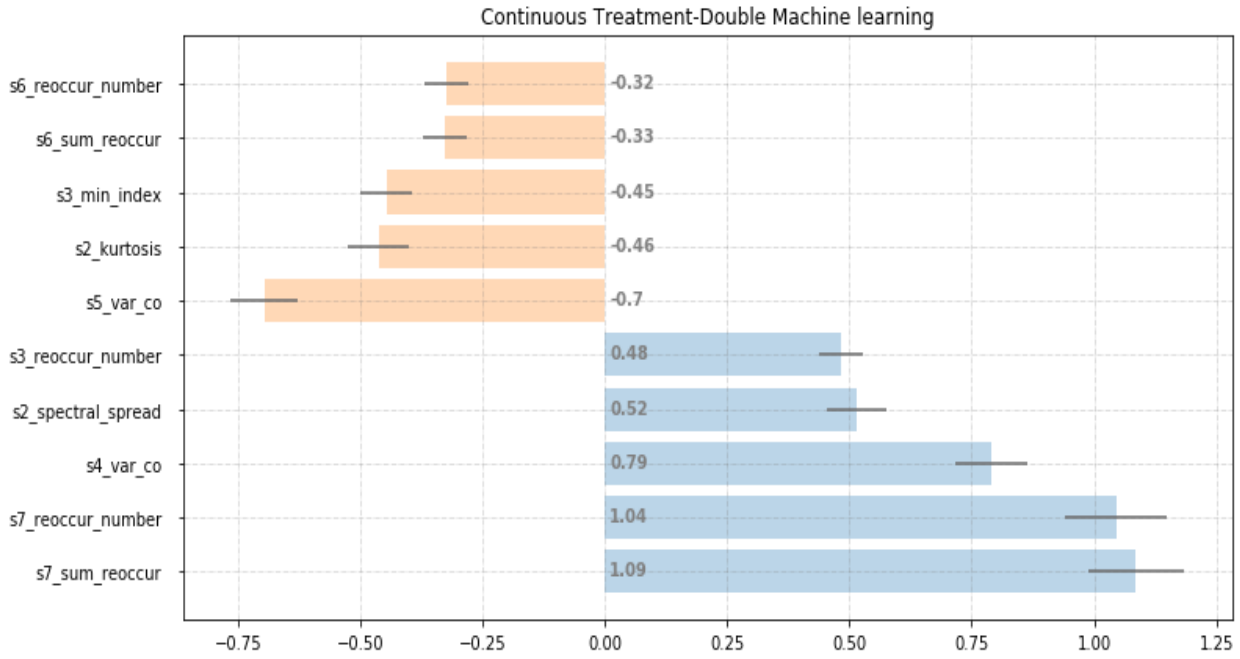

Figure 4-18. Average Treatment Effect (ATE) ranking for continuous treatment with a 95% confidence interval using bootstrap sampling. The parameters in orange color are the ranking of the top 5 negative ATE, while blue colors are the top 5 positive ATE parameters.

4.5 Conclusions and Discussion

This research challenges current data-driven models and starts the evaluation of causal models which integrate domain expertise into machine learning pipelines. The idea is that the latent causal-effect relationship behind the problem we are learning cannot be ignored in machine learning. We present causal network to infer causal structure from elastic waveform data. The generated network defines events as nodes and connects each event with directed arrows. The main motivation here is to illustrate their ability to untangle and explain causal relationships between crack propagation and various statistical features of the designed fracture system. The causal relationship is further tested to ensure that propagation causality signatures are not an artefact of the estimation method. By analyzing the multipoint wave-transmission measurements, we formalize the generalizable, physical-related causal signatures of crack propagation. The causal

signature of crack propagation refers to the waveform parameters which change significantly during the process of crack growth in the material. Here generalizable means the causal signatures can be considered applicable for sensors at different location around the materials with diverse sampling rates. Identified causal signatures can be used to advance scientific knowledge by revealing previously unknown relationships between crack propagation and elastic waveforms. Causal signatures are useful tools for quantifying the variability of the time-series waveforms and can provide important information about the crack propagation inside the sample.

For simulated three stages of linear propagation, fluctuations in the waveform such as positive turning, negative turning and zero crossing are being discovered as the effect of crack propagation. The physical meaning of positive turning, negative turning and zero crossing in time series signal are moments of change in the trend direction and sign, respectively. These features can be used to detect trend reversals and extract useful information about the underlying wave volatility. The greatest weakness in this part is that the crack expansion is totally stochastic and linear, without any solid mechanics and physical modelling. As an improvement, section 4.4 leveraged both causal inference and state-of-the-art simulation solutions to identify the causal signatures of realistic crack propagation, including recurrence values, total sum of recurrence values, and coefficient of variation. These parameters provide valuable insights into the repeating patterns and structures present in time series waveforms and are closely related to the complexity and similarity of each data point.

However, it is important to note that causal signatures are not always definitive, and that more research may be needed to confirm causal relationships and develop effective interventions. Another limitation of identified causal signatures is that they may not fully capture all the underlying dynamics or interactions between variables. Nonetheless, they can provide important

insights into the causal factors that influence outcomes, and help researchers and practitioners develop more effective strategies for understanding crack propagation. It also leads to the emergence of novel research inquiries, hypotheses, and theories.

CHAPTER V

UTILIZING THE KNOWLEDGE-DRIVEN MODEL FOR THE EVALUATION OF MECHANICAL DISCONTINUITIES*

The boom of big data and machine learning has been demonstrated in many fields, which somehow resulted in the vague even erroneous understanding that the huge amount of precious domain knowledge accumulated to date no longer seems to matter. Machine learning and causal inference are two techniques that emerged and developed separately. In this work, we are pioneering to propose the knowledge-driven model to illustrate that domain knowledge, especially causal relation cannot be ignored in machine learning tasks. A knowledge-driven model is a type of model that relies on prior knowledge or expertise to design the model's structure, select appropriate features, and determine algorithms to make accurate predictions. In the following parts, we will show how machine learning can benefit from the tools of causal inference with expert knowledge.

5.1 Introduction

The data-driven model is a type of approach to problem-solving or decision-making that relies heavily on analyzing large sets of data to identify patterns, insights, and predictions. It is often contrasted with more traditional models that rely on intuition, experience, and qualitative analysis. Data-driven model workflow can be customized to specific data/problem which can improve the relevance and effectiveness for better recommendations and decisions. However, data-driven model has its own limitations such as lack of generalizability and explainability. It may face

* Part of this chapter is reprinted with permission from "Monitoring the propagation of mechanical discontinuity using data-driven causal discovery and supervised learning." By Rui Liu, Copyright 2022 Mechanical Systems and Signal Processing, 170, 108791.

problems when the training condition is significantly different with the testing situation. The model we created to map from features to target in one environment may output incorrect values of the target for the features in another environment because the correlations are different. On the other hand, many data-driven models are black boxes, meaning that it is difficult to understand how they make decisions or what features are driving their predictions. This can make it challenging to diagnose problems or understand why the model is making certain predictions.

Knowledge is reflected from data collection to algorithm implementation in data-driven, while the value of domain knowledge in data analysis has been overlooked for a long time. Despite its exploratory nature, this study offers some insight into a knowledge driven model to combine causal inference and machine learning. A knowledge-driven model is a useful tool for capturing and utilizing human expertise and knowledge in decision-making processes, particularly in domains data may be limited or unreliable. Integrating expert knowledge with causal inference into machine learning can significantly reduce data demands, improve the stability and robustness of machine learning, and build interpretable machine learning systems (Deng, 2020). Compared to correlation, causal relationships are invariant, meaning that it is true across different circumstances and environments. From another perspective, causality is an important and growing aspect of interpretability in machine learning. The idea of causality has been developed and studied in many disciplines ranging from philosophy to economics, and even science, to conquer the instability issue in simple machine learning techniques (Hicks, 1980; Shoemaker, 1980; Detto et al., 2012). The intersection of causal inference and machine learning is a rapidly expanding area of research. However, no quantitative evaluation of influences in discontinuity growth has yet been given in rock mechanics.

For these reasons, the main objective of this study was to investigate the causal signatures of crack propagation and their impact on prediction. The causal network quantitatively characterizes the interconnection between crack propagation and the elastic waveform parameters. This could be done using domain knowledge or by using causal discovery algorithms. By using discovered causal signatures, we could incorporate causal knowledge into the model and build an adaptable and robust data system for both linear and physically related crack propagation samples. In future, causality signatures can also be served as early warning systems for the crack propagation in given material, or even field in the future.

5.2 Key Fundamental Questions to be Answered

This chapter aims to answer the following questions:

- Can the signatures discovered using causal inference and traditional feature extraction methods improve the detection, location, and monitoring of fractures propagating in the subsurface earth?
- How to utilize discovered causal signatures of crack propagation by analyzing the multipoint wave-transmission measurements using knowledge-driven model?

5.3 Association, Correlation and Causation

Association, correlation, and causation are three concepts that commonly used in statistics and research. Association refers to the presence of a relationship between two variables, where a change in one variable is related to a change in the other variable. There are several methods to quantify the association between variables. Mutual information calculates the amount of information shared between two variables to detect any kind of dependency, whether linear or non-linear. F-test is another statistical test used to compare the variances of two or more groups. It can

be used indirectly to access the association between two variables through regression analysis. If the F-test is significant, it suggests a strong association between parameters.

Correlation, on the other hand, represents the strength of the linear or monotonic association between the variables as measured by the correlation coefficient. The Pearson correlation coefficient is used to analyze the linear relationship between two continuous variables, while the Spearman correlation coefficient is used to analyze the monotonic relationship between two variables, which may be continuous or ordinal (Cohen et al., 2009; De Winter et al., 2016). However, it is important to note all correlations are associations, but not all associations are correlations.

Causation describes the relationship between two variables in which one of them is the cause of a change in the other variable. To establish causality, it is necessary to demonstrate that changes in one variable directly causes a change in another variable and that relationship is not due to other factors or variables (Confounder). Additionally, causation involves understanding the underlying mechanisms and processes that contribute to a particular outcome.

Scikit-Learn is a comprehensive machine learning library in Python that provides a variety of feature selection methods, including mutual information, F-test, and correlation coefficients. They are popular methods to identify the most relevant association or correlation features and improve the accuracy and efficiency of prediction applications. However, none of prevailing machine learning library or tool could provide causality-based feature selection. This section aims to clarify the distinctions between these concepts, which are often confused or misused in practice. Furthermore, this section emphasizes the significance of establishing causality in research, an aspect that has often been disregarded in various studies.

Correlation and causality can be deceptively similar and can simultaneously exist. However, correlation is not the same as causation (Duesberg, 1989; Conn, 2017). It is easier to find correlations compared to proving causality. Correlations can be easily quantified in terms of statistical or mathematical formulations that is applied on the data. As compared to correlation, a quantification of causality allows us to make better predictions about the future, explain the past, and intervene to change the outcomes. A correlation between x and y measures association and can be interchanged between the two. When x is correlated to y, y is automatically correlated to x. On the contrary, when “x causes y”, we cannot say that “y causes x”.

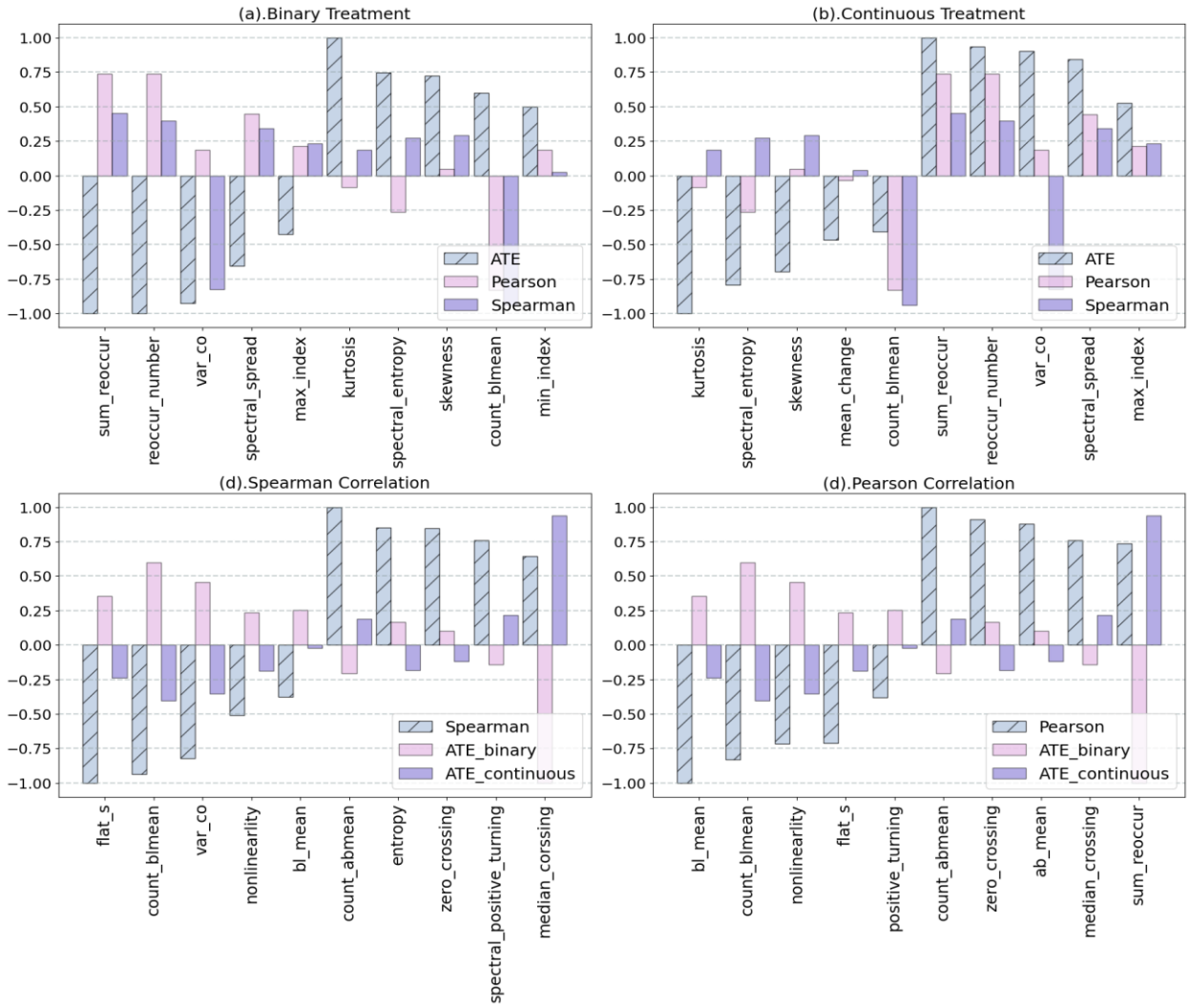

Figure 5-1. Exploring the Causation-Correlation Relationship: Evidence from (a) and (b) demonstrating causation does not imply correlation, while (c) and (d) show Pearson and Spearman correlation do not imply causation either.

Figure 5-1 illustrates a comparison between the causal signatures of simulated crack propagation using HOSS and the correlation coefficients captured through Pearson and Spearman correlation. The Pearson correlation measures the strength and direction of the linear relationship between continuous variables, while the Spearman correlation assesses the monotonic relationship between variables without assuming a specific functional form and can handle ordinal or interval scale variables. The choice between the two depends on the nature of the variables and the research

question at hand. The values presented here have been normalized to the range of (-1, 1) for the purpose of facilitating comparison.

The baseline for comparing their correlation coefficients in **Figure 5-1**(a) and (b) is the top five positive and negative causal variables from binary and continuous treatment. It shows causation does not imply any correlation. But there is also another possibility that the sample size is small, leading to insufficient statistical power to detect a correlation. In this case, it is necessary to increase the sample size to increase the likelihood of finding a correlation. In contrast, **Figure 5-1**(c) and (d) use high Pearson correlation and high Spearman correlation parameters as the base variables to demonstrate correlation and do not imply any causation. This suggests that the presence of a correlation between two variables does not necessarily mean that one variable causes the other.

Similarly, **Figure 5-2** compares the causal signatures of simulated crack propagation using HOSS and the association calculated from F-test and Mutual information. The values presented have been normalized to the range of (0, 1) due to non-negative association metrics. The subplots (a) and (b) indicate that the top five highly causal features exhibit a strong association (>0.5) as revealed by either the F-test or mutual information analysis.

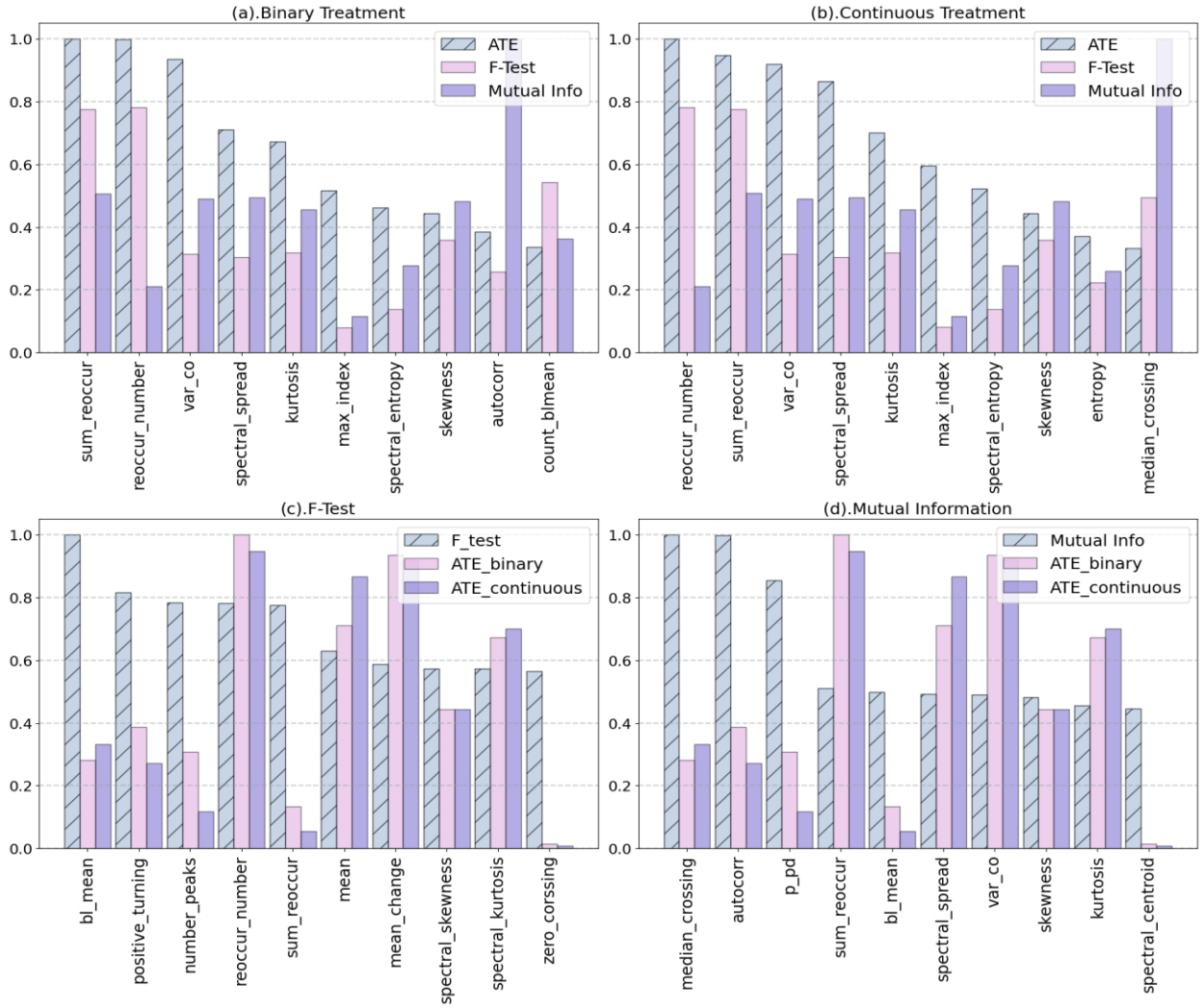

Figure 5-2. Exploring the Causation-Association Relationship. Evidence from (a) and (b) demonstrating that causation implies association, wherein strong causation leads to high association. In contrast, (c) and (d) show that F-test and mutual information do not necessarily imply causation.

Causation implies association because a causal relationship between two variables requires that there be an association or correlation between them. In other words, if one variable causes a change in the other variable, then the two variables must be related in some way. However, it is important to note that association does not necessarily imply causation because two variables are associated does not mean that one causes the other shown from (c) and (d). Therefore, it is important to be cautious when interpreting association/correlation and to avoid making causal

inferences based solely on association/correlation. Additional research and analysis, including experimental or quasi-experimental designs, are necessary to establish causality between two variables.

5.4 Knowledge-driven Model for Three-stage Linear Crack Propagation

In this work, we propose the use of a knowledge-driven causal-inference model to visualize three-stage linear crack propagation by analyzing causal signatures searched from more than 500 time/frequency domain features across 10,000 samples. Incorporating causal inference into a knowledge-driven model as pre-processing step could help to improve the accuracy of the mode, by ensuring that the ultimate decision-making or forecasting is based on valid causal relationships between variables.

Figure 5-3 compares the difference between data driven and knowledge driven model steps in this work. A data driven model can be decomposed into different steps, including data collection, feature engineering, data preprocessing, modeling, and predicting. On the other hand, knowledge driven model is start with a causal statement to define the treatment, effect and the potential confounders. Domain knowledge plays a significant role in causal hypothesis generation. The causal graph is a directed acyclic graph (DAG) of causal-effect relationships between variables. Constructing a useful causal model requires not only domain knowledge but also causal inference. In our study, causal inference could be treated as a tool to discover the FracMarker, which is causal signatures of crack propagation. FracMarkers are used to bridge machine learning and causal inference as new features for machine learning.

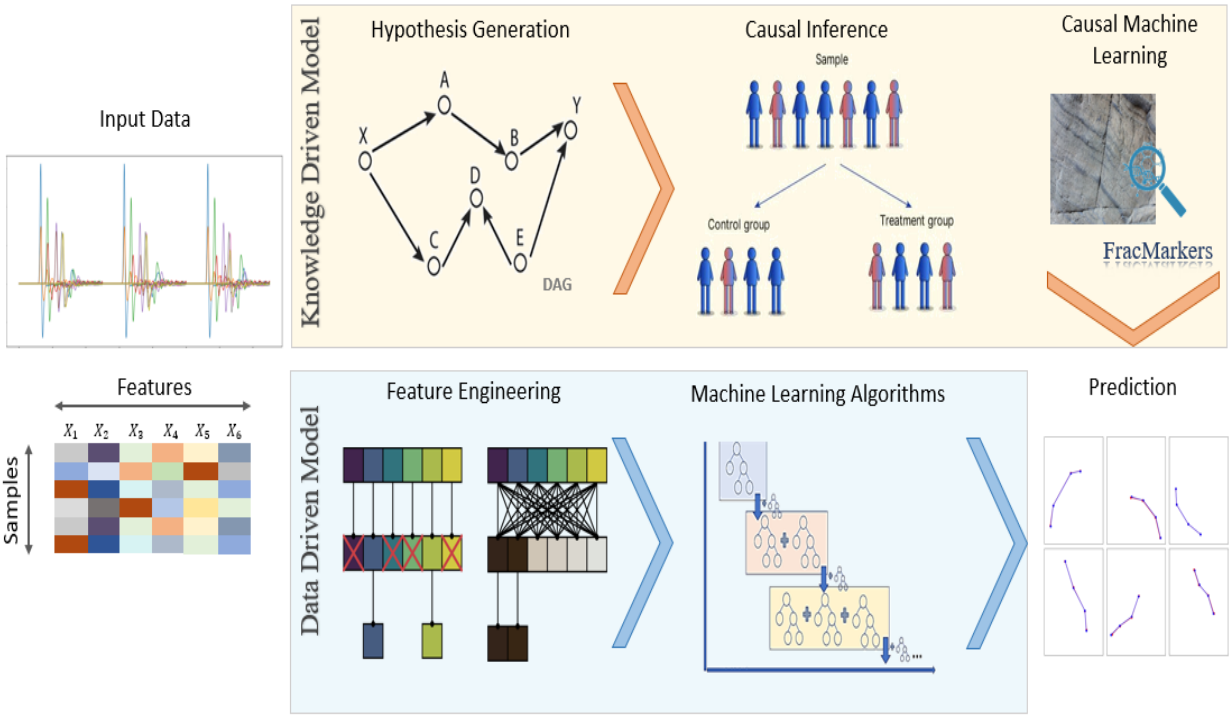

Figure 5-3. The comparison of data driven model and knowledge driven model. Two model usually share the same input data, which is the waveform in our case. Data driven model includes data collection, feature extraction, data preprocessing, modeling and crack prediction. Knowledge driven model contains causal graph, causal inference, a followed causal machine learning and final prediction.

In data driven model setting, we are focus on the useful features for prediction. As such, we tend to select features based on the prediction performance. Machine learning should not only make decisions but also provide a means of how predictions were made. In contrast, causal inference is constructing features based on the domain knowledge and statistical relations. Causal inference is a tool to break the black boxes in machine learning. Future studies on the causal inference are therefore recommended. When a machine learning algorithm relies heavily on correlations for prediction, its performance maybe poor on new data in different environment. Correlational pattern machine learning is insufficient for robust and reliable prediction. To be confident of our predictions and gap-fill the scenario difference between training and test, the invariant causal relationship is needed. This section displays causal insights could improve pure

correlation predictions. The box plot for all features, causal features and correlation features prediction results can be compared in **Figure 5-4(a)**. Box plots visually show the distribution of error from testing set with five important lines, the minimum, first quartile, median, third quantile, and the maximum. The two lines outside the box are 1.5 times the interquartile range (IQR). Outliers fall on the upper side as individual points.

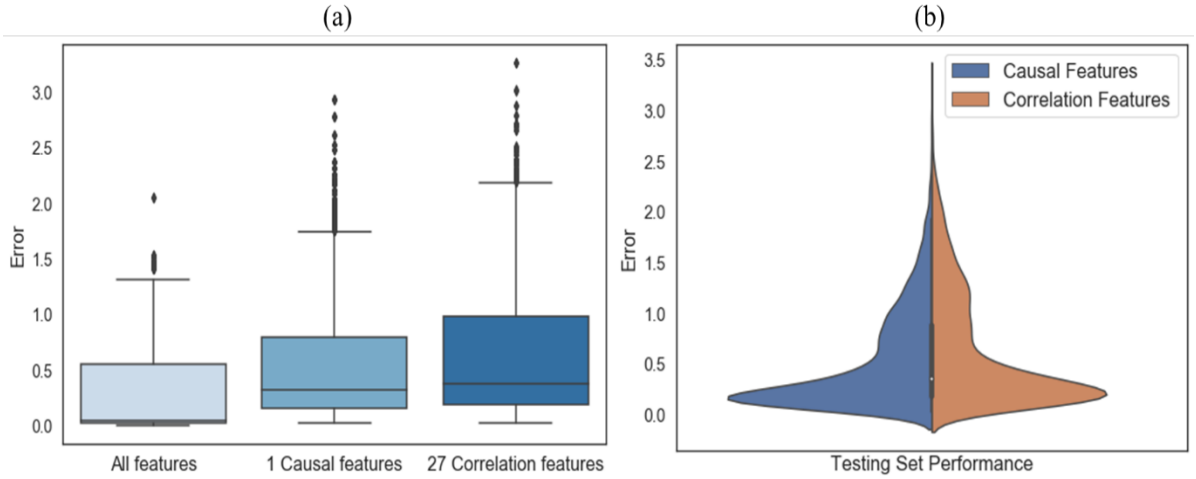

Figure 5-4. Summary of prediction error from all features, causal features, and correlation features. (a). Box plots compare the prediction performance from all features, causal features, and correlation features. (b). Split violin plot further compares the error distribution of causal features and correlation features.

In **Figure 5-4(a)**, the left box is the prediction result with all features extracted from 9 waveforms which perform best (20features*9sensors*3stages). The middle box is the prediction result with our strongest causal signature, zero crossing from 9 waveforms in three stages (1feature*9sensors*3stages). Then 27 high correlation features from mutual information ranking are used to generate the right box plot. It is apparent that all features could get the best prediction due to the large feature set. A split violin plot, as shown in **Figure 5-4(b)** is used as a handy tool in data visualization to compare the error distribution from causal features and correlation features. Comparatively speaking, causal features provide better prediction with lower computational costs.

5.5 Knowledge-driven Model for HOSS Crack Propagation Simulation

HOSS software from the LANL used advanced numerical methods to simulate fluid flow and geomechanical properties, which is critical for accurately predicting the fracture propagation process. By simulating these complex physics, HOSS can provide valuable insights into the behavior of fractures and how they interact with the surrounding rock. HOSS has been extensively tested and validated against laboratory experiments, field data, and other simulation tools. This testing has demonstrated that HOSS can accurately predict crack growth and other key parameters. By incorporating information into the HOSS simulation, we could improve the accuracy of the fracture propagation with complex patterns with the rock-like specimens. The combination of HOSS and knowledge-driven model has the potential to quantitate the fracture propagation process and optimize stimulation design for improved production and efficiency.

The feature selection methods used in data-driven models with scikit-learn are largely based on statistical tests such as mutual information, F-test, and correlation coefficient to identify associated or correlated features. In addition, researchers may use feature importance methods to determine the relative importance of each feature in making predictions. The most frequently used approach is permutation importance, which involves randomly shuffling the values of each feature and measuring the resulting decrease in model performance. Features that result in a greater decrease in performance are considered to be more important. In contrast, knowledge-driven models focus on using domain knowledge and prior information to identify the causal features that are likely to have a causal influence on the outcome variable. Causal features provide a more

accurate and interpretable representation of the underlying causal relationships, which can be critical for making informed decisions and interventions in complex systems.

In this section, we predict the crack propagation number in the given time window with all features, association features, correlation features and causation features to compare the performance from data-driven and knowledge-driven models. In the training process, the dataset has been split into training and validation sets, and setting the random seed ensures that the same samples are selected for each run. The 10 box plots in **Figure 5-5(a)** consist of 10 box plots that show the mean absolute error (MAE) of a prediction model in millimeters, with each plot corresponding to a different random seed on the testing set. The feature sets in the plot include all features, top 3 causal features and 3 top-ranking features from eight sensors using the scikit-learn feature selection methods such as F-test and mutual information.

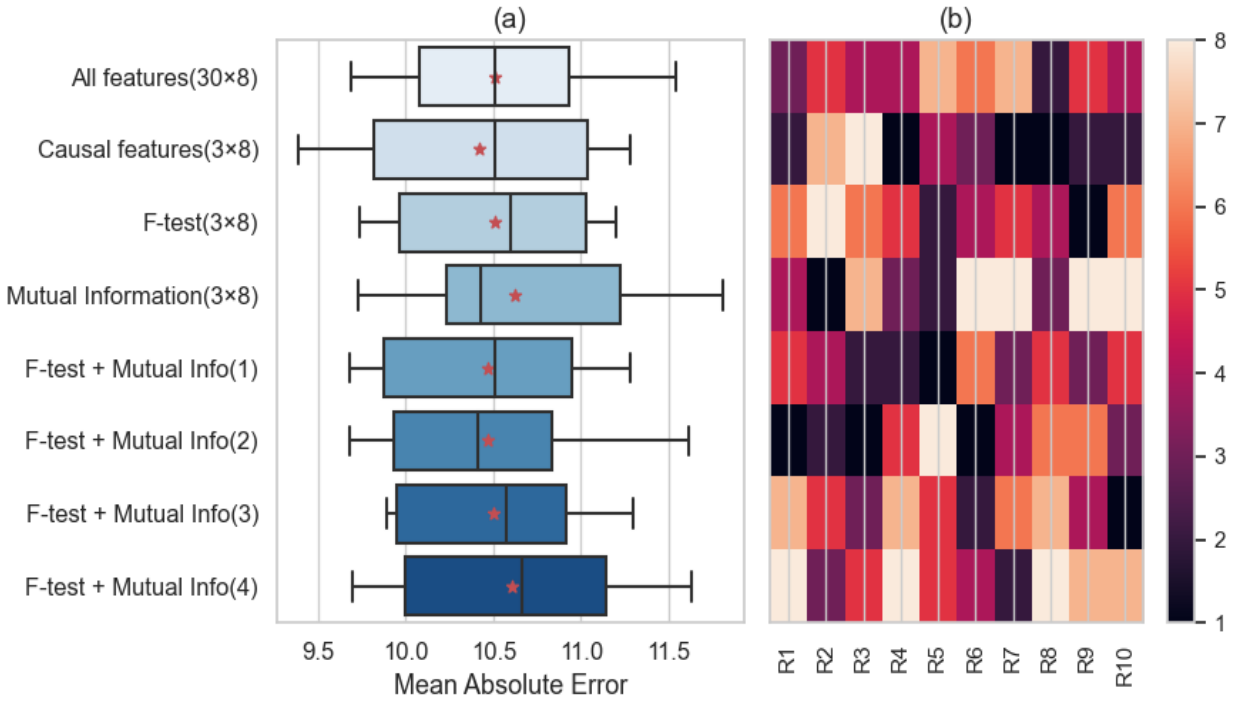

Figure 5-5. The performance of a model was evaluated using all available features, three causal features, and three features selected through methods such as F-test and mutual information. Box

plots in (a) illustrate the distribution of mean absolute error (MAE) for each feature set. In (b), a colormap displays the ranking of the results from 10 different train-test splits.

In a box plot, a rectangular box is drawn with the bottom and top of the box representing the first and third quartiles (Q1 and Q3), respectively. The median value is marked by a line inside the box. The red stars inside are the mean points. All results were obtained using a random forest algorithm that underwent grid search and hyperparameter tuning to prevent overfitting. Nevertheless, due to the limited sample size in our case, the model's performance in predicting changes in crack propagation length is not satisfactory. **Figure 5-5(b)** presents a colormap that illustrates the ranking of eight different models based on ten train-test splits. Based on the observations, the quality of the feature used to train the model can greatly affect the prediction performance. Certain feature sets may lead to challenges in interpreting the results of the model, as well as lower generalization performance. In addition, although causal features may not always yield the best results, they tend to perform comparatively better on the distribution of box plots compared to other feature sets.

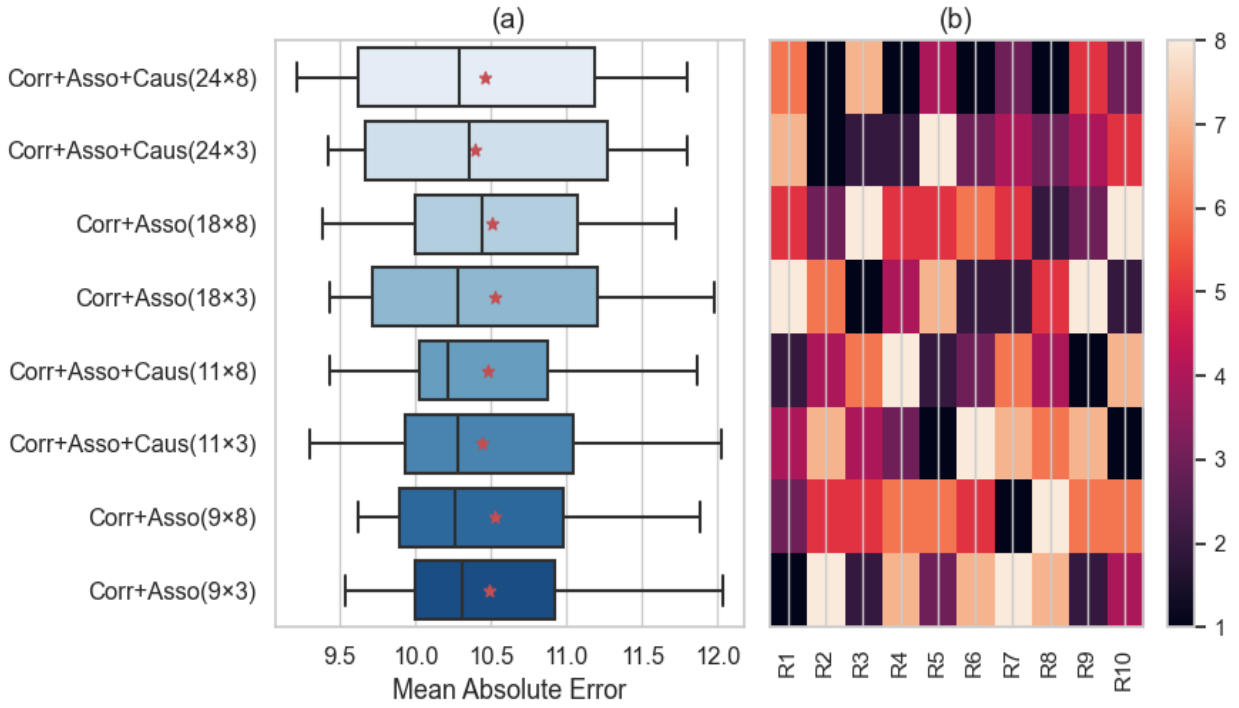

Figure 5-6. The performance of a model was evaluated using different combination of correlation features, association features and causation features. Box plots in (a) illustrate the distribution of mean absolute error (MAE) for each feature set. In (b), a colormap displays the ranking of the results from 10 different train-test splits.

We then merged the association, correlation, and causation features to examine whether incorporating causation features could enhance the prediction performance. Figure 5-6 compares eight predictions from the combinations of association, correlation, and causation features in bar plots and colormap. The top four feature sets comprise the top 10 features selected from combinations of correlation, association, and causation. The number in the following parentheses indicate the feature number fed into the model without any overlap. With causation features, model would include 24 features instead of 18 features of association and correlation. Two of them consist of only 3 sensors (sensor 5,6,7) which are located opposite to the source and considered more important. In contrast, the lower four feature sets follow a similar pattern, analyzing the top 5 features. When considering only correlation and association features, there are 9 features used.

However, if causation features are included in the model, the feature size increases to 11. A noticeable improvement in prediction model performance is observed in the box plots when high causation features are included in the model. In other words, adding causation features can improve the prediction model performance because causation implies a directional relationship between the variables, rather than just a correlation or association between them. According to the colormap, models that include causation features tend to rank higher.

5.6 Conclusions and Discussion

This work questions current data-driven models and initiates a study of knowledge-driven models that incorporate domain expertise into machine learning pipelines. Overall, both data- and knowledge-driven methods could provide robust estimation for the propagation of an embedded mechanical discontinuity in porous materials with different sizes and matrix properties. Generalized machine learning workflow could precisely predict the crack location, size and orientation through different linear growth stages, namely initial, intermediate, and final stages. However, current machine learning strategies ignore the latent causal-effect relationship underlying the problem. Therefore, this study suggests the new knowledge-driven causal model to emphasis latent causal network behind various statistical features of designed fracture system. In contrast to the traditional data-driven approach, knowledge-driven causal model illustrates their ability in untangling and explaining invariant causal relationships rather than simple correlation. The most significant finding is that waveform fluctuations such as positive turning, negative turning, and zero crossing have been identified as geophysical signatures of crack propagation which could applied to recognize cracks/fractures at different stages during propagation by analyzing signals from multipoint sensor system placed on the surface of the material. For more

complex physical related fracture propagation, reoccur number, the sum of reoccur values, and variation coefficient of the waveforms are causal signatures that highly influenced by the crack length change. Causal-related features could provide a deeper understanding of the underlying mechanisms that drive the relationships between variables, leading to better models with improved accuracy. We believe causality is the key component attempts to overcome the black boxes of machine learning. In near future, similar knowledge-driven causal discovery will be valuable area in the development of artificial intelligent.

CHAPTER VI

CONCLUSIONS AND FUTURE WORK

This study provides a comprehensive approach to understanding the characterization and propagation of fractures in materials by analyzing the multipoint waveform measurements. The chapters presented in this work are interconnected, Chapter 2 highlights the use of classification algorithms to visualize discontinuity orientation, dispersion, and spatial distribution in formation by using waveforms arrival times. Chapter 3 expands on this by incorporating whole waveform data to monitor linear discontinuity propagation in 2D materials through three stages with a data-driven approach. Chapter 4 analyzes causal inference techniques to identify the causal signatures of crack propagation from a feature space for linear propagation and physical-based crack propagation. The identification of causal signatures of crack propagation has numerous applications in materials science, hydraulic fracturing, and engineering. By understanding the causal relationships between the crack propagation process and waveform measurements, engineers can develop more effective strategies for controlling crack growth and improving the durability of materials.

Finally, in Chapter 5, we propose the knowledge-driven causal model to take advantage of specific domain knowledge when processing the input data. The knowledge-driven method provides a valuable approach for understanding and predicting crack propagation behavior in materials. By leveraging domain knowledge and causal inference techniques, this method can provide insights into the underlying physical processes driving crack growth and help to identify key factors that influence crack propagation. On the other hand, knowledge-driven models that use causal features can be more robust to changes in the data or the environment, as they are based on fundamental causal relationships rather than just correlations/associations.

The identification of causal signatures of crack propagation using causal inference techniques is a complex and challenging task. One of the main challenges is the need to accurately measure and analyze a wide range of statistical and physical parameters from waveforms, to identify the key factors driving by crack growth. Additionally, observations made from one or two flaws may provide a limited understanding of a much more complex behavior of the rock mass due to the large number of possible interactions among the discontinuities. Further investigations are necessary to validate the discovered geophysical signatures in field application.

REFERENCES

A. Mandelis, "DIFFUSION WAVES AND THEIR USES," Physics today, vol. 53, no. 8, pp. 29-34, 2000.

Abdi, H., & Williams, L. J. (2010). Principal component analysis. Wiley interdisciplinary reviews: computational statistics, 2(4), 433-459.

Adams, R. D., Cawley, P., Pye, C. J., & Stone, B. J. (1978). A vibration technique for non-destructively assessing the integrity of structures. Journal of mechanical engineering science, 20(2), 93-100.

Aghli, G., Soleimani, B., Moussavi-Harami, R., & Mohammadian, R. (2016). Fractured zones detection using conventional petrophysical logs by differentiation method and its correlation with image logs. Journal of Petroleum Science and Engineering, 142, 152-162.

Akande, K. O., Owolabi, T. O., & Olatunji, S. O. (2015). Investigating the effect of correlation-based feature selection on the performance of support vector machines in reservoir characterization. Journal of Natural Gas Science and Engineering, 22, 515-522.

Al-Bazzaz, W. H., Ali, A. A., & Al-Attar, M. A. (2009, December). Fracture geometry characterizations through physical modeling. In Kuwait International Petroleum Conference and Exhibition. OnePetro.

Aleardi, M. (2015). Seismic velocity estimation from well log data with genetic algorithms in comparison to neural networks and multilinear approaches. Journal of Applied Geophysics, 117, 13-22.

Ameen, M. S., MacPherson, K., Al-Marhoon, M. I., & Rahim, Z. (2012). Diverse fracture properties and their impact on performance in conventional and tight-gas reservoirs, Saudi Arabia: The Unayzah, South Haradh case studyUnayzah Conventional and Tight-Gas Fractures. AAPG bulletin, 96(3), 459-492.

Andersson, J., & Dverstorp, B. (1987). Conditional simulations of fluid flow in three-dimensional networks of discrete fractures. Water Resources Research, 23(10), 1876-1886.

Anifowose, F., Labadin, J., & Abdulraheem, A. (2015). Improving the prediction of petroleum reservoir characterization with a stacked generalization ensemble model of support vector machines. Applied Soft Computing, 26, 483-496.

Arumugam, V., Kumar, C. S., Santulli, C., Sarasini, F., & Stanley, A. J. (2011). A global method for the identification of failure modes in fiberglass using acoustic emission. Journal of Testing and Evaluation, 39(5), 1.

Ayatollahi, M. R., & Aliha, M. R. M. (2007). Fracture toughness study for a brittle rock subjected to mixed mode I/II loading. International Journal of Rock Mechanics and Mining Sciences, 44(4), 617-624.

ASTM, A. (1986). Standard test method of unconfined compressive strength of intact rock core specimens. ASTM Publication.

Bakku, S. K. (2015). Fracture characterization from seismic measurements in a borehole (Doctoral dissertation, Massachusetts Institute of Technology).

Barandas, M., Folgado, D., Fernandes, L., Santos, S., Abreu, M., Bota, P., ... & Gamboa, H. (2020). TSFEL: Time series feature extraction library. SoftwareX, 11, 100456.

Batista, G. E., Wang, X., & Keogh, E. J. (2011, April). A complexity-invariant distance measure for time series. In Proceedings of the 2011 SIAM international conference on data mining (pp. 699-710). Society for Industrial and Applied Mathematics.

Berrar, D. (2018). Bayes' theorem and naive Bayes classifier. Encyclopedia of Bioinformatics and Computational Biology: ABC of Bioinformatics, 403.

Berrar, D. (2019). Cross-Validation.

Bhoumick, P., Sondergeld, C., & Rai, C. S. (2018, June). Mapping hydraulic fracture in pyrophyllite using shear wave. In 52nd US Rock Mechanics/Geomechanics Symposium. OnePetro.

Bogatkov, D., & Babadagli, T. (2010). Fracture network modeling conditioned to pressure transient and tracer test dynamic data. Journal of Petroleum Science and Engineering, 75(1-2), 154-167.

Bolón-Canedo, V., Sánchez-Maroño, N., & Alonso-Betanzos, A. (2015). Recent advances and emerging challenges of feature selection in the context of big data. Knowledge-based systems, 86, 33-45.

Breiman, L. (2001). Random forests. Machine learning, 45(1), 5-32.

Bressan, T. S., de Souza, M. K., Girelli, T. J., & Junior, F. C. (2020). Evaluation of machine learning methods for lithology classification using geophysical data. Computers & Geosciences, 139, 104475.

Bühlmann, P., & Van De Geer, S. (2011). Statistics for high-dimensional data: methods, theory and applications. Springer Science & Business Media.

Bull, D. J., Spearing, S. M., Sinclair, I., & Helfen, L. (2013). Three-dimensional assessment of low velocity impact damage in particle toughened composite laminates using micro-focus X-ray computed tomography and synchrotron radiation laminography. Composites Part A: Applied Science and Manufacturing, 52, 62-69.

Bui, H. H., Kodikara, J. K., Bouazza, A., Haque, A., & Ranjith, P. G. (2014). A novel computational approach for large deformation and post-failure analyses of segmental retaining wall systems. International Journal for Numerical and Analytical Methods in Geomechanics, 38(13), 1321-1340.

Byun, H., Kim, J., Yoon, D., Kang, I. S., & Song, J. J. (2021). A deep convolutional neural network for rock fracture image segmentation. Earth Science Informatics, 14(4), 1937-1951.

C. Nicholson, "A beginner's guide to multilayer perceptrons (MLP)," ed: Pathmind, 2019.

C. M. Bishop, Pattern recognition and machine learning. springer, 2006.

Caliendo, M., & Kopeinig, S. (2008). Some practical guidance for the implementation of propensity score matching. Journal of economic surveys, 22(1), 31-72.

Cao, P., Liu, T., Pu, C., & Lin, H. (2015). Crack propagation and coalescence of brittle rock-like specimens with pre-existing cracks in compression. Engineering geology, 187, 113-121.

Carpinteri, A., Lacidogna, G., & Pugno, N. (2007). Structural damage diagnosis and life-time assessment by acoustic emission monitoring. Engineering Fracture Mechanics, 74(1-2), 273-289.

Casini, G., Hunt, D. W., Monsen, E., & Bounaim, A. (2016). Fracture characterization and modeling from virtual outcrops. AAPG Bulletin, 100(1), 41-61.

Cohen, I., Huang, Y., Chen, J., Benesty, J., Benesty, J., Chen, J., ... & Cohen, I. (2009). Pearson correlation coefficient. Noise reduction in speech processing, 1-4.

Chakravarty, A., Misra, S., & Rai, C. S. (2021). Visualization of hydraulic fracture using physics-informed clustering to process ultrasonic shear waves. International Journal of Rock Mechanics and Mining Sciences, 137, 104568.

Chang, S. H., Lee, C. I., & Jeon, S. (2002). Measurement of rock fracture toughness under modes I and II and mixed-mode conditions by using disc-type specimens. Engineering geology, 66(1-2), 79-97.

Chehrazi, A., Rahimpour-Bonab, H., & Rezaee, M. R. (2013). Seismic data conditioning and neural network-based attribute selection for enhanced fault detection. Petroleum Geoscience, 19(2), 169-183.

Chen, J., Zhou, M., Huang, H., Zhang, D., & Peng, Z. (2021). Automated extraction and evaluation of fracture trace maps from rock tunnel face images via deep learning. International Journal of Rock Mechanics and Mining Sciences, 142, 104745.

Chernozhukov, V., Chetverikov, D., Demirer, M., Duflo, E., Hansen, C., Newey, W., & Robins, J. (2016). Double/debiased machine learning for treatment and causal parameters. arXiv preprint arXiv:1608.00060.

Chernozhukov, V., Chetverikov, D., Demirer, M., Duflo, E., Hansen, C., & Newey, W. (2017). Double/debiased/neyman machine learning of treatment effects. American Economic Review, 107(5), 261-65.

Chernozhukov, V., Chetverikov, D., Demirer, M., Duflo, E., Hansen, C., Newey, W., & Robins, J. (2018). Double/debiased machine learning for treatment and structural parameters.

Cho, Y., Gibson Jr, R. L., Vasilyeva, M., & Efendiev, Y. (2018). Generalized multiscale finite elements for simulation of elastic-wave propagation in fractured media. Geophysics, 83(1), WA9-WA20.

Conn, V. S. (2017). Don't rock the analytical boat: Correlation is not causation.

Cottrell, M. G., & Dershowitz, B. (2012). A discrete fracture network approach for enhancing development of unconventional fractured reservoirs. Society of Petroleum Engineers YP Event, The Geological Society, London, United Kingdom, 8.

Cunha, A., Pochet, A., Lopes, H., & Gattass, M. (2020). Seismic fault detection in real data using transfer learning from a convolutional neural network pre-trained with synthetic seismic data. Computers & Geosciences, 135, 104344.

Christ, M., Braun, N., Neuffer, J., & Kempa-Liehr, A. W. (2018). Time series feature extraction on basis of scalable hypothesis tests (tsfresh–a python package). Neurocomputing, 307, 72-77.

D. Silin, V. Korneev, and G. Goloshubin, "Pressure diffusion waves in porous media," in SEG Technical Program Expanded Abstracts 2003: Society of Exploration Geophysicists, 2003, pp. 2323-2326.

De Silva, V., & Tenenbaum, J. B. (2002, December). Global versus local methods in nonlinear dimensionality reduction. In NIPS (Vol. 15, pp. 705-712).

De Winter, J. C., Gosling, S. D., & Potter, J. (2016). Comparing the Pearson and Spearman correlation coefficients across distributions and sample sizes: A tutorial using simulations and empirical data. Psychological methods, 21(3), 273.

Dershowitz WS, Doe TW, Uchida M and Hermanson J. (2003) Correlations between Fracture Size, Transmissivity, and Aperture. P. Culligan, H. Einstein, and A. Whittle, ed. Soil Rock America, 2003. Proceedings of the 12th Panamerican Conference on Soil Mechanics and Geotechnical Engineering, 887-891

Dershowitz, W. S., & Doe, T. W. (1988, May). Practical applications of discrete fracture approaches in hydrology, mining, and petroleum extraction. In Symposium Proceedings of the International Conference on Fluid Flow in Fractured Rocks, Atlanta, Georgia (pp. 15-18).

Detto, M., Molini, A., Katul, G., Stoy, P., Palmroth, S., & Baldocchi, D. (2012). Causality and persistence in ecological systems: a nonparametric spectral Granger causality approach. The American Naturalist, 179(4), 524-535.

Deng, X. (2020). Examining the effects of public policies and addiction on purchase of tobacco products with causal inference and machine learning methods.

Dong, Y., & Ansari, F. (2011). Non-destructive testing and evaluation (NDT/NDE) of civil structures rehabilitated using fiber reinforced polymer (FRP) composites. In Service life estimation and extension of civil engineering structures (pp. 193-222). Woodhead Publishing.

Drucker, H., Burges, C. J., Kaufman, L., Smola, A. J., & Vapnik, V. (1997). Support vector regression machines. In Advances in neural information processing systems (pp. 155-161).

Du, K., Li, X., Tao, M., & Wang, S. (2020). Experimental study on acoustic emission (AE) characteristics and crack classification during rock fracture in several basic lab tests. International Journal of Rock Mechanics and Mining Sciences, 133, 104411.

Dubnov, S. (2004). Generalization of spectral flatness measure for non-gaussian linear processes. IEEE Signal Processing Letters, 11(8), 698-701.

Duchene, P., Chaki, S., Ayadi, A., & Krawczak, P. (2018). A review of non-destructive techniques used for mechanical damage assessment in polymer composites. Journal of materials science, 53(11), 7915-7938.

Duesberg, P. H. (1989). Human immunodeficiency virus and acquired immunodeficiency syndrome: Correlation but not causation. Proceedings of the National Academy of Sciences, 86(3), 755-764.

Durak, L., & Arikan, O. (2003). Short-time Fourier transform: two fundamental properties and an optimal implementation. IEEE Transactions on Signal Processing, 51(5), 1231-1242.

Dwivedi, S. K., Vishwakarma, M., & Soni, A. (2018). Advances and researches on non-destructive testing: A review. Materials Today: Proceedings, 5(2), 3690-3698.

Eagleman, D. M., & Holcombe, A. O. (2002). Causality and the perception of time. Trends in cognitive sciences, 6(8), 323-325.

Firouzi, K., Cox, B., Treeby, B., & Saffari, N. (2012). A first-order k-space model for elastic wave propagation in heterogeneous media. The Journal of the Acoustical Society of America, 132(3), 1271-1283.

Fix, E., Hodges, J.L. Discriminatory analysis, nonparametric discrimination: Consistency properties. Technical Report 4, USAF School of Aviation Medicine, Randolph Field, Texas, 1951.

Foster, J., Misra, S., FALOLA, Y., & Bhatia, M. (2021). Preemptive Detection of High Water-Cut Wells in Delaware Basin using a Joint Unsupervised and Supervised Learning Approach. https://www.essoar.org/doi/abs/10.1002/essoar.10507756.2

Freund, Y., & Schapire, R. E. (1996, July). Experiments with a new boosting algorithm. In icml (Vol. 96, pp. 148-156).

Friedman, J. H. (2001). Greedy function approximation: a gradient boosting machine. Annals of statistics, 1189-1232.

Friedman, J. H. (2002). Stochastic gradient boosting. Computational statistics & data analysis, 38(4), 367-378.

G. Hamada and V. Joseph, "Developed correlations between sound wave velocity and porosity, permeability and mechanical properties of sandstone core samples," Petroleum Research, vol. 5, no. 4, pp. 326-338, 2020.

Ganguly, E., Misra, S., & Wu, Y. (2020, October). Generalizable data-driven techniques for microstructural analysis of shales. In SPE Annual Technical Conference and Exhibition. OnePetro.

Garcea, S. C., Wang, Y., & Withers, P. J. (2018). X-ray computed tomography of polymer composites. Composites Science and Technology, 156, 305-319.

Gunasekaran, S., Paulsen, M. R., & Shove, G. C. (1985). Optical methods for nondestructive quality evaluation of agricultural and biological materials. Journal of Agricultural Engineering Research, 32(3), 209-241.

Gholizadeh, S. (2016). A review of non-destructive testing methods of composite materials. Procedia structural integrity, 1, 50-57.

Guo, R., Cheng, L., Li, J., Hahn, P.R., & Liu, H. (2020). A Survey of Learning Causality with Data. ACM Computing Surveys (CSUR).

Guo, S., & Fraser, M. W. (2014). Propensity score analysis: Statistical methods and applications (Vol. 11). SAGE publications.

Haeri, H., Shahriar, K., Marji, M. F., & Moarefvand, P. (2014). Experimental and numerical study of crack propagation and coalescence in pre-cracked rock-like disks. International Journal of Rock Mechanics and Mining Sciences, 67, 20-28.

Herve Conge, 2022. Extensional fault around Moab fault, Utah, USA. Available from: https://www.sciencephoto.com/media/1066151/view/moab-fault-utah-usa.

Hale, D. (2012, November). Fault surfaces and fault throws from 3D seismic images. In 2012 SEG Annual Meeting. OnePetro.

Hale, D. (2013). Methods to compute fault images, extract fault surfaces, and estimate fault throws from 3D seismic images. Geophysics, 78(2), O33-O43.

Hart, B. S., Pearson, R., & Rawling, G. C. (2002). 3-D seismic horizon-based approaches to fracture-swarm sweet spot definition in tight-gas reservoirs. The Leading Edge, 21(1), 28-35.

Haukoos, J. S., & Lewis, R. J. (2015). The propensity score. Jama, 314(15), 1637-1638.

He, J., & Misra, S. (2019). Generation of synthetic dielectric dispersion logs in organic-rich shale formations using neural-network models. Geophysics, 84(3), D117-D129.

Hicks, J. (1980). Causality in economics. Australian National University Press.

Hitchcock, C. (2020). Causal Models. In E. N. Zalta (Ed.), The Stanford encyclopedia of philosophy. Metaphysics Research Lab, Stanford University.

Holland, P. W. (1986). Statistics and causal inference. Journal of the American statistical Association, 81(396), 945-960.

Hu, L. (2022). A review of mechanical mechanism and prediction of natural fracture in shale. Arabian Journal of Geosciences, 15(6), 1-16.

Hunter, A., Moore, B. A., Mudunuru, M., Chau, V., Tchoua, R., Nyshadham, C., ... & Srinivasan, G. (2019). Reduced-order modeling through machine learning and graph-theoretic approaches for brittle fracture applications. Computational Materials Science, 157, 87-98.

Huang, H. W., Li, Q. T., & Zhang, D. M. (2018). Deep learning based image recognition for crack and leakage defects of metro shield tunnel. Tunnelling and underground space technology, 77, 166-176.

Hume, D. (1751). Philosophical essays concerning human understanding (No. 35). M. Cooper.

I. Rish, "An empirical study of the naive Bayes classifier," in IJCAI 2001 workshop on empirical methods in artificial intelligence, 2001, vol. 3, no. 22, pp. 41-46.

Ibrahim, M. E. (2014). Nondestructive evaluation of thick-section composites and sandwich structures: A review. Composites Part A: Applied Science and Manufacturing, 64, 36-48.

Illman, W. A. (2014). Hydraulic tomography offers improved imaging of heterogeneity in fractured rocks. Groundwater, 52(5), 659-684.

ISRM, I. (1978). Suggested methods for the quantitative description of discontinuities in rock masses. Commission on the standardization of Laboratory and Field Tests in Rock Mechanics, ISRM.

Isah, B. W., Mohamad, H., Ahmad, N. R., Harahap, I. S. H., & Al-Bared, M. A. M. (2020, April). Uniaxial compression test of rocks: Review of strain measuring instruments. In IOP Conference Series: Earth and Environmental Science (Vol. 476, No. 1, p. 012039). IOP Publishing.

James St. John, 2019. Fractured 7 folded gyprock in the Permian, New Mexico, USA. Available from: https://commons.wikimedia.org/wiki/File:Folded_gyprock.jpg.

J. A. Sethian, "A fast marching level set method for monotonically advancing fronts," Proceedings of the National Academy of Sciences, vol. 93, no. 4, pp. 1591-1595, 1996.

J. J. Zhang, Applied Petroleum Geomechanics. Gulf Professional Publishing, 2019.

J. U. Kim, A. Datta-Gupta, R. Brouwer, and B. Haynes, "Calibration of high-resolution reservoir models using transient pressure data," in SPE Annual Technical Conference and Exhibition, 2009: Society of Petroleum Engineers.

Jager, K. J., Zoccali, C., Macleod, A., & Dekker, F. W. (2008). Confounding: what it is and how to deal with it. Kidney international, 73(3), 256-260.

Kless Gyzen, 2020. Cracked rock sample. Available from: https://sketchfab.com/3d-models/square-rock-cracked-updated-materials-22aa59eb632242c3ac2441949c6750b6.

K. Kira and L. A. Rendell, "A practical approach to feature selection," in Machine Learning Proceedings 1992: Elsevier, 1992, pp. 249-256.

Kammer, D. (2014). Slip fronts at frictional interfaces: A Numerical and Theoretical Study. EPFL Thesis, 12.

Kamrava, S., Tahmasebi, P., & Sahimi, M. (2019). Enhancing images of shale formations by a hybrid stochastic and deep learning algorithm. Neural Networks, 118, 310-320.

Kato, T., & Nishioka, T. (2005). Analysis of micro--macro material properties and mechanical effects of damaged material containing periodically distributed elliptical microcracks. International journal of fracture, 131(3), 247-266.

Khoshbakht, F., Memarian, H., & Mohammadnia, M. (2009). Comparison of Asmari, Pabdeh and Gurpi formation's fractures, derived from image log. Journal of Petroleum science and Engineering, 67(1-2), 65-74.

Kinra, V. K., Ganpatye, A. S., & Maslov, K. (2006). Ultrasonic ply-by-ply detection of matrix cracks in laminated composites. Journal of Nondestructive Evaluation, 25(1), 37-49.

Klapuri, A., & Davy, M. (Eds.). (2007). Signal processing methods for music transcription, chapter 5. Springer Science & Business Media.

Kosari, E., Ghareh-Cheloo, S., Kadkhodaie-Ilkhchi, A., & Bahroudi, A. (2015). Fracture characterization by fusion of geophysical and geomechanical data: a case study from the Asmari reservoir, the Central Zagros fold-thrust belt. Journal of Geophysics and Engineering, 12(1), 130-143.

Knight, E. E., Rougier, E., Lei, Z., Euser, B., Chau, V., Boyce, S. H., ... & Froment, M. (2020). HOSS: an implementation of the combined finite-discrete element method. Computational Particle Mechanics, 7(5), 765-787.

L. Bottou, "Large-scale machine learning with stochastic gradient descent," in *Proceedings of COMPSTAT'2010*: Springer, 2010, pp. 177-186.

Lai, J., Wang, G., Fan, Z., Wang, Z., Chen, J., Zhou, Z., ... & Xiao, C. (2017). Fracture detection in oil-based drilling mud using a combination of borehole image and sonic logs. Marine and Petroleum Geology, 84, 195-214.

Leal, J. A., Ochoa, L. H., & García, J. A. (2016). Identification of natural fractures using resistive image logs, fractal dimension and support vector machines. Ingeniería e Investigación, 36(3), 125-132.

Lemy F, Hadjigeorgiou J (2003) Discontinuity trace map construction using photographs of rock exposures. Int J Rock Mech Min Sci 40(6):903–917.

Li, H., Misra, S., & Liu, R. (2021). Characterization of mechanical discontinuities based on data-driven classification of compressional-wave travel times. International Journal of Rock Mechanics and Mining Sciences, 143, 104793.

Li, L., & Lee, S. H. (2008). Efficient field-scale simulation of black oil in a naturally fractured reservoir through discrete fracture networks and homogenized media. SPE Reservoir evaluation & engineering, 11(04), 750-758.

Liu, H., & Zhang, S. (2012). Noisy data elimination using mutual k-nearest neighbor for classification mining. Journal of Systems and Software, 85(5), 1067-1074.

Liu, M., Jin, Y., Lu, Y., Chen, M., & Wen, X. (2015). Oil-based critical mud weight window analyses in HTHP fractured tight formation. Journal of Petroleum Science and Engineering, 135, 750-764.

Liu, R., & Misra, S. (2020). Data-Driven Classification of Materials with Open or Closed Mechanical Discontinuities Based on Multipoint, Multimodal Travel-Time Measurements.

Liu, R., & Misra, S. (2022). A generalized machine learning workflow to visualize mechanical discontinuity. Journal of Petroleum Science and Engineering, 210, 109963.

Liu, R., & Misra, S. (2022). Monitoring the propagation of mechanical discontinuity using data-driven causal discovery and supervised learning. Mechanical Systems and Signal Processing, 170, 108791.

Liu, R., & Misra, S. (2022). Machine learning assisted detection and localization of mechanical discontinuity. International Journal of Fracture, 236(2), 219-234.

Long, J. C., Remer, J. S., Wilson, C. R., & Witherspoon, P. A. (1982). Porous media equivalents for networks of discontinuous fractures. Water resources research, 18(3), 645-658.

Mike Norton, 2020. Well-developed joint sets on flagstones at St. Mary's Chapel, Caithness, Scotland. Available from: https://commons.wikimedia.org/wiki/File:Joints_Caithness.JPG

M. Caputo, J. M. Carcione, and F. Cavallini. Wave simulation in biologic media based on the Kelvin-voigt fractional-derivative stress-strain relation. Ultrasound Med. Biol., 37(6):996–1004, 2011.

M. Greenberg and J. Castagna, "Shear-wave velocity estimation in porous rocks: theoretical formulation, preliminary verification and applications1," Geophysical prospecting, vol. 40, no. 2, pp. 195-209, 1992.

MacKinnon, D. P., Krull, J. L., & Lockwood, C. M. (2000). Equivalence of the mediation, confounding and suppression effect. Prevention science, 1(4), 173-181.

Maerten, L., Pollard, D. D., & Maerten, F. (2001). Digital mapping of three-dimensional structures of the Chimney Rock fault system, central Utah. Journal of Structural Geology, 23(4), 585-592.

Mallat, S. G. (1989). A theory for multiresolution signal decomposition: the wavelet representation. IEEE transactions on pattern analysis and machine intelligence, 11(7), 674-693.

Mardia, K. V., & Zemroch, P. J. (1975). Algorithm AS 86: The von Mises distribution function. Journal of the Royal Statistical Society. Series C (Applied Statistics), 24(2), 268-272.

Marins, M. A., Barros, B. D., Santos, I. H., Barrionuevo, D. C., Vargas, R. E., Prego, T. D. M., ... & Netto, S. L. (2021). Fault detection and classification in oil wells and production/service lines using random forest. Journal of Petroleum Science and Engineering, 197, 107879.

Martin, E., Jaros, J., & Treeby, B. E. (2019). Experimental validation of k-wave: Nonlinear wave propagation in layered, absorbing fluid media. IEEE transactions on ultrasonics, ferroelectrics, and frequency control, 67(1), 81-91.

Martinez, L. P., Hughes, R. G., & Wiggins, M. L. (2002). Identification and characterization of naturally fractured reservoirs using conventional well logs. The University of Oklahoma, 1-23.

Mast, T. D., Souriau, L. P., Liu, D. L., Tabei, M., Nachman, A. I., & Waag, R. C. (2001). A k-space method for large-scale models of wave propagation in tissue. IEEE transactions on ultrasonics, ferroelectrics, and frequency control, 48(2), 341-354.

Mirjalili, S., Mirjalili, S. M., & Lewis, A. (2014). Let a biogeography-based optimizer train your multi-layer perceptron. Information Sciences, 269, 188-209.

Misra, S., & He, J. (2019). Stacked neural network architecture to model the multifrequency conductivity/permittivity responses of subsurface shale formations. Machine Learning for Subsurface Characterization, 103.

Misra, S., & Li, H. (2019). Noninvasive fracture characterization based on the classification of sonic wave travel times. Machine Learning for Subsurface Characterization, 243.

Misra, S., Li, H., & He, J. (2020). Noninvasive fracture characterization based on the classification of sonic wave travel times. Machine Learning for Subsurface Characterization, 243-287.

Moore, B. A., Rougier, E., O'Malley, D., Srinivasan, G., Hunter, A., & Viswanathan, H. (2018). Predictive modeling of dynamic fracture growth in brittle materials with machine learning. Computational Materials Science, 148, 46-53.

Moraffah, R., Karami, M., Guo, R., Raglin, A., & Liu, H. (2020). Causal Interpretability for Machine Learning - Problems, Methods and Evaluation. ACM SIGKDD Explorations Newsletter, 22, 18 - 33.

Murphy, K. P. (2006). Naive bayes classifiers. University of British Columbia, 18(60), 1-8.

N. Watson, "Ultrasound tomography," in Industrial Tomography: Elsevier, 2015, pp. 235-261.

Naul, B., van der Walt, S., Crellin-Quick, A., Bloom, J. S., & Pérez, F. (2016). cesium: Open-source platform for time-series inference. arXiv preprint arXiv:1609.04504.

Natekin, A., & Knoll, A. (2013). Gradient boosting machines, a tutorial. Frontiers in neurorobotics, 7, 21.

National Research Council. (1996). Rock fractures and fluid flow: contemporary understanding and applications. National Academies Press.

Niles, H. E. (1922). Correlation, causation and Wright's theory of" path coefficients". Genetics, 7(3), 258.

Nogueira, A. R., Pugnana, A., Ruggieri, S., Pedreschi, D., & Gama, J. (2022). Methods and tools for causal discovery and causal inference. Wiley Interdisciplinary Reviews: Data Mining and Knowledge Discovery, 12(2), e1449.

Olariu, M. I., Ferguson, J. F., Aiken, C. L., & Xu, X. (2008). Outcrop fracture characterization using terrestrial laser scanners: Deep-water Jackfork sandstone at Big Rock Quarry, Arkansas. Geosphere, 4(1), 247-259.

Osisanwo, F. Y., Akinsola, J. E. T., Awodele, O., Hinmikaiye, J. O., Olakanmi, O., & Akinjobi, J. (2017). Supervised machine learning algorithms: classification and comparison. International Journal of Computer Trends and Technology (IJCTT), 48(3), 128-138.

Osogba, O., Misra, S., & Xu, C. (2020). Machine learning workflow to predict multi-target subsurface signals for the exploration of hydrocarbon and water. Fuel, 278, 118357.

P. Bhoumick, C. Sondergeld, and C. Rai, "Mapping hydraulic fracture in pyrophyllite using shear wave," in 52nd US Rock Mechanics/Geomechanics Symposium, 2018: American Rock Mechanics Association.

Pearl, J. (1998). Graphs, causality, and structural equation models. Sociological Methods & Research, 27(2), 226-284.

Pearl, J. (2009). Causality. Cambridge university press.

Peterson, L. E. (2009). K-nearest neighbor. Scholarpedia, 4(2), 1883.

Q. H. Liu. Large-scale simulations of electromagnetic and acoustic measurements using the pseudospectral time-domain (PSTD) algorithm. IEEE. T. Geosci. Remote, 37(2):917–926, 1999.

Quinlan, J. R. (1996, August). Bagging, boosting, and C4. 5. In Aaai/Iaai, vol. 1 (pp. 725-730).

R. J. Weimer and R. Tillman, "Sandstone reservoirs," in International Petroleum Exhibition and Technical Symposium, 1982: Society of Petroleum Engineers.

Rajabi, M., Beheshtian, S., Davoodi, S., Ghorbani, H., Mohamadian, N., Radwan, A. E., & Alvar, M. A. (2021). Novel hybrid machine learning optimizer algorithms to prediction of fracture density by petrophysical data. Journal of Petroleum Exploration and Production Technology, 11(12), 4375-4397.

Reid TR, Harrison JP. An automated tracing of rock mass discontinuities from digital images. Int. J. Rock Mech. Min. Sci. 1997. Vol. 34, No. 3/4, p. 335, paper no. 256.

Richard, H. A., Schramm, B., & Schirmeisen, N. H. (2014). Cracks on mixed mode loading–theories, experiments, simulations. International Journal of Fatigue, 62, 93-103.

Rish, I. (2001, August). An empirical study of the naive Bayes classifier. In IJCAI 2001 workshop on empirical methods in artificial intelligence (Vol. 3, No. 22, pp. 41-46).

Robinson, P. C. (1984). Connectivity, flow and transport in network models of fractured media (Doctoral dissertation, University of Oxford).

Rosenbaum, P. R., & Rubin, D. B. (1983). The central role of the propensity score in observational studies for causal effects. Biometrika, 70(1), 41-55.

Rubin, D. B. (1974). Estimating causal effects of treatments in randomized and nonrandomized studies. Journal of educational Psychology, 66(5), 688.

Rubin, D. B. (1977). Assignment to treatment group on the basis of a covariate. Journal of educational Statistics, 2(1), 1-26.

Rubin, D. B. (1978). Bayesian inference for causal effects: The role of randomization. The Annals of statistics, 34-58.

Rubin, D. B. (1980). Randomization analysis of experimental data: The Fisher randomization test comment. Journal of the American statistical association, 75(371), 591-593.

Rubin, D. B. (2005). Causal inference using potential outcomes: Design, modeling, decisions. Journal of the American Statistical Association, 100(469), 322-331.

Ruta, D., & Gabrys, B. (2005). Classifier selection for majority voting. Information fusion, 6(1), 63-81.

Sahouryeh, E., Dyskin, A. V., & Germanovich, L. N. (2002). Crack growth under biaxial compression. Engineering Fracture Mechanics, 69(18), 2187-2198.

Schmidt, J., Marques, M. R., Botti, S., & Marques, M. A. (2019). Recent advances and applications of machine learning in solid-state materials science. npj Computational Materials, 5(1), 1-36.

Scholkopf, B. (2019). Causality for Machine Learning.

Schwarzer, M., Rogan, B., Ruan, Y., Song, Z., Lee, D. Y., Percus, A. G., ... & Srinivasan, G. (2019). Learning to fail: Predicting fracture evolution in brittle material models using recurrent graph convolutional neural networks. Computational Materials Science, 162, 322-332.

Schwenk, H., & Bengio, Y. (1998). Training methods for adaptive boosting of neural networks. In Advances in neural information processing systems (pp. 647-653).

Scruby, C. B. (1987). An introduction to acoustic emission. Journal of Physics E: Scientific Instruments, 20(8), 946.

Shen, B., Stephansson, O., Einstein, H. H., & Ghahreman, B. (1995). Coalescence of fractures under shear stresses in experiments. Journal of Geophysical Research: Solid Earth, 100(B4), 5975-5990.

Shapley, L. (1971). Cores of convex games. International Journal of Game Theory, 1, 11-26.

Shapley, L. (1988). A Value for n-person Games.

Sharma, A., & Kiciman, E. (2019). DoWhy: A Python package for causal inference. In KDD 2019 workshop.

Shoemaker, S. (1980). Causality and properties. In Time and cause (pp. 109-135). Springer, Dordrecht.

Smith, J. E., & Peterson, E. J. (2012). The Los Alamos Science Pillars The Science of Signatures (No. LA-UR-12-24168). Los Alamos National Lab. (LANL), Los Alamos, NM (United States).

Simon, R. (2003). Supervised analysis when the number of candidate features (p) greatly exceeds the number of cases (n). ACM SIGKDD Explorations Newsletter, 5(2), 31-36.

Smith, L., & Schwartz, F. W. (1984). An analysis of the influence of fracture geometry on mass transport in fractured media. Water Resources Research, 20(9), 1241-1252.

Song, Y., Liang, J., Lu, J., & Zhao, X. (2017). An efficient instance selection algorithm for k nearest neighbor regression. Neurocomputing, 251, 26-34.

Su, J., & Zhang, H. (2006, July). A fast decision tree learning algorithm. In AAAI (Vol. 6, pp. 500-505).

Talebkeikhah, M., Sadeghtabaghi, Z., & Shabani, M. (2021). A comparison of machine learning approaches for prediction of permeability using well log data in the hydrocarbon reservoirs. Journal of Human, Earth, and Future, 2(2), 82-99.

Tian, X., & Daigle, H. (2018). Machine-learning-based object detection in images for reservoir characterization: A case study of fracture detection in shales. The Leading Edge, 37(6), 435-442.

Tokhmechi, B. (2009). Identification and categorization of joints using data fusion approach, emphasizing on Asmari Formation. University of Tehran. 155pp.

Trabelsi, A., Elouedi, Z., & Lefevre, E. (2019). Decision tree classifiers for evidential attribute values and class labels. Fuzzy Sets and Systems, 366, 46-62.

Treeby, B. E., & Cox, B. T. (2010). k-Wave: MATLAB toolbox for the simulation and reconstruction of photoacoustic wave fields. Journal of biomedical optics, 15(2), 021314.

Treeby, B. E., Jaros, J., Rohrbach, D., & Cox, B. T. (2014, September). Modelling elastic wave propagation using the k-wave matlab toolbox. In 2014 IEEE international ultrasonics symposium (pp. 146-149). IEEE.

V. Volpert and S. Petrovskii, "Reaction–diffusion waves in biology," Physics of life reviews, vol. 6, no. 4, pp. 267-310, 2009.

Ventura, D. (2008). Manifold Learning Examples–PCA, LLE and ISOMAP. Department of Computer Science, Brigham Young University, Provo, UT, USA.

von Mises, R. (1981). Uber die" Ganzzahligkeit" der Atomgewicht und verwandte Fragen. Physikal. Z., 19, 490-500.

von Mises, R., “Mathematical Theory of Probability and Statistics”, New York: Academic Press, 1964.

W. S. Noble, "What is a support vector machine?" Nature biotechnology, vol. 24, no. 12, pp. 1565-1567, 2006.

Wang W, Liao H, Huang Y (2007) Rock fracture tracing based on image processing and SVM. In: Third international conference on natural computation, ICNC, pp 632–635.

Wang, Y., Arns, C. H., Rahman, S. S., & Arns, J. Y. (2018). Porous structure reconstruction using convolutional neural networks. Mathematical geosciences, 50(7), 781-799.

Wang, X. X., Cao, W. Q., Cao, M. S., & Yuan, J. (2020). Assembling nano–microarchitecture for electromagnetic absorbers and smart devices. Advanced materials, 32(36), 2002112.

Wang, Y., Oyen, D., Guo, W. G., Mehta, A., Scott, C. B., Panda, N., ... & Yue, X. (2021). StressNet-Deep learning to predict stress with fracture propagation in brittle materials. npj Materials Degradation, 5(1), 1-10.

Wong, R. H. C., Chau, K. T., Tang, C. A., & Lin, P. (2001). Analysis of crack coalescence in rock-like materials containing three flaws—part I: experimental approach. International Journal of Rock Mechanics and Mining Sciences, 38(7), 909-924.

Wong, K. W., Fung, C. C., Ong, Y. S., & Gedeon, T. D. (2005, November). Reservoir characterization using support vector machines. In International Conference on Computational Intelligence for Modelling, Control and Automation and International Conference on Intelligent

Agents, Web Technologies and Internet Commerce (CIMCA-IAWTIC'06) (Vol. 2, pp. 354-359). IEEE.

Wong, R. H., & Chau, K. T. (1998). Crack coalescence in a rock-like material containing two cracks. International Journal of Rock Mechanics and Mining Sciences, 35(2), 147-164.

Wu, S. C., Xiao, T. Q., & Withers, P. J. (2017). The imaging of failure in structural materials by synchrotron radiation X-ray microtomography. Engineering Fracture Mechanics, 182, 127-156.

Wu, B., & Huang, W. (2020). Uniaxial Compression Mechanical Properties of Rock Samples in Soft and Hard Composite Strata. Advances in Materials Science and Engineering, 2020.

Xiong, W., Ji, X., Ma, Y., Wang, Y., AlBinHassan, N. M., Ali, M. N., & Luo, Y. (2018). Seismic fault detection with convolutional neural network. Geophysics, 83(5), O97-O103.

Xu, S., Ross, C., Raebel, M. A., Shetterly, S., Blanchette, C., & Smith, D. (2010). Use of stabilized inverse propensity scores as weights to directly estimate relative risk and its confidence intervals. Value in Health, 13(2), 273-277.

Xue, L., Liu, Y., Xiong, Y., Liu, Y., Cui, X., & Lei, G. (2021). A data-driven shale gas production forecasting method based on the multi-objective random forest regression. Journal of Petroleum Science and Engineering, 196, 107801.

Y. Lin and Y. Jeon, "Random forests and adaptive nearest neighbors (Technical Report No. 1055)," University of Wisconsin, 2002.

Zahedi, P., Parvandeh, S., Asgharpour, A., McLaury, B. S., Shirazi, S. A., & McKinney, B. A. (2018). Random forest regression prediction of solid particle Erosion in elbows. Powder Technology, 338, 983-992.

Zazoun, R. S. (2013). Fracture density estimation from core and conventional well logs data using artificial neural networks: The Cambro-Ordovician reservoir of Mesdar oil field, Algeria. Journal of African Earth Sciences, 83, 55-73.

Zhao, Y., & Liu, Q. (2023). Causal ML: Python package for causal inference machine learning. SoftwareX, 21, 101294.

Zhong, R., Johnson Jr, R., & Chen, Z. (2020). Generating pseudo density log from drilling and logging-while-drilling data using extreme gradient boosting (XGBoost). International Journal of Coal Geology, 220, 103416.

Zhou, J., Li, E., Wang, M., Chen, X., Shi, X., & Jiang, L. (2019). Feasibility of stochastic gradient boosting approach for evaluating seismic liquefaction potential based on SPT and CPT case histories. Journal of Performance of Constructed Facilities, 33(3), 04019024.

APPENDIX A

FEATURE SET BASED ON STATISTICAL PARAMETERIZATIONS

1) Mean: the average pressure of points in waveform.
2) Median: the median pressure of points in waveform.
3) Variance: measures variability from the average or mean.
4) Standard deviation: measures the dispersion of dataset relative to its mean, the square root of variance.
5) Skewness: calculate with the adjusted Fisher-Pearson standardized moment coefficient G1.
6) Kurtosis: calculated with the adjusted Fisher-Pearson standardized moment coefficient G2.
7) Energy: absolute energy of the time series which is the sum over the squared values.
8) Maximum amplitude index of the signal: index of signal maximum point.
9) Minimum amplitude index of the signal: index of signal minimum point.
10) 10th Percentiles: measures to indicate the value below 10 percentage of observations in a group of observations fall.
11) 90th Percentiles: measures to indicate the value below 90 percentage of observations in a group of observations fall.
12) Zero crossing: number of crossings of x on zero.
13) Number of peaks: number of peaks of at least support n in the time series x.
14) Longest period above mean: returns the length of the longest consecutive subsequence in x that is bigger than the mean of x.
15) Variance coefficient: returns the variation coefficient (standard error / mean, give relative value of variation around mean) of x.
16) Sum Value: the sum value over the time series values.
17) Autocorrelation: the autocorrelation of the specified lag.
18) Mean value of second derivation: returns the mean value of a central approximation of the second derivative.
19) Positive turning: number of positive turning points of the signal.
20) Negative turning: number of negative turning points of the signal.

APPENDIX B

AVERAGE CAUSAL EFFECTS FROM BINARY TREATMENT

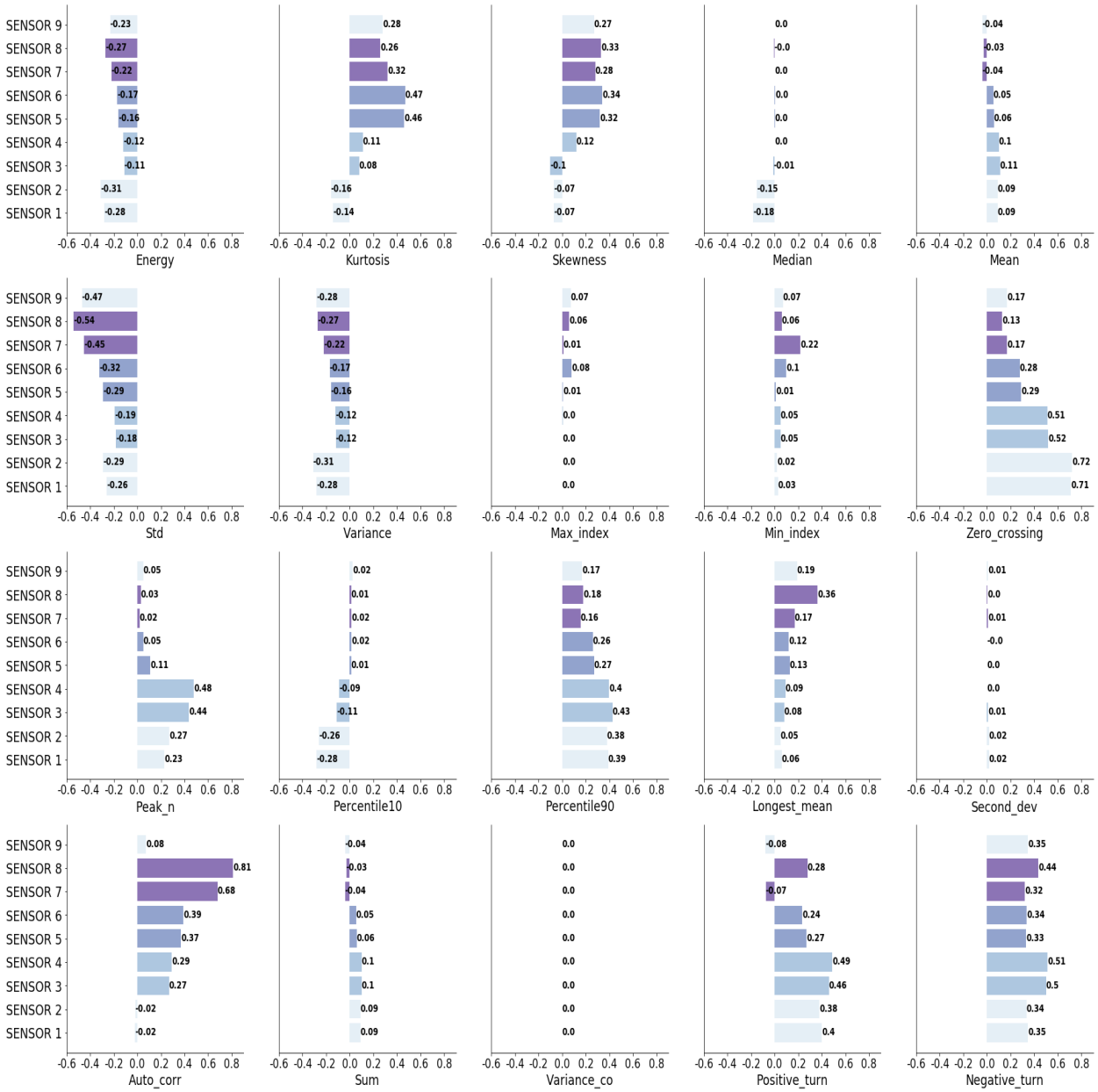

Figure B-1. Detail ATE bar plot for 20 statistical features compute from 9 elastic waves captured by different sensors around material.

APPENDIX C

AVERAGE CAUSAL EFFECTS FROM CONTINUOUS TREATMENT

Band 1:

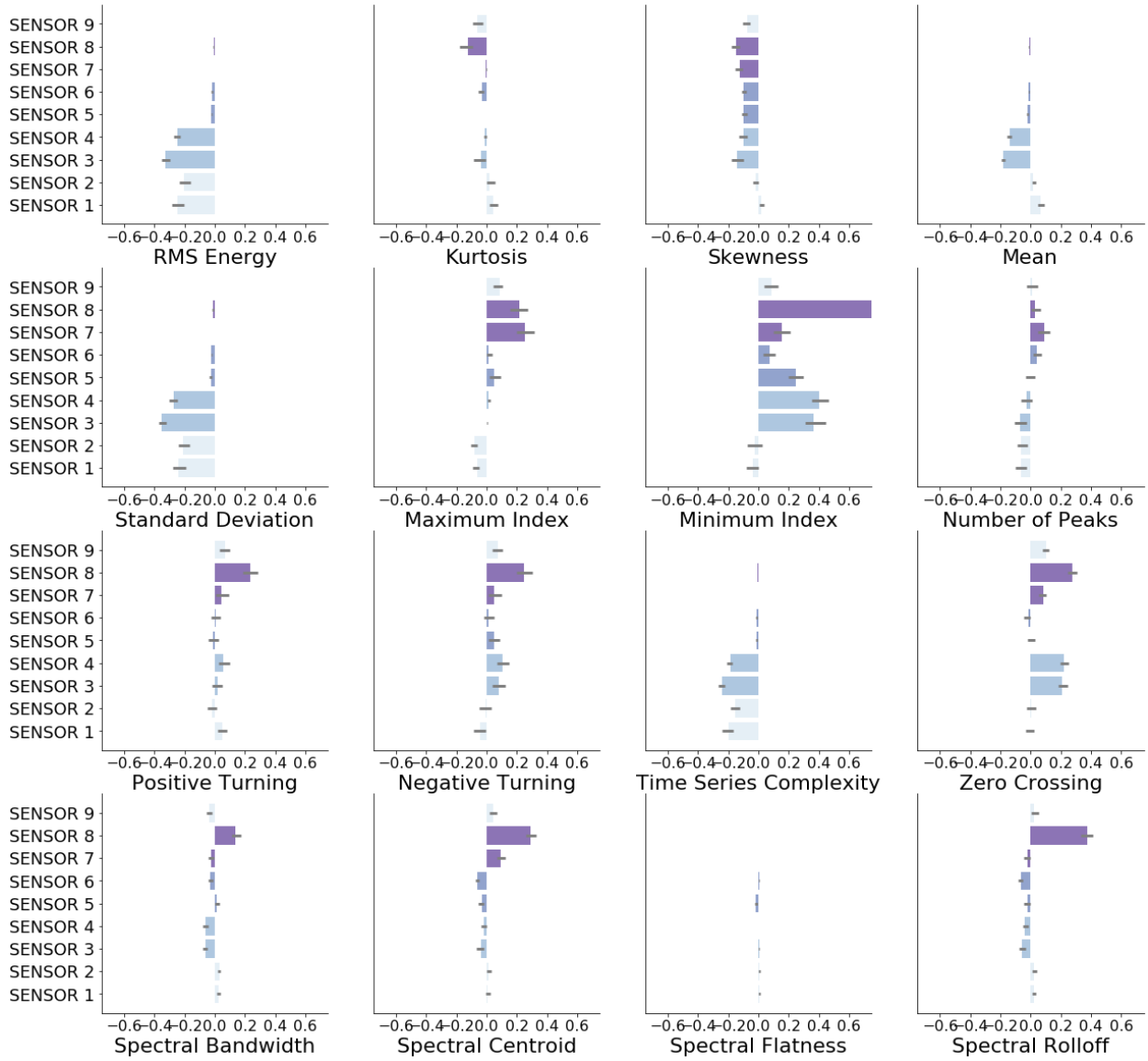

Figure C-1. Band 1 ATE bar plot for the 16 statistical-parameterization based features computed from the 9 waveforms captured by 9 sensors placed around the surface of the material. All zeros mean that no causal relationship was found between the feature and the target and the feature failed the refutation test. A positive ATE means the crack propagation has a positive impact on the feature. The gray line around our estimate is 95% confidence interval calculated from bootstrap method with 100 simulations.

Band 2:

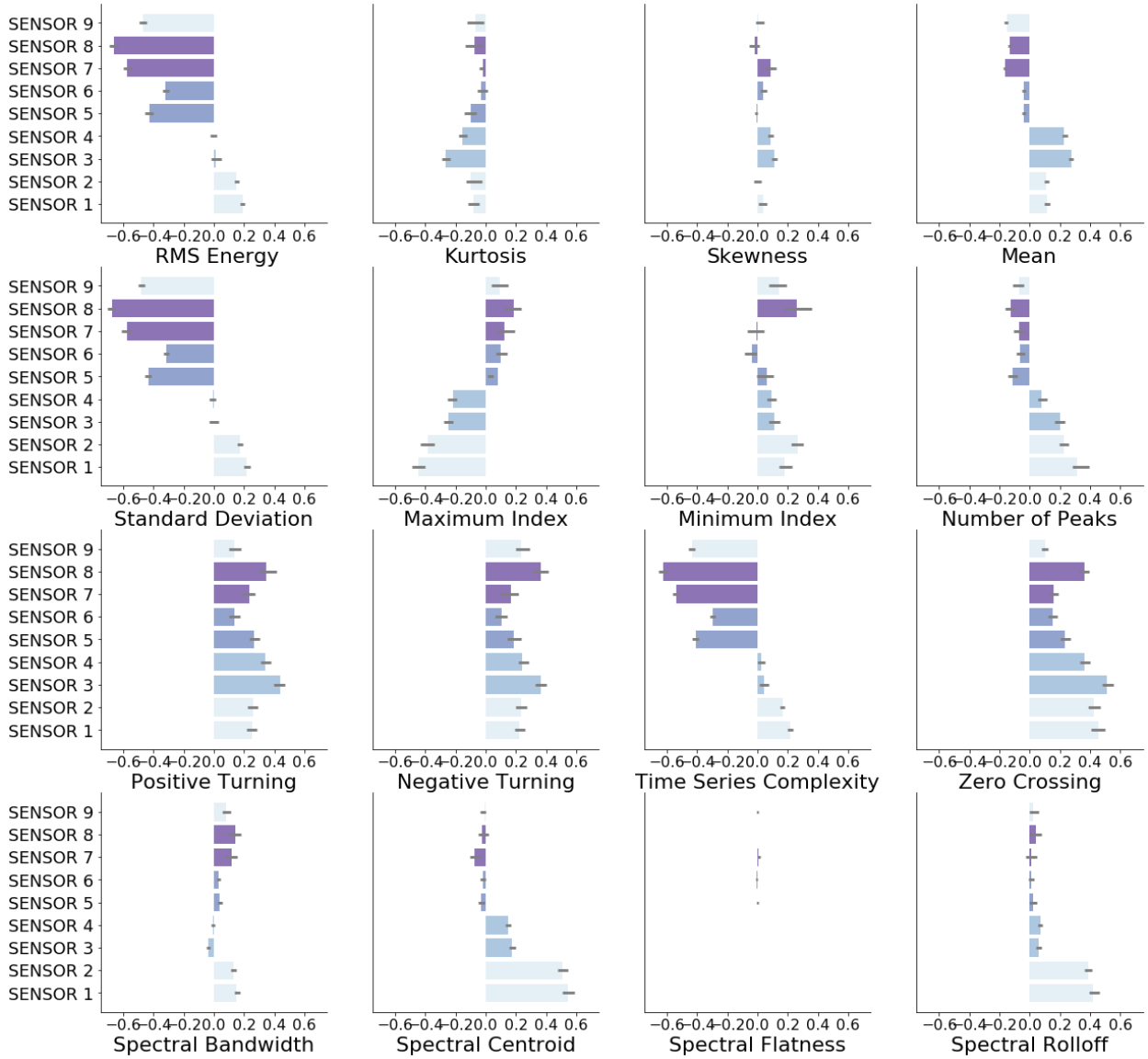

Figure C-2. Band 2 ATE bar plot for the 16 statistical-parameterization based features computed from the 9 waveforms captured by 9 sensors placed around the surface of the material. All zeros mean that no causal relationship was found between the feature and the target and the feature failed the refutation test. A positive ATE means the crack propagation has a positive impact on the feature. The gray line around our estimate is 95% confidence interval calculated from bootstrap method with 100 simulations.

Band 3:

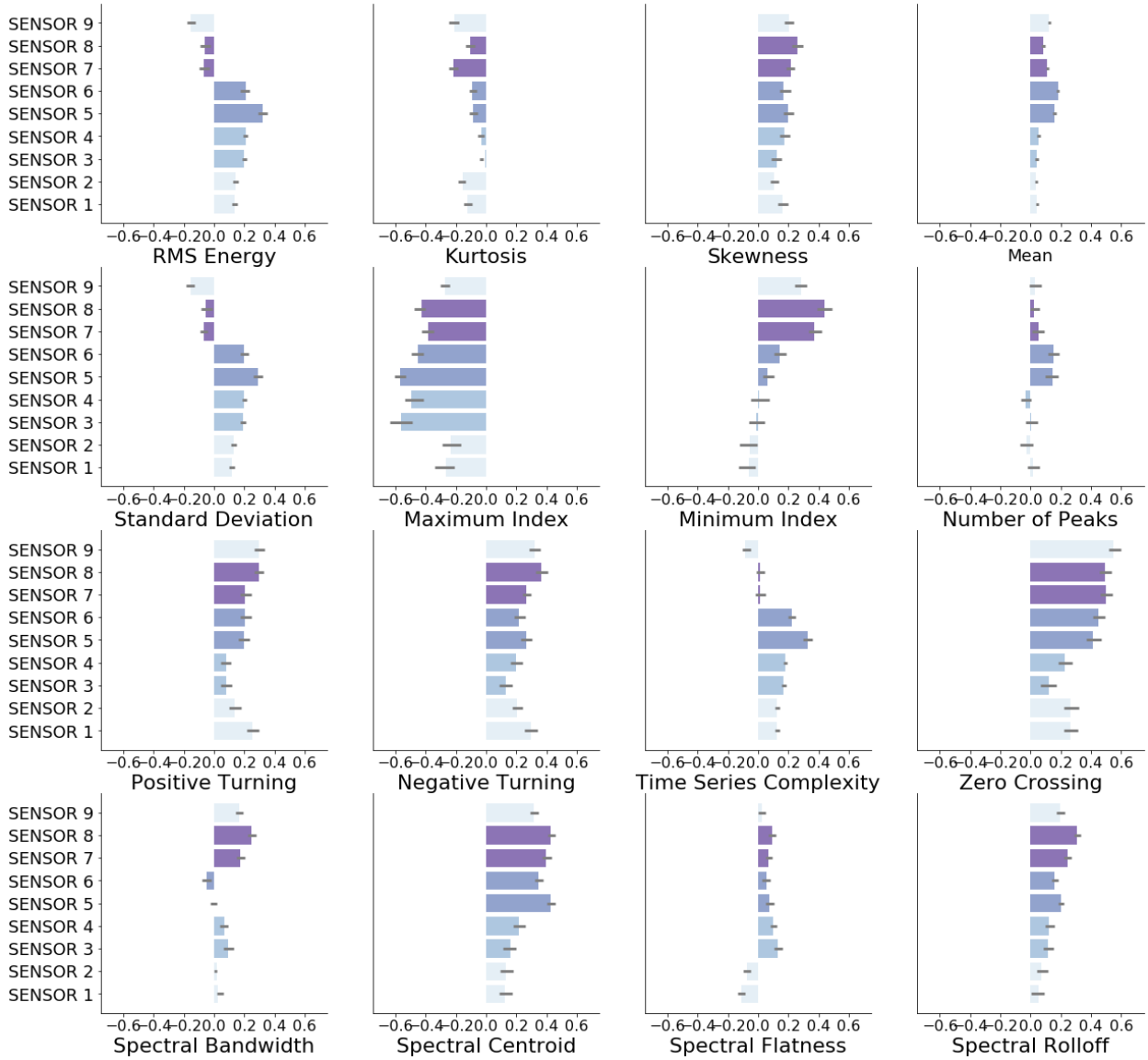

Figure C-3. Band 3 ATE bar plot for the 16 statistical-parameterization based features computed from the 9 waveforms captured by 9 sensors placed around the surface of the material. All zeros mean that no causal relationship was found between the feature and the target and the feature failed the refutation test. A positive ATE means the crack propagation has a positive impact on the feature. The gray line around our estimate is 95% confidence interval calculated from bootstrap method with 100 simulations.

APPENDIX D

HOSS SIMULATION SAMPLES

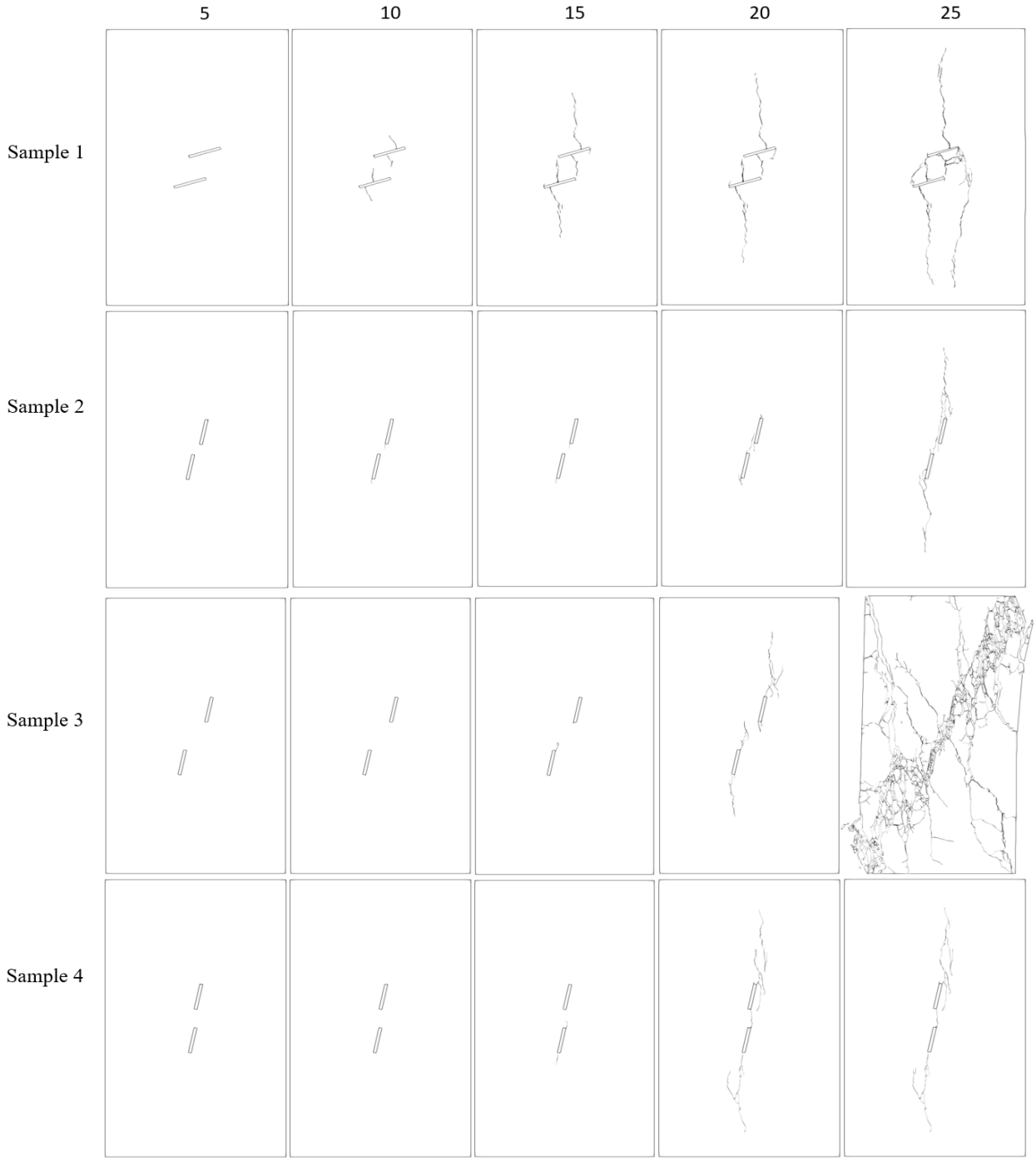

Figure D-1. HOSS simulation samples of fracture coalescence and propagation with five time steps.

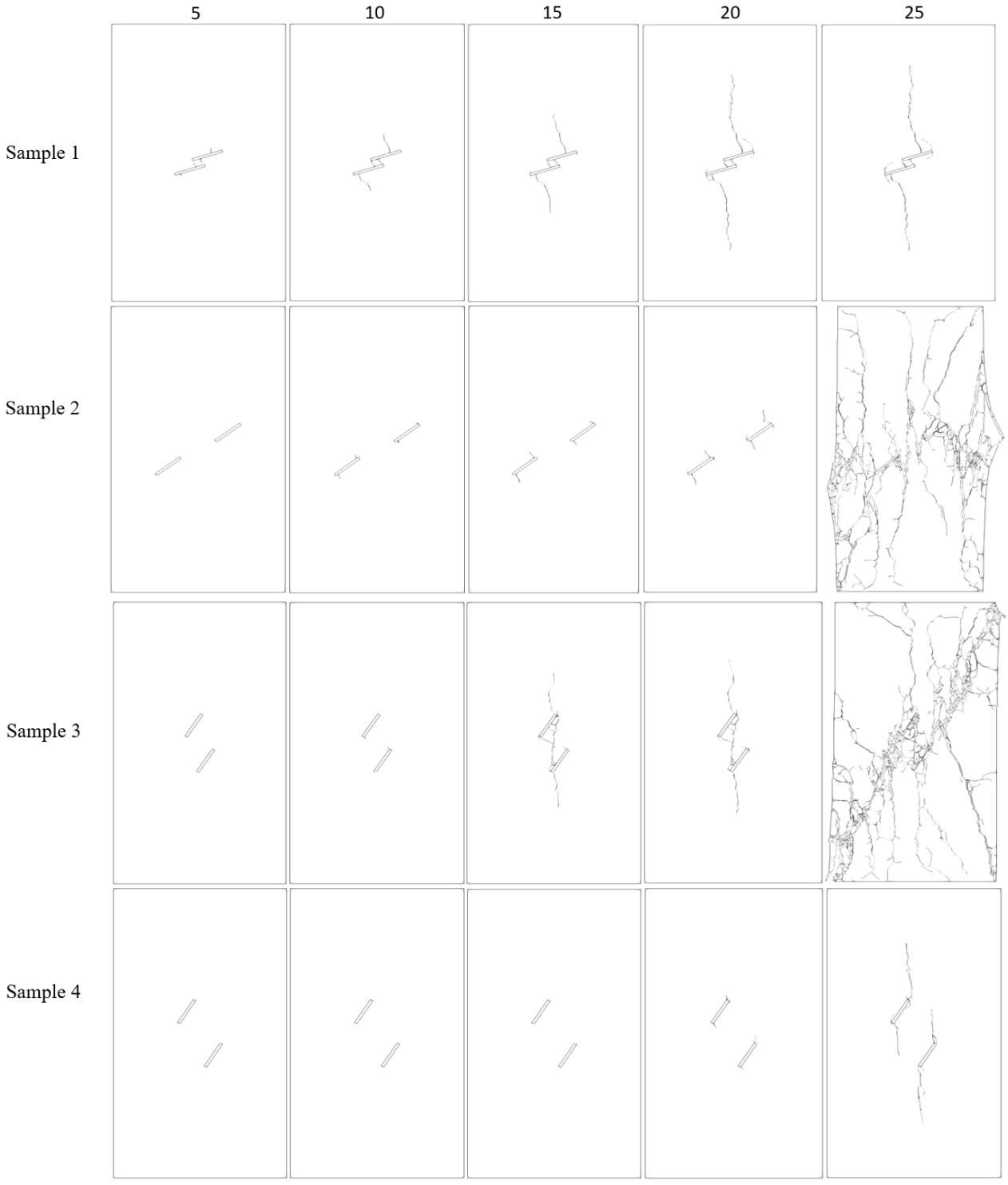

Figure D-2. HOSS simulation samples of fracture coalescence and propagation with five different time steps.

APPENDIX E

FEATURE SPACE FOR CAUSAL DISCOVERY

1) Mean: the average pressure of points in time series x.
2) Skewness: calculate with the adjusted Fisher-Pearson standardized moment coefficient G1.
3) Kurtosis: calculated with the adjusted Fisher-Pearson standardized moment coefficient G2.
4) Standard deviation: measures the dispersion of dataset relative to its mean, the square root of variance.
5) Number of peaks: number of peaks of at least support n in the time series x.
6) Maximum amplitude index of the signal: index of signal maximum point.
7) Minimum amplitude index of the signal: index of signal minimum point.
8) Zero crossing: number of crossings of x on zero.
9) Positive turning: number of positive turning points of the signal.
10) Negative turning: number of negative turning points of the signal.
11) Longest period above mean: returns the length of the longest consecutive subsequence in x that is bigger than the mean of x.
12) Longest period below mean: returns the length of the longest consecutive subsequence in x that is smaller than the mean of x.
13) Entropy: calculate and return Shannon sample entropy of time series x.
14) Autocorrelation: the autocorrelation of the specified lag.
15) Nonlinearity: computed nonlinearity coefficient using a modification of the statistic with Teräsvirta's nonlinearity test.
16) Flat spots: computed by dividing the sample space of a time series into ten equal-sized intervals, and computing the maximum run length within any single interval.
17) Peak to peak distance: computes the peak to peak distance.
18) Median crossing: number of crossings of x on median value.
19) Variation coefficient: returns the variation coefficient (standard error / mean, give relative value of variation around mean) of time series x.
20) Sum of reoccurring points: returns the sum of all points that are present in the signal more than once.
21) Sum of reoccurring values: returns the sum of all values that are present in the signal more than once.
22) Mean changes: returns the meaning over the differences between subsequent time series x.
23) Count above mean: Returns the percentage of values in x that are higher than mean.
24) Count below mean: Returns the percentage of values in x that are smaller than mean.
25) Spectral centroid: measures the center of mass of the spectrum.

26) Maximum Frequency: computes maximum frequency of the signal.
27) Spectral kurtosis: measures the flatness of a distribution around mean value.
28) Spectral skewness: measures the asymmetry of a distribution around its mean value.
29) Spectral positive turning: computes number of positive turning points of the FFT magnitude signal.
30) Spectral spread: measures the spread of the spectrum around its mean value.